REPUBLIQUE DU CAMEROUN
Paix – Travail – Patrie
****
UNIVERSITE DE YAOUNDE I
FACULTE DES SCIENCES
DEPARTEMENT DE PHYSIQUES
****
CENTRE DE RECHERCHE ET DE FORMATION DOCTORALE EN SCIENCES, TECHNOLOGIES ET GEOSCIENCES

REPUBLIC OF CAMEROUN
Peace – Work – Fatherland
****
UNIVERSITY OF YAOUNDE I
FACULTY OF SCIENCE
DEPARTMENT OF PHYSICS
****
POSTGRADUATE SCHOOL OF SCIENCES, TECHNOLOGY AND GEOSCIENCES
Laboratory of Nuclear, Atomic, Molecular and Biological Physics

EFFECT OF ELECTROMAGNETIC INDUCTION AND RADIATION ON THE ELECTRICAL ACTIVITY OF BIOLOGICAL EXCITABLE CELLS

Thesis submitted and defended in partial fulfillment of the requirements for the award of the degree of Doctor of Philosophy (PhD) in Physics

Par : **TAKEMBO NTAHKIE Clovis**
Master of Science in Physics

Sous la direction de
EKOBENA FOUDA Henri Paul
Professor

Année Académique : 2020

UNIVERSITE DE YAOUNDE I
UNIVERSITY OF YAOUNDE I

FACULTE DES SCIENCES
FACULTY OF SCIENCE

DEPARTEMENT DE PHYSIQUE
DEPARTMENT OF PHYSICS

ATTESTATION DE CORRECTION DE LA THESE DE DOCTORAT/Ph.D

Nous, Professeur **NDJAKA Jean-Marie Bienvenu**, Examinateur, et Professeur **BEN-BOLIE Germain Hubert**, Président du jury de la Thèse de Doctorat/Ph.D de Monsieur **TAKEMBO NTAHKIE Clovis**, Matricule **12W1879**, préparée sous la direction du Professeur **EKOBENA FOUDA Henri Paul** intitulée : « **Effect of electromagnetic induction and radiation on the electrical activity of biological excitable cells** », soutenue le **Vendredi, 17 juillet 2020**, en vue de l'obtention du grade de Docteur/Ph.D en Physique, Spécialité **Physique Atomique, Moléculaire et Biophysique**, option **Biophysique** attestons que toutes les corrections demandées par le jury de soutenance ont été effectuées.

En foi de quoi, la présente attestation lui est délivrée pour servir et valoir ce que de droit.

Fait à Yaoundé le 13 JUIL 2020

L'Examinateur

Pr. NDJAKA Jean-Marie Bienvenu

Le Président du jury

Pr. BEN-BOLIE Germain Hubert

Le Chef de Département de Physique

UNIVERSITE DE YAOUNDE I * FACULTE DES SCIENCES * Le Chef de Département * DEPARTEMENT DE PHYSIQUE

Pr. NDJAKA Jean-Marie Bienvenu

EFFECT OF ELECTROMAGNETIC INDUCTION AND RADIATION ON THE ELECTRICAL ACTIVITY OF BIOLOGICAL EXCITABLE CELLS

Submitted in Partial Fulfillment of the Requirements

for the Degree of Doctorate/PhD in Physics

Option: **Atomic, Molecular and Biological Physics**

by

TAKEMBO NTAHKIE Clovis

BSc, MSc in Physics

Registration Number: **12W1879**

Under the supervision of

EKOBENA FOUDA Henri Paul

Professor, UYI

July 14, 2020

Dedication

To my Saviour, Lord Jesus Christ.

Acknowledgments

Recognizing that no human endeavor and effort can be achieved without the blessing and grace of the Almighty God, I thank him for allowing me to begin and complete this Thesis. Throughout the process, his grace in my life has inspired new ideas that have given me the desire and motivation to carry-out the research. I give God all the glory, honor and adoration.

I would like to express my deep gratitude to all the people who contributed, in whatever manner, to the success of this work. Firstly, I thank my supervisor, **Prof. EKOBENA FOUDA Henri Paul** for devoting his valuable time and resources for the realization of this thesis. I express my deepest thanks to **Dr Mvogo Alain** who allowed me to integrate the rich and fascinating domain of neuroscience and cardiology on which this thesis is based. These domains of modern science has enable me to better discern the mechanisms of electrical impulse transmission by neurons and myocardial cells in a well organized network. Using these networks, it has also been possible the discern the role of external electromagnetic radiation on neural and cardiac systems. Thanks to the ingenuity of this "Master" of nonlinear Physics, I quickly integrated a novel research world where a few years earlier I would not have risked it. His passion for research, his love for a job well done, his diligence in the finalization of a project, his perseverance in the search for original results, his particular interest in the transfer of skills and autonomy, here are so many other virtues that I have received from this great hero of Biophysics, **Prof. KOFANE Timoléon Crépin**. Excellently, **Prof. KOFANE** and **Dr Mvogo Alain** coordinated the follow-up of all the results presented in this Thesis via relevant orientations and appreciations. Thanks to them, we understood and interpreted the complex wave phenomena of Modulationnal Instability, through the theory of soliton in the transfer of information and excitation of the nervous and cardiac systems.

I am also grateful to **Prof. BEN-BOLIE Germain Hubert** , **Prof. TABI Conrad Bertrand** and **Prof. MOHAMADOU ALIDOU** who largely contributed to the

motivation and the realization of this scientific work. I would like to express my deep gratitude to them who have also welcomed and trained many students, as well as enhanced the image of our institution through remarkable scientific contributions.

Furthermore, I would like to thank my teachers who taught me the fundamentals of sciences. They are: **Prof. NDJAKA Jean-Marie**, **Prof. WOAFO Paul**, **Prof. OWONO OWONO Luc Calvin**, **Prof. PEMHA Elkana**, **Prof. TCHAWOUA Clément**, **Prof. ZEKENG Serge**, **Prof. NDJOMO Donatien**, **Prof. MANGUELE Dikoum Eléazar**, **Prof. OWONO ATEBA**, **Prof. NANA NBENJO**, **Prof. ESSIMBI ZOBO**, **Prof. EYEBE FOUDA Armand**, **Prof. HONA Jacques**, **Prof. MBANE BIOULE**, **Prof. SIEWE SIEWE Martin**, **Prof. FEWO Serges Ibraid**, **Prof. DJUIDJE KENMOE Germaine**, **Dr WOULACHE Rosalie Laure**, **Dr BEYALA ATEBA Jean Félix**, Dr **ENYEGUE Francoise**.

I also take this opportunity to thank all my academic elders who shared with me their experience on calculation methods, the use of software essential for the research and interpretation of some complex phenomena. They are: **Dr MAÏNA Ibrahim**, **Dr ADAMOU DANG Koko** and **Dr ETEME Alain Sylvain**.

Additionally, I would like to thank my classmates who supported me with various actions throughout my academic career. I am thinking mainly of: **Mr NGUIMFACK Boris**, **Mr KUIPOU William**, **Mr ALOA Claude**.

Furthermore, I wish to express my heartfelt thanks to the parents, brothers, sisters and friends who have distinguished themselves by their immeasurable commitments throughout my academic training. First of all, my late father, **TAKEMBO ADAMU**, who did everything and gave everything before the world separated us. Then my mother **Regina NCHONGWA**, my brothers, **MUNGWA**; **Rogers, David, Martin, Joseph, Denis, Augustine, Edwin, Rapheal, Bertrand** and my sisters **Mrs MBAH Ernestine**, **MUNGWA Sophina**, **MUNGWA Gladys**. I greatly thank the family of **Mr TAMBOUH Oscar** and **Mr MUCHIA Elvis** for their psychological and material supports which have largely contributed to the success of this Thesis. Special thanks to **Prof. GOGHOMU Paul MINGO**, presently the Minister in charge of special duty at the presidency of the Republic of Cameroon for his motivation and material supports.

Contents

Dedication i

Acknowledgments ii

Contents iv

List of Figures viii

List of Abbreviations xiv

Résumé xv

Abstract xvi

General Introduction 1

0.1 Context of the thesis 2

0.2 Problematic and objectives of the thesis 4

0.3 Organization of the Thesis 5

Chapter 1 Literature review: The Biology of Cardiac Tissue and Neuronal Networks 6

Introduction 6

1.1 Cardiac Muscle and Electrical Activity 8

1.1.1 Structure of Cardiac muscle 8

1.1.2 Conduction System of the Heart 10

1.1.3 Membrane Potentials and Ion Movement in Cardiac Conductive Cells 13

1.1.4 Comparative Rates of Conduction System Firing 14

1.2 Neurons 15

1.2.1 Structure and Functions 15

1.2.2 Classification of neurons 17

1.2.3 Electrical Activity of Neurons 18
1.2.3.1 The cell membrane 19
1.2.3.2 The resting Potential 19
1.2.3.3 The action Potential 20
1.2.3.4 The Nerve Impulse 24
1.3 The Neural Networks 25
1.3.1 The Synapses 25
1.3.1.1 Chemical Synapses 26
1.3.1.2 Electrical Synapses 27
1.3.1.3 Excitatory Synapses 28
1.3.1.4 Inhibitory Synapses 29
1.3.1.5 Modulatory synapses 29
1.3.2 Functional and behavioral properties of neural networks 29
1.4 Mathematical Neuron Models 30
1.4.1 Hodgkin-Huxley Model 31
1.4.2 Integrate and Fire Model 33
1.4.3 FitzHugh-Nagumo Model 34
1.4.4 Hindmarsh-Rose Model 35
1.4.5 Izhikevich Model 35
1.4.6 Morris-Lecar Model 36
1.4.7 Comments on the various Models 36
Conclusion 37

Chapter 2 Improved models of FitzHugh-Nagumo and methodologies 39
Introduction 39
2.1 Improved FHN models 41
2.1.1 The discrete FHN neural model under magnetic flow 41
2.1.2 The discrete FHN myocardial model under magnetic flow 42
2.1.3 The FHN neuronal network with memristive electromagnetic induction coupling 43
2.1.4 The one dimensional diffusive FHN myocardial network under electromagnetic induction 45
2.2 Analytical and Numerical methods 48
2.2.1 The multiple scale expansion in the discrete approximation 48

2.2.1.1 Derivation of DNLS equation with coefficients depending on MF parameter 50
2.2.1.2 Derivation of a DNLS equation with coefficients depending on the EMI gain 52
2.2.1.3 Derivation of a DNLS equation with coefficients depending on the MSC parameter 54
2.2.2 The semi-discrete approximation 55
2.2.2.1 Derivation of damped CGL equations for myocardial cell WP. 57
2.2.2.2 Exact solutions of the modified CGLE 65
2.2.2.3 Linear stability analysis on a discrete NLS equation 67
2.2.3 The RK4 numerical integration method 68
Conclusion 69

Chapter 3 Results and Discussion: Linear Stability Analysis and Spatiotemporal Patterns under Magnetic Flow 71

Introduction 71
3.1 MF patterns in FHN neural networks 72
3.1.1 Analytical analysis of MI 72
3.1.2 Numerical analysis of MI 73
3.2 MF patterns in FHN cardiac tissue under electromagnetic radiation 84
3.2.1 Analytical analysis of MI 84
3.2.2 Spatiotemporal patterns and biological implications 87
3.3 Effect of EMR on the dynamics of spatiotemporal patterns in memristor-based neuronal network 92
3.3.1 Analytical features of MI 93
3.3.2 Numerical analysis of MI 93
3.4 Modulated wave solution of diffusive myocardial network under magnetic flow effects 98
3.4.1 Numerical experiments 100
Conclusion 102

General Conclusion 114

Bibliography **117**

List of publications **124**

List of Figures

Figure 1.1 (a) Cardiac muscle cells with myofibrils composed of myofilaments arranged in sarcomeres, T tubules to transmit the impulse from the sarcolemma to the interior of the cell, numerous mitochondria for energy, and intercalated discs that are found at the junction of different cardiac muscle cells. (b) A photomicrograph of cardiac muscle cells shows the nuclei and intercalated discs. (c) An intercalated disc connects cardiac muscle cells and consists of desmosomes and gap junctions. $LM1600$. (Micrograph provided by the Regents of the University of Michigan Medical School ľ 2012) [46]. 9

Figure 1.2 Specialized conducting components of the heart; the sinoatrial node, the internodal pathways, the atrioventricular node, the atrioventricular bundle, the right and left bundle branches, and the Purkinje fibers [46]. 10

Figure 1.3 (1) The sinoatrial (SA) node and the remainder of the conduction system are at rest. (2) The SA node initiates the action potential, which sweeps across the atria. (3) After reaching the atrioventricular node, there is a delay of approximately 100 ms that allows the atria to complete pumping blood before the impulse is transmitted to the atrioventricular bundle. (4) Following the delay, the impulse travels through the atrioventricular bundle and bundle branches to the Purkinje fibers, and also reaches the right papillary muscle via the moderator band. (5) The impulse spreads to the contractile fibers of the ventricle. (6) Ventricular contraction begins. [46]. . . . 12

Figure 1.4 The prepotential is due to a slow influx of sodium ions until the threshold is reached followed by a rapid depolarization and repolarization. The prepotential accounts for the membrane reaching threshold and initiates the spontaneous depolarization and contraction of the cell. We note the lack of a resting potential [46]. 14
Figure 1.5 Annotated diagram of a neuron [47]. 16
Figure 1.6 Structural categories of neurons [48]. 18
Figure 1.7 Cell membrane flow diagram [49]. 20
Figure 1.8 Measuring charge across a Membrane with a voltmeter. A recording electrode is inserted into the cell and a reference electrode is outside the cell. By comparing the charge measured by these two electrodes, the transmembrane voltage is determined. It is conventional to express that value for the cytosol relative to the outside [49]. 21
Figure 1.9 Action potential graph [50]. 23
Figure 1.10 A neural network with three neurons [57] 25
Figure 1.11 Chemical synapse diagram [61]. 26
Figure 1.12 Electrical synapse flow diagram [62]. 27
Figure 1.13 Electrical equivalent circuit for a short segment of squid giant axon according to [7]. The capacitor represents the capacitance of the cell membrane; the two variable resistors represent voltage-dependent Na^+ and K^+ conductances, the fixed resistor represents a voltage-independent leakage conductance and the three batteries represent reversal potentials for the corresponding conductances. 32

Figure 2.1 Panel displays the plot of angular frequency (ω), vs. the wave number (q), as given by the dispersion relation in Eq. (2.56), for $D_0 = 0.05$ and $k_0 = 1.2$ 57
Figure 2.2 Panel shows how ω is a decreasing function of the memristor coupling parameter k_0. The lower and upper cut off frequencies are lowered as the effect of electromagnetic induction is increased thus more cells could be recruited into conduction process. The parameter values are the same as in Fig. (2.1) 58
Figure 2.3 Panel displays the plot of group velocity (V_g) vs. the wave number (q), as given by the dispersion relation in Eq. (2.59), for $k_0 = 1.0$. 59

Figure 2.4 Group velocity is an increasing function of the memristor coupling. 59
Figure 2.5 A plot of the dispersion coefficient vs. wave number in panel (a) and the influence of memristor coupling depicted in panel (b). . . . 62
Figure 2.6 A plot of the dissipation coefficient vs. wave number in panel (a) and the influence of memristor coupling depicted in panel (b). . . . 63
Figure 2.7 A plot of the real part of nonlinearity coefficient vs. wave number in panel (a) and the influence of memristor coupling depicted in panel (b). 63
Figure 2.8 A plot of the imaginary part of nonlinearity coefficient vs. wave number in panel (a) and the influence of memristor coupling depicted in panel (b). 64
Figure 2.9 A plot of the instability criteria coefficient vs. wave number in panel (a) and the influence of memristor coupling depicted in panel (b). . 65

Figure 3.1 Panels display the critical amplitude $\eta_{0,cr}$, vs. the wave number q, as given by the instability criterion (20). Panel (a) displays the critical amplitude for $k_1 = 0.1$ and $K = 0.05$, while panel (b) shows how $\eta_{0,cr}$ is an increasing function of the MC parameter for $K = 0.5$ 73
Figure 3.2 Panels show the spatiotemporal features of patterns at fixed parameters k_1=1.5, $K = 0.05$ and $I_{ext} = 0.05$, (a) 3D feature, (b) X, Z plane and (c) X, Y plane 75
Figure 3.3 Panels show the spatiotemporal features of patterns at fixed parameters k_1=2.5, $K = 0.05$ and $I_{ext} = 0.05$, (a) 3D feature, (b) X, Z plane and (c) X, Y plane 76
Figure 3.4 Panels depict the (X,Z) and (X,Y) planes of spatiotemporal features of patterns for K=0.5 at fixed parameters k_1=2.5 and $I_{ext} = 0.05$. 78
Figure 3.5 Panels show the spatial features of patterns at fixed parameters $k_1 = 2.5$, K=0.5 and $I_{ext} = 0.5$ at: (a) t=1500 and (b) t=2500 . . . 79
Figure 3.6 Panels show the features of patterns by setting different transmembrane currents at fixed parameters K=0.5, ω=0.05, $k_1 = 1.5$ for (a) I_0=0.01, (b) I_0=1.00 and (c) I_0=2.50 80
Figure 3.7 Panels show the features of patterns by setting different values of angular frequency of transmembrane currents at fixed parameters $K = 0.5, k_1 = 2.5, I_0 = 1$ for (a) $\omega = 0.1$, (b) $\omega = 0.5$ and (c) $\omega = 1.5$ 82

Figure 3.8 Panels show the features of patterns when induction current $k_1\rho(\phi_n)v_n$ is generated with different intensities. The parameters are selected by $K = 0.5, \omega = 0.5, I_0 = 1.0$ for (a) $k_1 = 0.1$, (b) $k_1 = 0.5$ and (c) $k_1 = 2.5$ 83

Figure 3.9 Figure displays the plot of critical amplitude $\chi_{0,cr}$, vs. the wave number q, as given by the instability criterion (3.5), with $k_0 = 1.6$ and $K = 0.01$ 85

Figure 3.10 Figure displays the plot of critical amplitude $\chi_{0,cr}$, vs. the wave number q, as given by the instability criterion (3.5) for different values of memristor coupling k_0, with $K = 0.02$. We observe; $\eta_{0,cr}$ is an increasing function of memristor coupling k_0 86

Figure 3.11 Figure shows the spatiotemporal features (the 3D feature) of patterns for the magnetic flux gain $k_0 = 2.51, t = 200$. Other parameter values used are; $K = 0.5, I_0 = 0.035$ and $\omega = 0.8$ 87

Figure 3.12 Panels show the spatial features of patterns for different magnetic flux gain k_0; (a) 2.51, (b) 2.53 and (c) 2.58 88

Figure 3.13 Panels show the spatial features of patterns for the electromagnetic intensity (a) H_0=2.50, (b) H_0=2.54 and (c) H_0=2.65, with $k_0 = 1.50$ 89

Figure 3.14 Panels show the spatiotemporal features of patterns for the memristor coupling parameter (a) k_0=0.50, (b) k_0=1.50 and (c) k_0=2.04, with H_0=1.3 90

Figure 3.15 Panels show the spatiotemporal features of patterns for the stimulation current(a) I_0=0.09, (b) I_0=0.19, and (c) I_0=0.29. Other parameters were set at K_0=1.80, ω=0.8 and Ω=0.05 103

Figure 3.16 Plot of critical amplitude, vs. the wave number for different values of memristive synaptic coupling (K). The growth rate of modulational instability is an increasing function of the memristive synaptic gain(K). 104

Figure 3.17 Panel presents spatially homogeneous patterns, with temporal periodic-like structures calculated for the memristive synaptic gain $K = 0.05$, with $I_{ext} = 0.6$ 104

Figure 3.18 Panels show the spatiotemporal features for different values of the memristive synaptic gain; (a) K=1.0, (b) K=5.0, and K= 10.0, with $I_{ext} = 0.6$ 105

Figure 3.19 Time series for membrane potential at the nodes 10, 200, and 500 with K=0.05 and $I_{ext} = 0.6$ 105

Figure 3.20 Time series of the node 300 for different external stimuli; (a) $I_{ext} = 1.300$ (b) $I_{ext} = 1.410$ (c) $I_{ext} = 1.418$ and (d) $I_{ext} = 1.421$ 106

Figure 3.21 Spatiotemporal evolution of the membrane action potential and the effect of an external stimulus on wave patterns. It has been plotted for (a)$I_{ext} = 0.60$, (b) $I_{ext} = 1.0$ and (c) $I_{ext} = 1.4$ for K=10.0 . . . 106

Figure 3.22 Developed spatiotemporal pattern and time series calculated for the constant frequency external electromagnetic radiation intensity $A = 0.04$, with $f = 0.2$ and $I_{ext} = 1.418$ 107

Figure 3.23 Spatiotemporal evolution of the membrane action potential and the effect of an external electromagnetic radiation intensity on wave patterns. It has been plotted for $A = 0.055$, $A = 0.065$ and $A = 0.075$, from Left to Right. 107

Figure 3.24 Spatiotemporal evolution for different frequencies of external electromagnetic radiation, (a) f=0.002, (b) f=0.02, and (c) f=0.04, with A=0.05 108

Figure 3.25 Corresponding time series evolution for different frequencies of external electromagnetic radiation for parameter values illustrated by Figs. (3.24). The intensity increases from Top to Bottom. 108

Figure 3.26 Spatiotemporal evolution of the cardiac ionic wave in all the computational domains: (a) 3D view of the traveling cardiac pulse, (b) upper view, and (c) spatial ionic wave profiles at t=10. Signal appears in the form of a nearly symmetric wave packet. $k_0 = 1.0, q = 0.02\pi, \epsilon = 0.01, A_0 = 0.01$ and t=3010 109

Figure 3.27 Impacts of small perturbations on the cardiac ionic wave. $k_0 = 1.0, q = 0.02\pi, A_0 = 0.001$ and t=3010 110

Figure 3.28 Impact of electromagnetic induction on the cardiac ionic wave. $q = 0.02\pi, A_0 = 0.001$ and t=3010 110

Figure 3.29 Spatiotemporal evolution of the cardiac ionic wave in all the computational domains: (a) 3D view of the traveling cardiac pulse, (b) upper view, and (c) spatial ionic wave profiles at $t = 10$. Signal appears in the form of an asymmetric wave packet. The parametric values are; $D_0 = 0.05, k_0 = 1.0, q = 0.02\pi, \epsilon = 0.70$ and $A_0 = 1.00$. 111

Figure 3.30 Ionic wave profiles at different times 112

Figure 3.31 Impacts of small perturbations on the cardiac ionic wave (a) $\epsilon = 0.05$, (b) $\epsilon = 0.1$ and (c) $\epsilon = 0.6$ 112

Figure 3.32 Time behavior of the cardiac ionic wave. The rest parameter values are: $D_0 = 0.05, k_0 = 1.0, q = 0.1\pi, \epsilon = 0.30$ and $A_0 = 0.02$ 113

List of Abbreviations

Initials	Meaning	**Initials**	Meaning
NNs	Neural networks	**NLS**	Nonlinear Schrödinger
HR	Hindmarsh-Rose	**DNLS**	Discrete nonlinear Schrödinger
HH	Hodgkin-Huxley	**CGL**	Complex Ginzburg-Landau
FHN	FitzHugh-Nagumo	**MFE**	Magnetic flow effect
IF	Integrate-and-fire	**MSC**	Memristive synaptic coupling
ML	Morris-Lecar	**ODEs**	Ordinary differential equations
MF	Magnetic flow	**EEG**	Electroencephalography
EMI	Electromagnetic induction	**IBI**	Inter-burst interval
EMR	Electromagnetic radiation	**SDA**	Semi-discrete approximation
MI	Modulational instability	**RK4**	Fourth-order Runge-Kutta
NA	Neuronal activity	**NS**	Neuronal synchronization
CNS	Central nervous system	**EPSPs**	Excitatory post synaptic potentials
MC	Memristor coupling	**GABA**	G-Amino-Butyric Acid
DNA	Deoxyribonucleic acid	**WP**	Waves propagation

Résumé

Nous traitons l'effet conjoint de l'induction et de la radiation électromagnétique sur l'activité électrique des cellules biologiques excitables. Après une adéquate modélisation théorique, des méthodes mathématiques et numériques appropriées sont utilisées pour étudier chaque phénomène. Du point de vue biophysique, nous montrons que des ondes initiées à partir du nœud sinusoidal du cœur se propagent dans les cellules du myocarde sous forme d'excitations solitoniques modulées, régulant ainsi les pulsations cardiaques en tant que stimulateur. En outre, il est révélé que le modèle amélioré avec induction électromagnétique peut également conduire à la formation des structures spatio-temporelles non-linéaires et quasi-périodiques dont certaines ont un comportement quasi-synchrone. Par ailleurs, l'induction électromagnétique dans les réseaux de neurones pourrait également contribuer aux comportements coopératifs et collectifs des neurones thalamocorticaux. En présence d'un fort rayonnement électromagnétique, on observe la disparition progressive des motifs. Ce qui pourrait être assimilé à une conduction bloquée pendant la propagation du signal. Cela pourrait fournir des indications et une meilleure compréhension des insuffisances cardiaques et nerveuses soudaines lorsque les cellules sont exposées à un rayonnement électromagnétique élevé. L'application de la stimulation magnétique trans-crânienne présent un avantage car les boucles électriques cérébrales anormales peuvent être corrigées. Ceci constitue une méthode de correction indirecte qui pourrait aider à éviter des blessures graves dans le ceveau.

Mots clés: Cellules du myocarde; les neurones; induction électromagnétique; rayonnement; excitations non- linéaires; synchronisation; stimulation magnétique; intelligence artificielle.

Abstract

This thesis deals with the effects of electromagnetic induction and radiation on the electrical activity of biological excitable cells. After a good physical and mathematical modeling of biological excitable cells with electromagnetic induction and exposure to electromagnetic field, appropriate mathematical and numerical methods are used to investigate the action of each phenomenon on the electrical activity of cells. It is found from biophysical point of view that cardiac electrical signals or waves initiated from the heart sinus node propagate in myocardial cells both in temporal and spatial dimensions in the form of a localized modulated solitonic wave thereby regulating heartbeat as powerful pacemaker. Also, it is revealed that the improved model with electromagnetic induction can also lead to the formation of nonlinear quasi-periodic spatiotemporal patterns with some features of synchronization. The generation of pulses and rhythmics behaviors like breathing or swimming are highly relevant in brain researches. Furthermore, electromagnetic induction in neural networks could also contributes to the co-operative and collective behaviors of the thalamocortical neurons. In the presence of electromagnetic radiation, the formation of periodic pulse train presents disappearing pattern, which could be likened to conduction blocked during signal propagation. This could provide guidance and better understanding of sudden heart failure exposed to heavily electromagnetic radiation. Currently, neuro-computer scientists simulate the rich and complex behaviors of biological neural networks to develop artificial neural networks for the improvement of artificial intelligence. The application of trans-cranial magnetic stimulation is a fruitful avenue where abnormal brain electrical loop can be corrected. This constitutes the non-direct invasive method of correction which could help avoid major injury during the event of administration as the case may be with direct electrical stimulation.

Keywords: Myocardial cells; neurons; electromagnetic induction and radiation; spatiotemporal patterns; neuronal synchronization; magnetic stimulation; artificial intelligence.

General Introduction

Excitable systems are, in general, spatially distributed systems which as a result of application of a super-threshold stimulus, are able to generate and conduct nonlinear waves of excitation. Biological examples of excitable media include electrical membrane excitation in nerves of the brain (neurons) and muscular tissue of the heart (myocardial cells), intracellular waves of calcium induced calcium release and some simple morphogenetic systems. Studies of the brain and the heart using methods of nonlinear science resulted in the development of the concept of an excitable medium, which is currently one of the most developed and important branches of modern computational biology [1].

The heart is made up of cardiac conducting cells helping to initiate and propagate the action potential (the electrical impulse) that travels throughout the heart and triggers the contractions that propel the blood to the rest of the body. The human heart is known to beat about $2-3$ billion times in a normal life span [2]. Under an unhealthy condition, the heart may lose its normal rhythm, degenerating into a sudden much faster and irregular rhythms, known as arrhythmias [3]. The actual transition from a normal healthy rhythm to a lethal rhythm is known to be a transition from regular electrical wave conduction to an irregular, turbulent wave conduction in the heart. This is a clear medical problem, which is also a problem of Mathematics, Physics and Biophysics, respectively.

The brain is the most important but highly complex system in nature. It forms an integral part of the nervous system and made up of a large number of neurons grouped into functional ensembles generally called micro-circuits [4]. The neurons form the basic, structural and functional units of information encoding and transmission within the brain. Thus, they initiate and propagate the electrical impulse. Reliable micro-circuits are crucial in discerning the potential mechanism of signal encoding and propagation in the brain, which is one of the challenges of modern neuroscience.

This baroque complexities of cardiac and nervous system require some strong computational treatments safely guided by mathematical insights, based on simple nonlinear

systems, or rationally reduced models. The FitzHugh-Nagumo (FHN) model [5,6] in the discrete form is extended to include the effect of electromagnetic induction and radiation, hence analytical and numerical techniques applied to study phenomena of spatiotemporal pattern formation and neuronal synchronization (NS).

0.1 Context of the thesis

The biological Hodgkin-Huxley (HH) [7] neuron model has been available for bifurcation analysis and understanding the dynamical response to external stimuli, synchronization stability and evolution of collective behaviors under coupling. Based on this neuron model, dynamical analysis is carried out on the isolate neuron model, particularly, coherence resonance and stochastic resonance are induced by imposing appropriate noise. As a result, distinct regularity can be found in the sampled time series for membrane potentials. Furthermore, collective behaviors are investigated on the neuronal network connected with different topological connection, such as synchronization transition, pattern selection in the network. These results are important and helpful to understand potential mechanism for occurrence of neuronal disease. So, reliable schemes can be presented to prevent the breakdown of neuronal systems. Many simplified HH models have been proposed; FHN model, Integrate-and-fire model [8], Morris-Lecar (ML) model [9], Hindmarsh-Rose model [10–12] and Izhikevich model [13, 14].

However, the excitability property of neuron is much too complex and many factors should be considered as well. According to the Faraday's law of induction, the fluctuation or changes in action potentials in excitable cells (neurons) can generate magnet field in the media; in that sense, the excitability of neurons will be adjusted under feedback effect [15,16]. Albeit the satisfactory results reported in the above mentioned studies, the appropriate mechanism and the conditions under which spatiotemporal patterns emerge and spread among coupled neurons under electromagnetic induction have been not investigated. Therefore, it is important to set more reliable FHN models so that the effect of electromagnetic induction could be considered.

Myocardial cell excitations are also too complex [17–19] and many realistic biological and physical factors should be included during the control of disease and dynamical analysis. Complex electrophysiological activities in electrical activities and excitation dynamics have been detected and widely reported in cardiac tissues [20–22]. These spatial

patterns can be reproduced and observed by collecting the sampled membrane potentials in different areas of myocardial tissue [23]. Many iterated maps of action potential [24] and theoretical model [25, 26] have been proposed to study these patterns in relation to its emergence, phase transition and pattern selection. In fact, it has been argued that as a result of these complex electrophysiological conditions, complex distribution of electromagnetic field can be detected in cells [27, 28]. This implies, the dynamical behavior of each cell can be changed according to Maxwell electromagnetic induction theorem. On this background, the magnetic flux and memristor are used to develop a more reliable model. Magnetic flux is used to describe the change and distribution of electromagnetic field, while memristor couples the magnetic flux change to the membrane action potential. Magnetic flux has been recently used to model the effect of electromagnetic induction on the trans-membrane potential of neurons [29]. Indeed, the effect of electromagnetic radiation can be detected and investigated when neuron or cell is exposed to electromagnetic field. As a result of this exposure, the excitability of cells should be adjusted under feedback effect [30]. Albeit the satisfactory results reported in the above mentioned studies, the appropriate different mechanisms and conditions under which spatiotemporal patterns emerge and spread among coupled myocardial cells under electromagnetic radiation have not received enough investigations relevant for disease prediction and understanding. This constitute a strong motivation of the present work. It is thus highly relevant to discuss the onset and condition of the formation of modulated waves patterns in a network of coupled myocardial cells and neurons mediated by modulational instablity(MI).

MI is one of the direct mechanism well documented that leads to the formation of solitons and train of waves in systems where there are permanent competitive effects between non-linearity and dispersion [31, 132]. Meier *et al.* [33], realized the first experimental observation of MI in physical systems. We show in this work, that the effect of electromagnetic induction and radiation can enhance spatiotemporal information through the activation of MI. Through numerical experiment, the myocardial cell lattice reveals to support the generation of localized modes, soliton-like in shape with breathing motion, which are relevant in cardiac researches. Furthermore, the potential mechanism of external electromagnetic radiation-induced heart disease via pattern formation will be discussed.

0.2 Problematic and objectives of the thesis

Rapid industrial expansion and technological improvement have gradually increased the exposure of man to the lethal effect of electromagnetic radiation throughout the last century. These high exposures are contributed from the increased use of electromagnetic portable instruments, multiplications of electrical devices in flats, nearness of manufacturing industries to the domain of habitations. This has increased the level of electromagnetic interactions in human biological cells, notably the cells of the brain and the heart. These interactions have been widely suggested to be responsible for some neuro-degenerative diseases such as the more pathological forms of behavior like multiple sclerosis, Alzheimer, migraines, epileptic seizures, Parkinson diseases etc. [34–36].

Cardiovascular disease is the major prevailing cause of death worldwide and accounts for about a third of all deaths [37]. This disease may arise due to defects in the blood vessels, arteries or veins resulting to heart attacks and strokes. These defects may also disrupt the normal contraction of the ventricles, resulting in heart failure and impaired blood supply. An abnormal or irregular heart rhythm, including atrial and ventricular fibrillation as well as ventricular tachycardia, are closely associated with the loss of rhythm and synchronization of cardiac electrical impulses which initiate the pumping of blood.

Maintaining the optimal electrical activities of neurons are highly important for humans as any breakdown due from any external attack can lead to the collapse of brain resulting to serious diseases and even death in case of injury of the nervous system. Lisi *et al.* [38], reported the effect of electromagnetic radiations at a frequency of 50 Hz on the development of newborn rat cerebellar granule neurons. Xu *et al.* [39], also investigated the oxidative damage to mitochondrial DNA in primary cultured neurons exposed to 1,800 MHz radio frequency radiation. For more review on the biological phenomena effect of electromagnetic radiation, readers can find survey in [40,41] and references therein. However, the effect of electromagnetic induction, injury on neuron and electromagnetic radiation is still under investigation relevant for disease discerning, predictions and control. Indeed, electromagnetic induction and radiation [42, 43], injury on neurons [44] can cause serious nervous disorder due to the blocking of signal propagation and encoding in neural activities. Zhang et *al.* [45], setup a reliable model with memristive synapse and discussed spatial patterns emergence under electromagnetic induction. However, the appropriate conditions and mechanism under which spatiotemporal patterns emerge and

spread among the reliable neural networks under the effect of electromagnetic induction and radiation, have not yet fully been unmasked and deserve to be properly investigated. This constitutes the strong motivation to this work. In this thesis, the combination of analytical and numerical methods is used to study waves propagation and neuronal synchronization phenomena in the context of the transport and transfer of impulses in cardiac tissue and neural networks in order to light, the effects of electromagnetic induction and radiation.

0.3 Organization of the Thesis

This thesis is divided into three chapters that are outlined as follows:

✠ The first chapter, the biology of cardiac tissue and neuronal networks, focuses on the biological excitable cells; the organization and properties of myocardial cells and neurons as the basic units of cardiac excitation and information processing in the nervous system respectively. Their networks are then viewed as the macroscopic structures for the transport of impulses during signal encoding. In this chapter some of the most prominent neural models are presented and resulting in the choice of the FHN model whose properties are well discussed.

✠ Chapter 2, the improved models of FHN and methodologies, presents the different mathematical models developed in this thesis as well as the analytical and numerical methods used. Some immediate applications are made in order to facilitate the understanding of the methods. Interestingly, a discrete nonlinear Schrödinger (DNLS) and a complex Ginzburg-Landau (CGL) equations are derived from generic model and allow to find analytical expression of some MI functions such as critical amplitude or MI gain along with instability criterion.

✠ The third chapter, results and discussions, is devoted to obtained results and biophysical implications. We first discuss the effects of electromagnetic induction and radiation on single-channel neuronal communication and secondly on the myocardial cells . Then the high frequency mode is studied in a discrete model of one-dimensional FHN network. We end this study by reporting the possibility of emphatic communication via memristive electromagnetic induction.

The thesis ends with a general conclusion including the summary of the main results and the futures orientations.

Chapter 1

Literature review: The Biology of Cardiac Tissue and Neuronal Networks

Introduction

Cardiac tissue are made up of two major types of cardiac muscle cells: myocardial contractile cells and myocardial conducting cells. The myocardial contractile cells constitute the bulk (99%) of the cells in the atria and ventricles. Contractile cells conduct impulses and are responsible for contractions that pump blood through the body. The myocardial conducting cells (1% of the cells) form the conduction system of the heart. Except for Purkinje cells, they are generally much smaller than the contractile cells and have few of the myofibrils or filaments needed for contraction. Their function is similar in many respects to neurons, although they are specialized muscle cells. Myocardial conduction cells initiate and propagate the action potential (the electrical impulse) that travels throughout the heart and triggers the contractions that propel the blood. Recall that cardiac muscle shares a few characteristics with both skeletal muscle and smooth muscle, but it has some unique properties of its own. Not the least of these exceptional properties is its ability to initiate an electrical potential at a fixed rate that spreads rapidly from cell to cell to trigger the contractile mechanism. This property is known as auto-rhythmicity. Neither smooth nor skeletal muscle can do this. Even though cardiac muscle has auto-rhythmicity, heart rate is modulated by the endocrine and nervous systems.

The human brain is made up of about one hundred billion neurons that communicate with each other through synaptic nodes. These neurons are analog units that work

together, performing very sophisticated operations of cognitive and control functions. Neurons communicate by means of electrical impulses (action potentials). The evolution in time of these impulses forms a complex code that supports the treatment of the nervous message. Obviously, the emission of an action potential by a neuron is favored by the electrical properties of its plasma membrane which is ionically permeable. The abundance of neurons in the cerebral tissue sometimes confers them complex and different morphologies, but still retains a basic structure consisting of a cell body, an axon and dendrites.

Naturally in the brain, each neuron can have approximatively ten thousand connections with other neurons, totaling a million billion electrochemical interactions in the nervous system. Neurons interacting with each other via synapses form a network that constitutes a very sophisticated and complex communication system. In a neurons family, the knowledge of inherent properties of individual neuron does not necessarily allow the knowledge of the properties of the network, since the electrical activity of each neuron is influenced by those of the others to which it is connected likewise the conducting cells in the heart. In particular the chemical substances of a given afferent neuron as well as transient electric field produced from a population of spikes for interneuronal communication may enhance nerve impulse transmission. This once more makes the phenomenon of myocardial and neuronal activities very ambiguous.

To remove the equivocation, researchers have built, on the basis of experimental results, mathematical models, more or less simple, to simulate the different behavior of neurons and myocardial cells. Thanks to these mathematical models, it is henceforth possible to obtain spike-shaped patterns like those obtained by Hodgkin and Huxley via experiment on the giant squid axon. Additionally, most of the behaviors related to a neural network and cardiac tissue are accurately reproduced through these models, although most of which not having biologically specificity, have universal physical fundamentals.

This chapter is divided into four main parts. The first part presents; the structure of cardiac muscle, the components of the conducting system that distributes electrical impulses through the heart, the comparison of the effect of ion movement on membrane potential of cardiac conductive and contractile cells, the related characteristics of an electrocardiogram to events in the cardiac cycle and the identification of blocks that can interrupt the cardiac cycle. The second part presents; the neuron as the basic unit of the nervous system with a particular emphasis on its structure and functions, and the properties of action potential. The third part presents the highlights of the role of synapses

in the transmission of nerve impulses from one neuron to another in a neural network. Finally we comment on the most famous mathematical models in the qualitative and quantitative description of the electrical activity of neurons.

1.1 Cardiac Muscle and Electrical Activity

The heart is made up of cardiac conducting cells helping to initiate and propagate the action potential (the electrical impulse) that travels throughout the heart and triggers the contractions that propel the blood to the rest of the body. As for the most of the biological systems, structure and various functions are closely dependent.

1.1.1 Structure of Cardiac muscle

Compared to the giant cylinders of skeletal muscle, cardiac muscle cells, or cardiomyocytes, are considerably shorter with much smaller diameters. Cardiac muscle also demonstrates striations, the alternating pattern of dark A bands and light I bands attributed to the precise arrangement of the myofilaments and fibrils that are organized in sarcomeres along the length of the cell. These contractile elements are virtually identical to skeletal muscle. T (transverse) tubules penetrate from the surface plasma membrane, the sarcolemma, to the interior of the cell, allowing the electrical impulse to reach the interior. The T tubules are only found at the Z discs, whereas in skeletal muscle, they are found at the junction of the A and I bands. Therefore, there are one-half as many T tubules in cardiac muscle as in skeletal muscle. In addition, the sarcoplasmic reticulum stores few calcium ions, so most of the calcium ions must come from outside the cells. The result is a slower onset of contraction. Mitochondria are plentiful, providing energy for the contractions of the heart. Typically, cardiomyocytes have a single, central nucleus, but two or more nuclei may be found in some cells. Cardiac muscle cells branch freely. A junction between two adjoining cells is marked by a critical structure called an intercalated disc, which helps support the synchronized contraction of the muscle. The sarcolemmas from adjacent cells bind together at the intercalated discs. They consist of desmosomes, specialized linking proteoglycans, tight junctions, and large numbers of gap junctions that allow the passage of ions between the cells and help to synchronize the contraction. Intercellular connective tissue also helps to bind the cells together. The importance of strongly binding these cells together is necessitated by the forces exerted

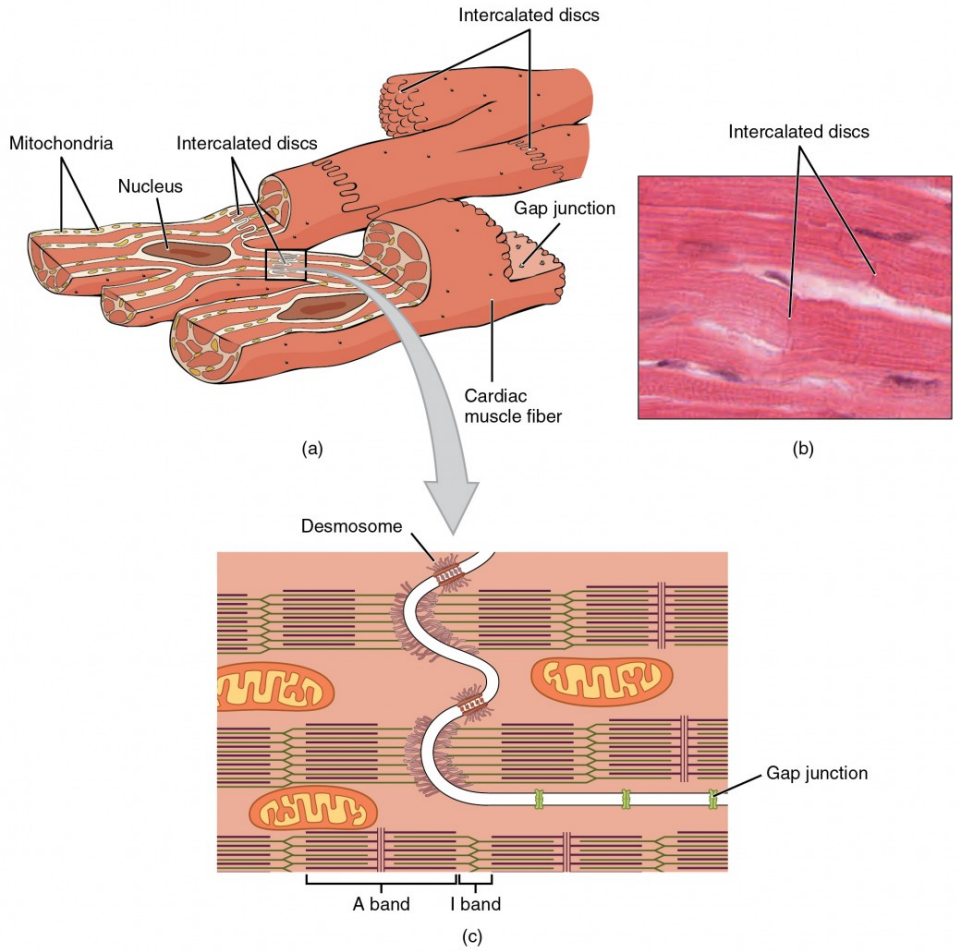

Figure 1.1: (a) Cardiac muscle cells with myofibrils composed of myofilaments arranged in sarcomeres, T tubules to transmit the impulse from the sarcolemma to the interior of the cell, numerous mitochondria for energy, and intercalated discs that are found at the junction of different cardiac muscle cells. (b) A photomicrograph of cardiac muscle cells shows the nuclei and intercalated discs. (c) An intercalated disc connects cardiac muscle cells and consists of desmosomes and gap junctions. $LM1600$. (Micrograph provided by the Regents of the University of Michigan Medical School ľ 2012) [46].

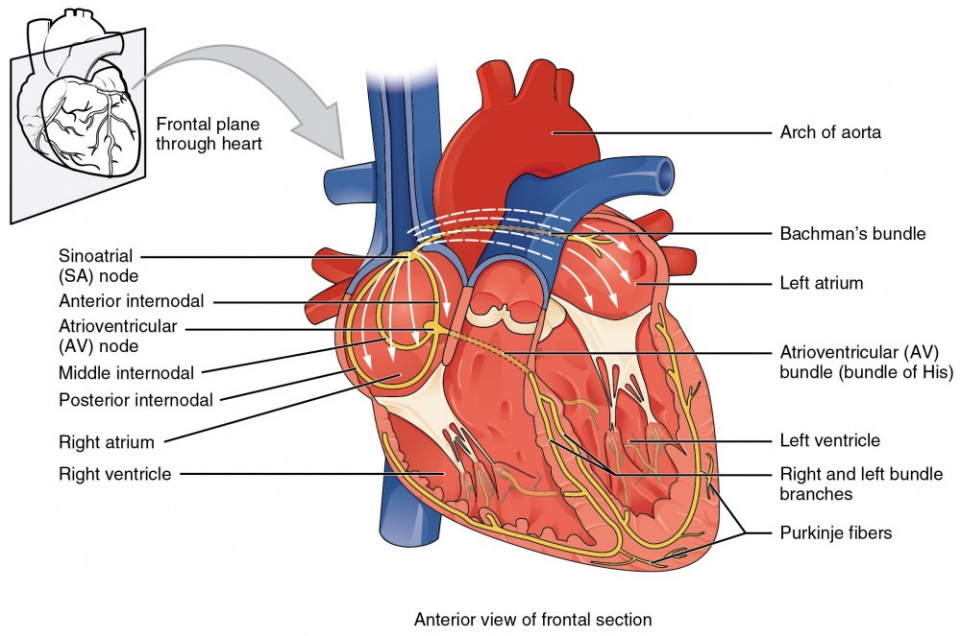

Figure 1.2: Specialized conducting components of the heart; the sinoatrial node, the internodal pathways, the atrioventricular node, the atrioventricular bundle, the right and left bundle branches, and the Purkinje fibers [46].

by contraction(see Fig.1.1).

1.1.2 Conduction System of the Heart

If embryonic heart cells are separated into a Petri dish and kept alive, each is capable of generating its own electrical impulse followed by contraction. When two independently beating embryonic cardiac muscle cells are placed together, the cell with the higher inherent rate sets the pace, and the impulse spreads from the faster to the slower cell to trigger a contraction. As more cells are joined together, the fastest cell continues to assume control of the rate. A fully developed adult heart maintains the capability of generating its own electrical impulse, triggered by the fastest cells, as part of the cardiac conduction system. The components of the cardiac conduction system include the sinoatrial node, the atrioventricular node, the atrioventricular bundle, the atrioventricular bundle branches, and the Purkinje cells.

Sinoatrial (SA) **Node** is a specialized clump of myocardial conducting cells located in the superior and posterior walls of the right atrium in close proximity to the orifice of the superior vena cava. Normal cardiac rhythm is established by the sinoatrial (SA)

node. The SA node has the highest inherent rate of depolarization and is known as the pacemaker of the heart. It initiates the sinus rhythm, or normal electrical pattern followed by contraction of the heart. This impulse spreads from its initiation in the SA node throughout the atria through specialized internodal pathways, to the atrial myocardial contractile cells and the atrioventricular node. The internodal pathways consist of three bands (anterior, middle, and posterior) that lead directly from the SA node to the next node in the conduction system, the atrioventricular node. The impulse takes approximately 50 ms (milliseconds) to travel between these two nodes. The relative importance of this pathway has been debated since the impulse would reach the atrioventricular node simply following the cell-by-cell pathway through the contractile cells of the myocardium in the atria. In addition, there is a specialized pathway called BachmannŠs bundle or the interatrial band that conducts the impulse directly from the right atrium to the left atrium. Regardless of the pathway, as the impulse reaches the atrioventricular septum, the connective tissue of the cardiac skeleton prevents the impulse from spreading into the myocardial cells in the ventricles except at the atrioventricular node. *Fig*.1.3 illustrates the initiation of the impulse in the *SA* node that then spreads the impulse throughout the atria to the atrioventricular node.

The electrical event, the wave of depolarization, is the trigger for muscular contraction. The wave of depolarization begins in the right atrium, and the impulse spreads across the superior portions of both atria and then down through the contractile cells. The contractile cells then begin contraction from the superior to the inferior portions of the atria, efficiently pumping blood into the ventricles.

Atrioventricular (*AV*) Node is a second clump of specialized myocardial conductive cells, located in the inferior portion of the right atrium within the atrioventricular septum. The septum prevents the impulse from spreading directly to the ventricles without passing through the AV node. There is a critical pause before the AV node depolarizes and transmits the impulse to the atrioventricular bundle(see image above, step 3). This delay in transmission is partially attributable to the small diameter of the cells of the node, which slow the impulse. Also, conduction between nodal cells is less efficient than between conducting cells. These factors mean that it takes the impulse approximately 100 ms to pass through the node. This pause is critical to heart function, as it allows the atrial cardiomyocytes to complete their contraction that pumps blood into the ventricles before the impulse is transmitted to the cells of the ventricle itself. With extreme stimulation

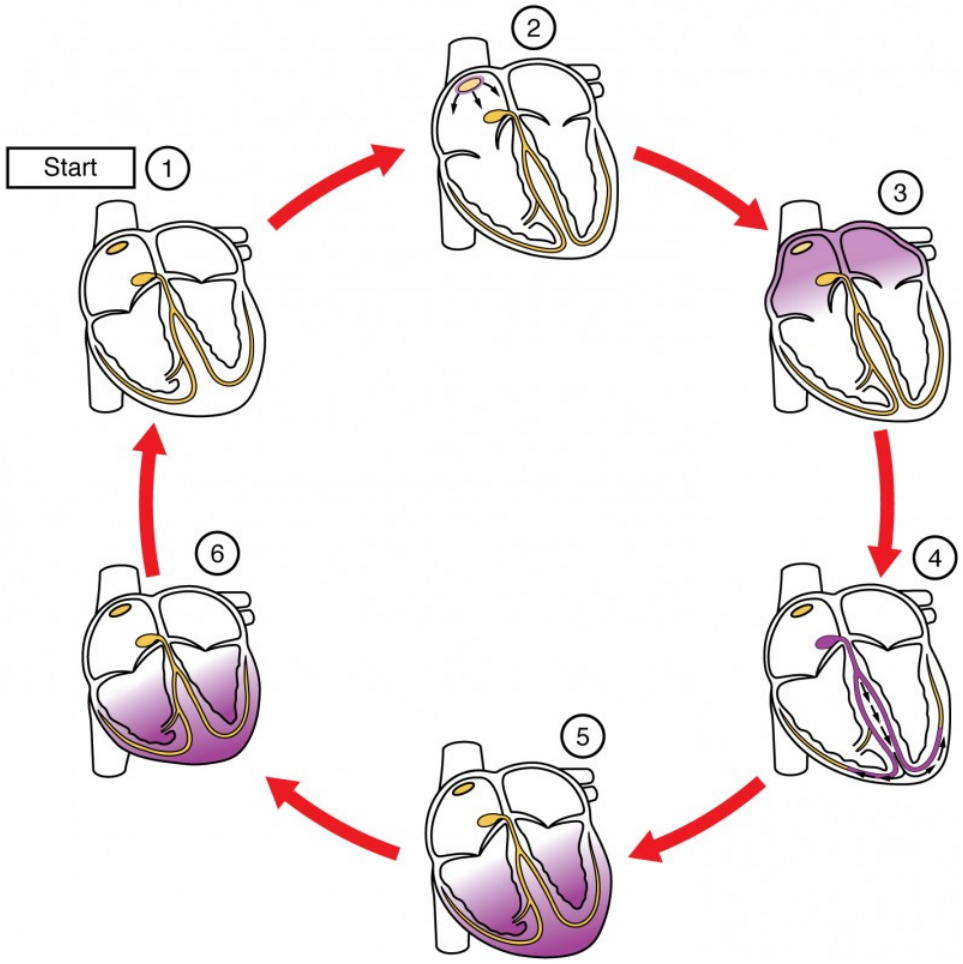

Figure 1.3: (1) The sinoatrial (SA) node and the remainder of the conduction system are at rest. (2) The SA node initiates the action potential, which sweeps across the atria. (3) After reaching the atrioventricular node, there is a delay of approximately 100 ms that allows the atria to complete pumping blood before the impulse is transmitted to the atrioventricular bundle. (4) Following the delay, the impulse travels through the atrioventricular bundle and bundle branches to the Purkinje fibers, and also reaches the right papillary muscle via the moderator band. (5) The impulse spreads to the contractile fibers of the ventricle. (6) Ventricular contraction begins. [46].

by the SA node, the AV node can transmit impulses maximally at 220 per minute. This establishes the typical maximum heart rate in a healthy young individual. Damaged hearts or those stimulated by drugs can contract at higher rates, but at these rates, the heart can no longer effectively pump blood.

Atrioventricular Bundle (Bundle of His), Bundle Branches, and Purkinje Fibers proceeds through the interventricular septum before dividing into two atrioventricular bundle branches, commonly called the left and right bundle branches. The left bundle branch has two fascicles. The left bundle branch supplies the left ventricle, and the right bundle branch the right ventricle. Since the left ventricle is much larger than the right, the left bundle branch is also considerably larger than the right. Portions of the right bundle branch are found in the moderator band and supply the right papillary muscles. Because of this connection, each papillary muscle receives the impulse at approximately the same time, so they begin to contract simultaneously just prior to the remainder of the myocardial contractile cells of the ventricles. This is believed to allow tension to develop on the chordae tendineae prior to right ventricular contraction. There is no corresponding moderator band on the left. Both bundle branches descend and reach the apex of the heart where they connect with the Purkinje fibers (see image above, step 4). This passage takes approximately 25 ms.

Purkinje fibers are additional myocardial conductive fibers that spread the impulse to the myocardial contractile cells in the ventricles. They extend throughout the myocardium from the apex of the heart toward the atrioventricular septum and the base of the heart. The Purkinje fibers have a fast inherent conduction rate, and the electrical impulse reaches all of the ventricular muscle cells in about 75 ms (see image above, step 5). Since the electrical stimulus begins at the apex, the contraction also begins at the apex and travels toward the base of the heart, similar to squeezing a tube of toothpaste from the bottom. This allows the blood to be pumped out of the ventricles and into the aorta and pulmonary trunk. The total time elapsed from the initiation of the impulse in the SA node until depolarization of the ventricles is approximately 225 ms.

1.1.3 Membrane Potentials and Ion Movement in Cardiac Conductive Cells

Action potentials are considerably different between cardiac conductive cells and cardiac contractive cells. While Na^+ and K^+ play essential roles, Ca^{2+} is also critical for

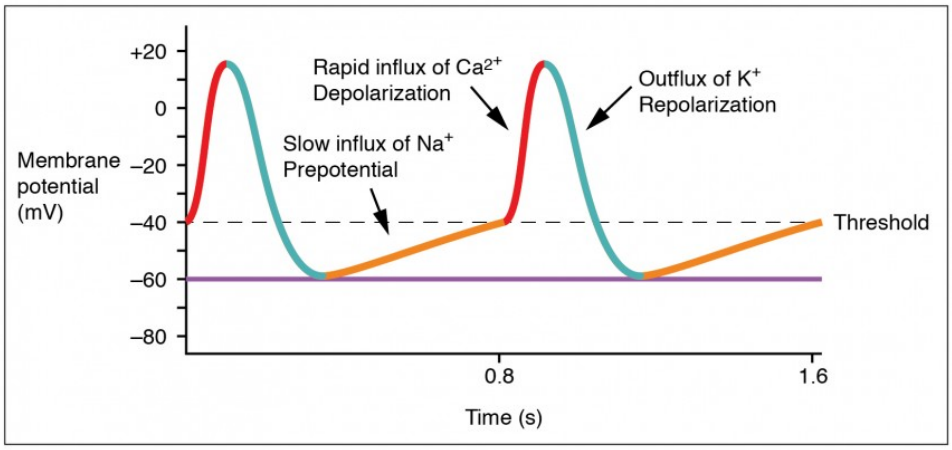

Figure 1.4: The prepotential is due to a slow influx of sodium ions until the threshold is reached followed by a rapid depolarization and repolarization. The prepotential accounts for the membrane reaching threshold and initiates the spontaneous depolarization and contraction of the cell. We note the lack of a resting potential [46].

both types of cells. Unlike skeletal muscles and neurons, cardiac conductive cells do not have a stable resting potential. Conductive cells contain a series of sodium ion channels that allow a normal and slow influx of sodium ions that causes the membrane potential to rise slowly from an initial value of -60 mV up to about 40 mV. The resulting movement of sodium ions creates spontaneous depolarization (or pre-potential depolarization). At this point, calcium ion channels open and Ca^{2+} enters the cell, further depolarizing it at a more rapid rate until it reaches a value of approximately $+5$ mV. At this point, the calcium ion channels close and K^+ channels open, allowing out flux of K^+ and resulting in repolarization. When the membrane potential reaches approximately -60 mV, the K^+ channels close and Na^+ channels open, and the prepotential phase begins again. This phenomenon explains the auto-rhythmicity properties of cardiac muscle (Fig.1.8).

1.1.4 Comparative Rates of Conduction System Firing

The pattern of prepotential or spontaneous depolarization, followed by rapid depolarization and repolarization just described, are seen in the SA node and a few other conductive cells in the heart. Since the SA node is the pacemaker, it reaches threshold faster than any other component of the conduction system. It will initiate the impulses spreading to the other conducting cells. The SA node, without nervous or endocrine control, would initiate a heart impulse approximately $80 - 100$ times per minute. Although

each component of the conduction system is capable of generating its own impulse, the rate progressively slows as you proceed from the SA node to the Purkinje fibers. Without the SA node, the AV node would generate a heart rate of $40-60$ beats per minute. If the AV node were blocked, the atrioventricular bundle would fire at a rate of approximately $30-40$ impulses per minute. The bundle branches would have an inherent rate of $20-30$ impulses per minute, and the Purkinje fibers would fire at $15-20$ impulses per minute. While a few exceptionally trained aerobic athletes demonstrate resting heart rates in the range of $30-40$ beats per minute (the lowest recorded figure is 28 beats per minute for Miguel Indurain, a cyclist), for most individuals, rates lower than 50 beats per minute would indicate a condition called bradycardia. Depending upon the specific individual, as rates fall much below this level, the heart would be unable to maintain adequate flow of blood to vital tissues, initially resulting in decreasing loss of function across the systems, unconsciousness, and ultimately death.

1.2 Neurons

Neurons are nervous cells specialized either in the reception of the nerve impulse coming from the brain, or in the transmission of this nerve impulse towards the brain.

1.2.1 Structure and Functions

There is a wide variety of neurons, with different shapes and sizes. However, they all have a common structure (see Fig.1.9) comprising:

- the cell body, also called the soma,
- numerous short processes of the soma, called the dendrites; and,
- the single long nerve fiber, the axon.

The body of a nerve cell is similar to that of all other cells. The cell body generally includes the nucleus, mitochondria, endoplasmic reticulum, ribosomes, and other organelles. Nerve cells contain about $70-80\%$ water; the dry material is about 80% protein and 20% lipid. The cell volume varies between 600 and 70.000 μmL. The soma, or cell body, is the processing center of a neuron. When it receives information, it processes it and, if it is sufficient important relative to a certain threshold, sends a signal into the axon. The

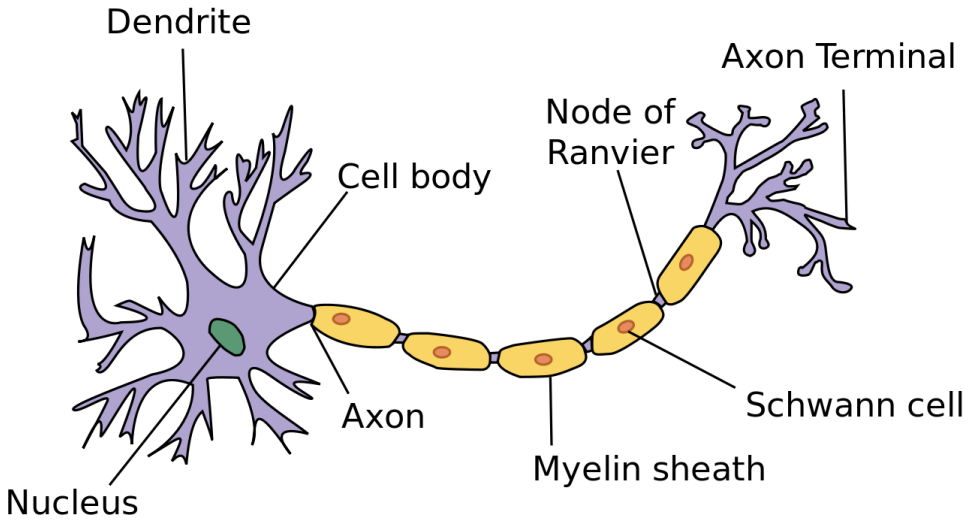

Figure 1.5: Annotated diagram of a neuron [47].

unique feature of the cell body is that it is the only part of a neuron that contains a cell nucleus in which DNA molecule is confined. Most RNA in a neuron is produced by the cell nucleus. Therefore, most proteins are produced in the cell body and then transported to the entire neuron.

Dendrites are a multiple extensions that arise at the level of the soma to branch out as a tree. They function as an "antennae" of the neuron and are covered by thousands of synapses. They ensure the continuity of the propagation of information between the different neurons that make up the information path. When we move away from the soma, the dendrites diameter decreases, what differ them from the axon whose diameter remains almost uniform, except on the the axonal terminations level. Dendrites receive electrical impulses passed by other neurons and propagate them to the cell body. The dendritic membrane under the synapse (the post-synaptic membrane) has many specialized protein molecules called receptors that detect the neurotransmitters in the synaptic cleft.

The axon is the main conducting unit of the neuron, capable of conveying electrical signals from the soma, along distances that range from as short as $0.1mm$ to as long as $2m$. Many axon split into several branches, thereby conveying information to different targets. Many neurons do not have axons. For instance, in amacrine neurons, all the neuronal processes are dendrites. Neurons with very short axons are also found. The axons of many neurons are wrapped in a myelin sheat, which is composed of the membranes of intersticial cells and is wrapped around the axons to form several concentric layers. The myelin sheath is broken at various points by the nodes of Ranvier, so that in cross section

it looks like a string of sausages. The myelin protects the axon, and prevents interference between axons as they pass along in bundles, sometimes thousands at time. The cells that wrap around peripheral nerve fibers (nerve fibers outside of the brain and spinal cord) are called Schwann cells (because they were first described by Theodor Schwann). The cells that wrap around axons within the central nervous system (brain and spinal cord) are called oligodendrocytes. The axon, with its surrounded sheath, is called a nerve fiber. Between each pair of successive Schwann cells is a gap or a node of Ranvier. The axon hillock is where the axon is joined to the cell body. It is from here that the electrical firing, known as an action potential, usually occurs.

1.2.2 Classification of neurons

We encounter structural and functional classification of neurons. Structurally, neurons are classified by the number of processes that originate from the cell body. For this purpose, we have four types of neurons: anaxonic neurons, bipolar neurons, pseudounipolar neurons and multipolar neurons as shown in Fig.1.2.

Anaxonic neurons have dendrites, but no axons. They produce local electrical variations (graded potential), but no action potential.

Bipolar neurons have two extensions that emerge from the cell body: a dendrite and an axon; they are present in certain sense organs, eg, in the retina, the inner ear, and the olfactory mucosa.

Pseudounipolar neurons have a simple and short extension. They are divided into two extensions in T-shaped: one goes towards the central nervous system (CNS), peripheral extension (dendrites to the cell body); and the other, towards the peripheral nervous system, central extension (cell body to the CNS). These two extensions constitute a single long axon.

Multipolar neurons represent the most common type; they have many dendrites and a single axon.

Functionally, neurons can be divided into three functional classes namely sensory (afferent) neurons, interneurons and efferent (somatic motor and autonomic) neurons.

Afferent neurons carry information about temperature, pressure, light, and other stimuli from sensory receptor to the CNS. Sensory neurons or afferent neurons are unipolar, bipolar, or multipolar shaped cells that conduct action potentials toward or into the central nervous system. They carry somatic nervous system signals from the skin, joints,

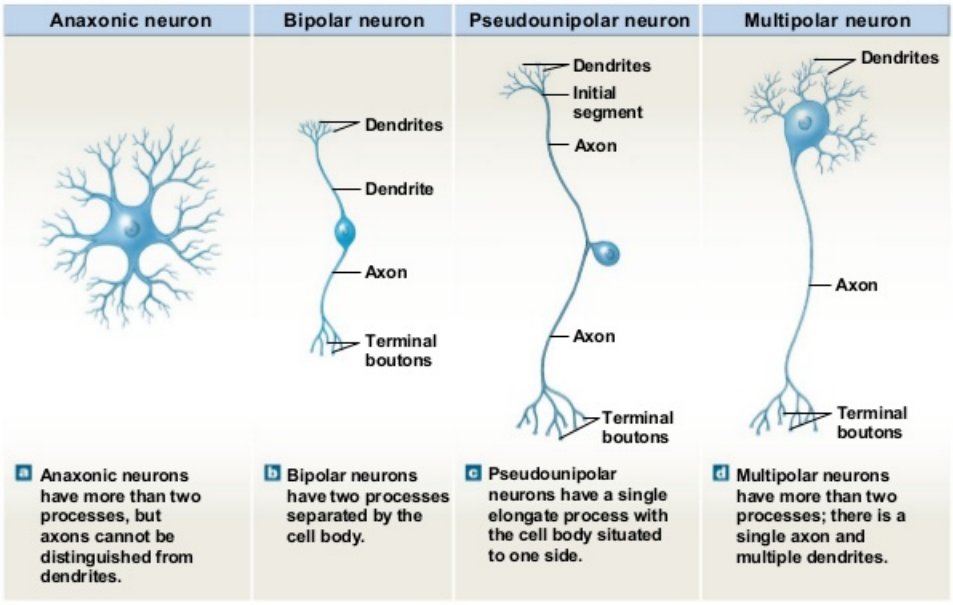

Figure 1.6: Structural categories of neurons [48].

skeletal muscles, sensory organs (eyes, ears, mouth, and nose). They also carry autonomic nervous system signals from the visceral organs (heart, lungs, vessels, etc).

In comparison, **motor neurons** (efferent neurons; lower motor neurons) are multipolar shaped cells that conduct action potentials out of the central nervous system. Their cell bodies and dendrites are located in the central nervous system and their axons run inside the nerves to the peripheral organs.

Interneurons (internuncial or association neurons) are the billions of cells that form much of the central nervous system and link the sensory and motor neurons. After receiving input from the sensory neurons, the interneurons perform many complex tasks inside the CNS. First, they integrate, image, and interpret, the sensory information. Next, they form judgments and make needed decisions. Finally, they plan and initiate appropriate response behaviors, which they transfer to the motor neurons.

1.2.3 Electrical Activity of Neurons

The nervous signal delivered by the neuron is of an electrical nature. This property is an exclusivity of the plasma membrane of the nerve tissue which is very permeable to certain ions. The flow of ions through this membrane is therefore at the origin of a membrane current that reflects the electrical activity of neurons. The ionic unbalance between the intra- and extracellular media of the membrane promotes the electrical activity of the

neurons. Therefore, it is important to understand both anatomy and physiology of the cell membrane.

1.2.3.1 The cell membrane

The neuronal membrane serves as a barrier to enclose the cytoplasm inside the neuron, and to exclude certain substances that float in the fluid that bathes the neuron. The membrane with its mosaic of proteins is responsible for many important functions:

- keeping certain ions and small molecules out of the cell and letting others in,
- accumulating nutrients, and rejecting harmful substances,
- catalyzing enzymatic reactions,
- establishing an electrical potential inside the cell,
- conducting an impulse being sensitive to particular neurotransmitters and modulators .

The membrane is made of lipids and proteins-fats and chains of aminoacids. The basic structure of this membrane is a bilayer or sandwich of phospholipids, organized in such a way that the polar (charged) regions face outward and the non polar regions face inward. The external face of the membrane contains the receptors, small specialized molecular regions which provide a kind of "attachment port" for other external molecules, in a scheme analogous to a key and a keyhole. For each external molecule there is a corresponding receptor. Whenever receptors become attached to a molecule, some alterations of the membrane and in the interior of the cell ensue, such as the modification of permeability to some ions. The main ions found on both sides of the membrane are Na^+ (sodium) ions, K^+ (potassium) ions and Cl^- (chlorite) ions. The schematic view of neuron cell membrane is drawn in Fig.1.11. At rest, the cell membrane is the seat of a resting potential.

1.2.3.2 The resting Potential

The relatively static membrane potential of quiescent cells is called the resting membrane potential (or resting voltage). Generally the value of resting potential is about $-70mV$. This value measured using a microelectrode artifice (see Fig.1.11), corresponds to the difference in electrical state between the intracellular medium on the one hand and the extracellular medium on the other hand. Negative value of resting potential is due to:

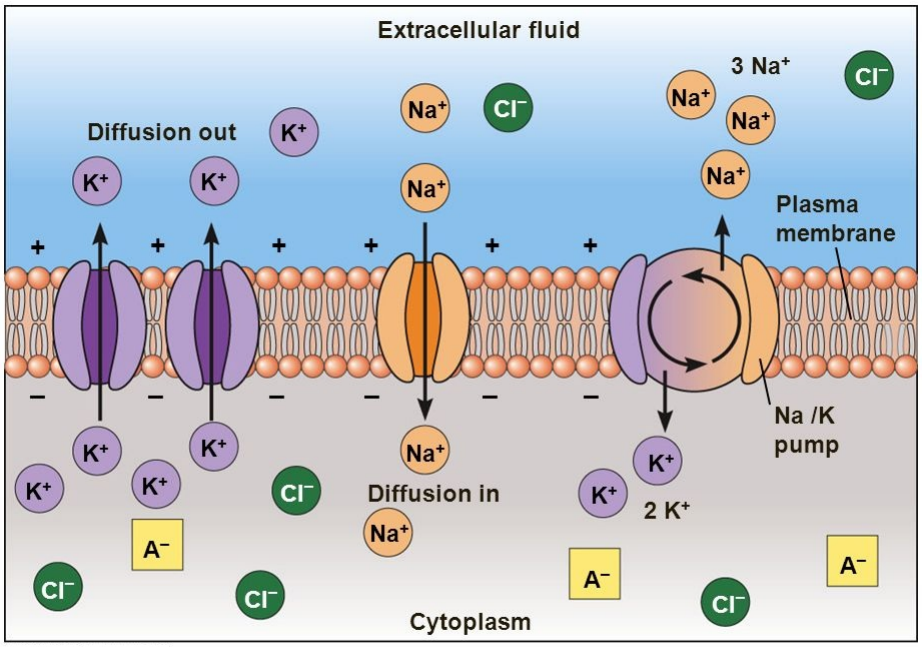

Figure 1.7: Cell membrane flow diagram [49].

- presence of large number of positive Na^+ ions towards outside of membrane,
- presence of large number of positive K^+ ions towards inside of membrane,
- zwitterionic protein molecules of cytoplasm behave as negative ions in presence of highly charged K^+,
- $Na^+ - K^+$ ion pump continuously pumps out three sodium ions while only two potassium ions are taken inside the cell.

All these factors mean that the inside of the cell is negatively charged with respect to the outside, hence the existence of a resting potential. However, when cell membrane is excited, the resting potential splits into action potential.

1.2.3.3 The action Potential

The action potential is a localized, short-lived electrical signal emitted by excitable cells (eg, neuron) when subjected to suitable stimuli. In fact, the stimulus intensity must reach a certain threshold value in order to generate this signal. As depicted in Fig.1.9, the action potential displays four transient phases ranging from:

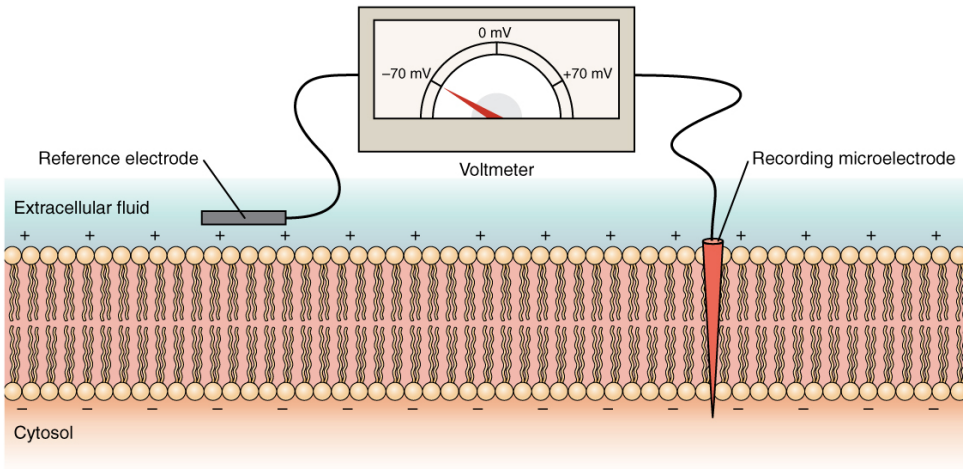

Figure 1.8: Measuring charge across a Membrane with a voltmeter. A recording electrode is inserted into the cell and a reference electrode is outside the cell. By comparing the charge measured by these two electrodes, the transmembrane voltage is determined. It is conventional to express that value for the cytosol relative to the outside [49].

- **failure phase** where the action potential is between $-70mV$ and $-55mV$. The limit value $-55mV$ represents the threshold value that the action potential must reach in order for it to appear. Thus, the action potential obeys to the threshold law. During this phase, the sodium channels open gradually causing the entry of sodium ions inside the cell, but their concentration remains low. At the same time, the potassium channels are inactive and therefore remain closed,

- **depolarization phase** where the action potential increases from $-55mV$ to $+30mV$, reaches its peak before starting to decrease. It is important to note that this maximum value can not be exceeded whatever the greatest possible value that can reach the intensity of the stimulus. As a result, the action potential responds to the all-or-nothing law. During this phase, all sodium channels are opened and the potassium channels closed but active. A large amount of sodium ions invade the intracellular fluid thus creating a reverse polarity of the membrane. Thus, unlike the resting state, the inside of the membrane becomes positively charged, while the outside becomes negatively charged. At the end of this phase, the sodium channels close, becoming inactive, as the potassium canals open.

- **repolarization phase** occurs when action potential decreases from its maximum value $+30mV$ to their resting state $-70mV$. Throughout this stage, more and more

K^+ ions flow towards outside of membrane, thus leading to the initial polarization state where more positive charges are on the outside and more negative charges on the inside.

- **hyperpolarization phase** occurs when action potential falls below the resting potential value. This is due to the slow closing of the potassium channels and results in a recrudescence of potassium ions outside the cell. As these canals close, the sodium pump will initiate the slow entry of sodium ions into the cell thus allowing the action potential to recover its resting value. At the end of this transition, the sodium channels become active, that is to say close to respond to a new stimulus.

It should also be noted that the time interval separating the onset of depolarization and the end of repolarization constitutes the refractory period during which the cell membrane can not respond to a new stimulus whatever its intensity. Moreover, since action potential is generated locally in the neuron, it becomes like a stimulus and will regenerate along the axon to the synaptic connections. It is said that the action potential undergoes a conduction that is saltatory in the case of myelinated axons and continues in the case of unmyelinated ones. In summary, the action potential obeys to four main laws that govern its properties namely:

- **the threshold law**: the action potential emerges only when the membrane potential reached a certain threshold level which is proportional to the stimulus intensity [51].

- **the all-or-nothing law**: The amplitude of an action potential is independent of the amount of current that produced it. In other words, larger currents do not create larger action potentials. Therefore, action potentials are said to be all-or-none signals, since either they occur fully or they do not occur at all [52]. The frequency of action potentials is correlated with the intensity of a stimulus. This is in contrast to receptor potentials, whose amplitudes are dependent on the intensity of a stimulus [51].

- **the refractory period law**: each action potential is followed by a refractory period, which can be divided into an absolute refractory period, during which it is impossible to evoke another action potential, and then a relative refractory period, during which stronger than usual stimulus is required [51]. These two refractory periods are caused by changes in the state of sodium and potassium channel molecules. When closing

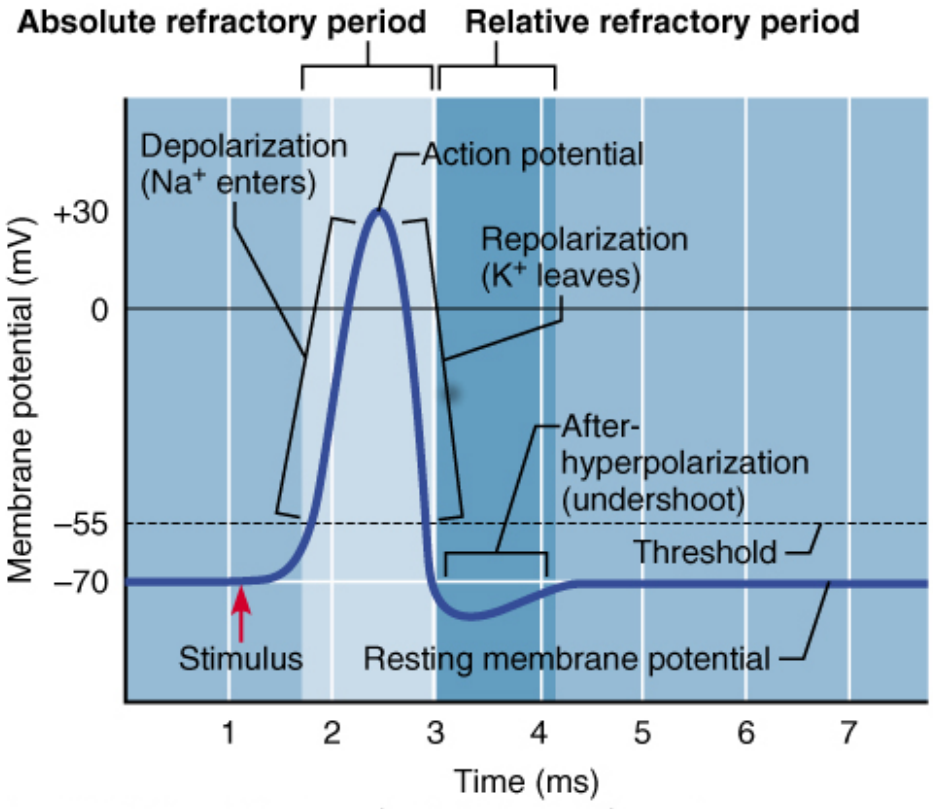

Figure 1.9: Action potential graph [50].

after an action potential, sodium channels enter an "inactivated" state, in which they cannot be made to open regardless of the membrane potential. This gives rise to the absolute refractory period. Even after a sufficient number of sodium channels have transitioned back to their resting state, it frequently happens that a fraction of potassium channels remains open, making it difficult for the membrane potential to depolarize, and thereby giving rise to the relative refractory period. Because the density and subtypes of potassium channels may differ greatly between different types of neurons, the duration of the relative refractory period is highly variable. The absolute refractory period is largely responsible for the unidirectional propagation of action potentials along axons [51]. At any given moment, the patch of axon behind the actively spiking part is refractory, but the patch in front, not having been activated recently, is capable of being stimulated by the depolarization from the action potential.

- **the law of conduction**: the action potential generated at the axon hillock propa-

gates as a wave along the axon without turning back because of the refractory period law. The currents flowing inwards at a point on the axon during an action potential spread out along the axon, and depolarize the adjacent sections of its membrane. If sufficiently strong, this depolarization provokes a similar action potential at the neighboring membrane patches. This basic mechanism was demonstrated by Alan Lloyd Hodgkin in 1937 [53].

1.2.3.4 The Nerve Impulse

It is important to distinguish the concepts of action potential on the one hand, and the nerve impulse on the other hand. In fact, the action potential is an electrochemical signal that results from the depolarization phenomenon of the plasma membrane of neuron, while nerve impulse is the phenomenon of propagation of an action potential along the nerve fiber. The nerve pulse propagates through the nerve fiber without decay and with constant velocity. An impulse can be formed and spread because the nerve fiber contains a nonlinear element, which suppresses small deviations from normal state and strengthens big ones. In this case, the nonlinear dependence of the membrane permeability (through which the nerve impulse is spread) from the momentum and the diffusion of ions across the membrane are balanced. In Ref. [54], it is shown that non-linearity can actually balance diffusion and, as a result, a running solitary wave with constant speed and shape can occur, i.e., a soliton. A nerve impulse is then an extension of an action potential. Physiological studies have shown that propagation of a nerve impulse through NNs has autowave character. This also allows simulating such processes using soliton theory which describes the form and velocity of propagation of the nervous pulse, stability of its characteristic parameters in time, and process locality with very good precision [55]. The conduction of an action potential along the axon can be continuous or saltatory. In saltatory conduction, an action potential at one node of Ranvier causes inwards currents that depolarize the membrane at the next node, provoking a new action potential there; the action potential appears to "hop" from node to node. This propagation mode enable fast and efficient transduction of electrical signals in the nervous system for certain neuronal axons that are covered with myelin sheaths. However, in the absence of the myelin sheath, the conduction of the nerve impulse proceeds continuously, thus reducing its propagation speed. As a general rule, myelination increases the conduction velocity of action potentials and makes them more energy-efficient. Whether saltatory or continue, the mean conduction velocity of an

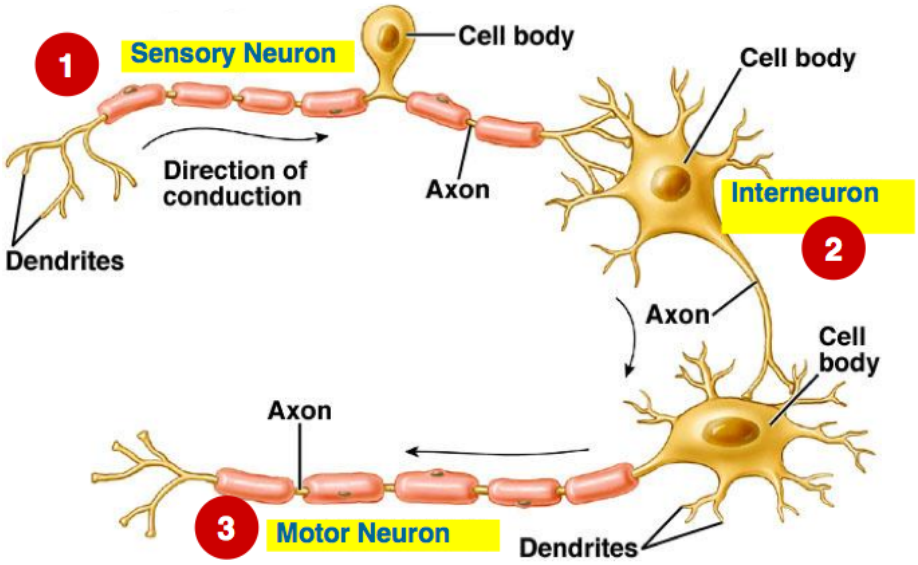

Figure 1.10: A neural network with three neurons [57]

action potential ranges from 1 metre per second (ms^{-1}) to over $100ms^{-1}$, and, in general, increases with axonal diameter [56]. In practice, the nerve impulse emitted by a neuron does not remain confined in the latter, it is transmitted to the neighboring neuron via synaptic connections. The recipient neuron in turn transmits it to its nearest neighbor by the same process, and so on until its final destination, which is either the brain or a motor organ. Thus, the path taken by the nerve impulse from its source to its destination constitutes the neural network.

1.3 The Neural Networks

A network of biological neurons is a series of neurons interconnected by synapses whose activation defines a recognizable linear pathway capable of communicating with each other by sharing nerve impulses. Therefore, the synapse appears as the main characteristic entity of such a network. Fig.1.10 is an illustration of a simple neural network.

1.3.1 The Synapses

Synapses are the junctions formed with other nerve cells where the presynaptic terminal of one cell comes into 'contact' with the postsynaptic membrane of another. It is at

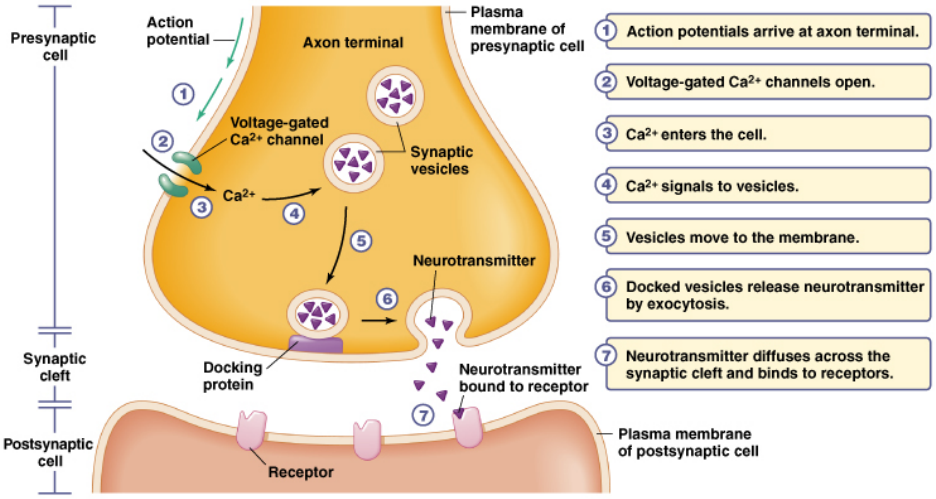

Figure 1.11: Chemical synapse diagram [61].

these junctions that neurons are excited, inhibited, or modulated. Briefly, the synapse is the system which allows the neurons to communicate between them, it is the place where information passes from a neuron to another. Structurally, we distinguish two types of synapses, electrical and chemical. However, from a functional point of view, there are excitatory, inhibitory and modulatory synapses.

1.3.1.1 Chemical Synapses

In general in chemical synapses (Fig.1.11), action potentials that reach the synaptic knobs cause a neurotransmitter to be released into the synaptic cleft [58]. Neurotransmitters are small molecules that may open ion channels in the postsynaptic cell; most axons have the same neurotransmitter at all of their termini. The arrival of the action potential opens voltage-sensitive calcium channels in the presynaptic membrane; the influx of calcium causes vesicles filled with neurotransmitter to migrate to the cell's surface and release their contents into the synaptic cleft [59]. This complex process is inhibited by the neurotoxins tetanospasmin and botulinum toxin, which are responsible for tetanus and botulism, respectively [60]. There are two types of chemical junctions. Type I is an excitatory synapse, generally found on dendrites, type II is an inhibitory synapse, generally found on cell bodies. Different substances are released at these two types of synapse. The direction of flow of information is usually one way at these junctions.

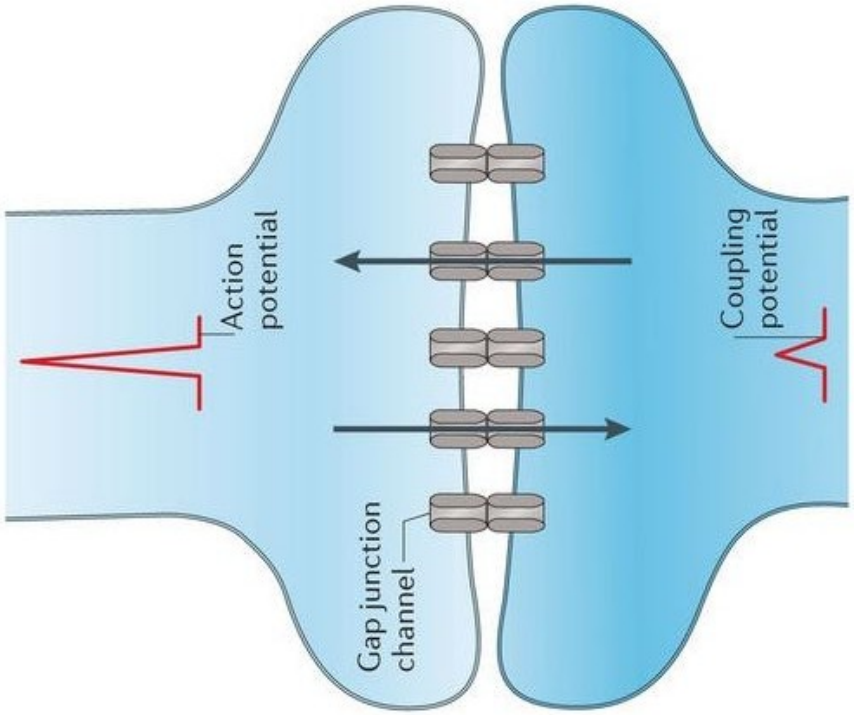

Figure 1.12: Electrical synapse flow diagram [62].

1.3.1.2 Electrical Synapses

Electrical synapses (Fig.1.12) dispense with the "middleman" of the neurotransmitter, and connect the presynaptic and postsynaptic cells together [63]. When an action potential reaches such a synapse, the ionic currents flowing into the presynaptic cell can cross the barrier of the two cell membranes and enter the postsynaptic cell through pores known as connexion [64]. Thus, the ionic currents of the presynaptic action potential can directly stimulate the postsynaptic cell. Electrical synapses allow for faster transmission because they do not require the slow diffusion of neurotransmitters across the synaptic cleft. Hence, electrical synapses are used whenever fast response and coordination of timing are crucial, as in escape reflexes, the retina of vertebrates, and the heart. Additionally, ions can generally flow both ways at these junctions i.e. they tend to be bi-directional, although there are electrical junctions where the ions can only flow one way, and hence are known as rectifying junctions. Rectifying junctions are used to synchronize the firing of nerve cells.

In short, the comparative table between electrical and chemical synapses is presented below

Electrical synapses	**Chemical synapses**
Cytoplasmic continuity between pre-and post-synaptic cells	No cytoplasmic continuity between pre-and post-synaptic cells
Communicating agent is ionic current	Communicating agent is a chemical transmiter
Essentially no synaptic delay	Significant synaptic delay
Typically bidirectional	Unidirectional
Rare in complex animals	Common in complex animals
Common in simple animals	Rare in simple animals
Direct communication among neurons	Indirect communication among neurons
Post synaptic signal is similar to presynaptic	Post synaptic signal can be different
Only excitatory	Excitatory or inhibitory
synchronized activity	specificity: point to point communication
temperature-insensitive	temperature-sensitive

Table 1.1: Comparative table between electrical and chemical synapses.

1.3.1.3 Excitatory Synapses

Most excitatory synapses in the brain use glutamate or aspartate as the neurotransmitter. These neurotransmitters bind to non-selective cationic channels that allow for Na^+ and K^+ to pass. As mentioned earlier, it takes many excitatory post synaptic potentials (EPSPs) from these kinds of synapses to depolarize a postsynaptic neuron enough to reach threshold and trigger an action potential. A very important subset of synapses in the brain includes a group capable of forming memories by increasing the activity and the strength of the synapse. This process is called long-term potentiation. Long-term potentiation operates at the synapse, using the neurotransmitter glutamate and the receptor known as the N-methyl-D-aspartic acid (NMDA) receptor. The NMDA receptor is unique in that it is both ligand and voltage regulated. When activated by ligands, it becomes permeable to Na^+, but if the charge difference is sufficient, the channel becomes permeable to Ca^{2+} as well. Ca^{2+} can initiate a second messenger cascade that results in an increase in the number of glutamate receptors, thereby increasing the strength of the synapse. The change in strength can last for weeks, months, or even years depending on

whether or not the synapse is continually used.

1.3.1.4 Inhibitory Synapses

It may seem somewhat of a paradox to have inhibitory synapses, but the excitability of neurons is essentially governed by a balance between excitation and inhibition. The main inhibitory neurotransmitters are G-Amino-Butyric Acid (GABA) and glycine. Both neurotransmitters bind to receptors that result in an increase conductance of Cl^- . Because of the negative charge of Cl^- and the fact that it usually moves into the cell, the effect is to oppose depolarization and cause the membrane to move away from threshold.

1.3.1.5 Modulatory synapses

Modulatory synapses are those that can be "primed" by neuromodulators so that they are able to respond more powerfully to other inputs. An example of a priming neuromodulator is norepinephrine. By itself, norepinephrine has little effect on synaptic transmission, but when a cell is exposed to norepinephrine first, it will react more powerfully to glutamate.

1.3.2 Functional and behavioral properties of neural networks

The human brain is a cluster of roughly 10^{15} neural networks. Although each of these networks may operate independently of each other, they perform almost the same functions as a whole and may adopt similar behaviors. If the neuron in its individuality is capable of generating, processing and transmitting information, its role remains limited to the microscopic scale. Its natural membership in a network allows it to modulate its activity while giving it still interesting and more promising properties. In general, NNs provide five major cognitive functions [65] namely:

- **Perception**: it is a sensory property that allows each individual to communicate with his external world through the five senses of sight, hearing, smell, touch and taste. Thus, the perception of an object for example is transmitted to the brain by a specialized neural network for this task, then the information received by the brain is analyzed and then decoded before being sent via another neural network to the receiving organ (the eye) in the form of a real image of the perceived object.

- **Thought**: it is a mental process that is triggered by internal stimuli. It consists of mental operations that the awake brain performs on internal information stored by a network of neurons. This property involves the networks of cortical neurons and allows the brain to imagine, perform mental or complex calculations and even move from one place to another.

- **Language**: it is a communicative property that uses neural networks. Language is one of the most elaborate, complex, and rich brain functions. Its pathological alterations are numerous and, at first sight, often bizarre. The cerebral cortex is a mosaic of specialized areas richly interconnected with each other. When an area is damaged, specific symptoms appear which quench the communication. Even more gravely, when two zones are disconnected, they develop disorders just as specific. Thanks to language, the wording of words becomes possible.

- **Consciousness**:, it is a discerning property of neural networks. It is thanks to it that we make good and bad choices. But it also makes it possible to distinguish sick subjects from healthy subjects. A loss of consciousness can lead to a comatic state surmountable but sometimes irreversible.

- **Memory**: it is one of the most fascinating properties of neural networks. Thanks to memory, enormous amounts of information are recorded during the learning process. It also allows you to remember people or images already seen before. There is long-term memory that can store information over a long period of time and short-term memory that temporarily stores information.

Some behavioral properties such as the rhythm in the alpha and gamma frequency range in the mammalian hypothalamus, NS, spiral and spindle waves formation, sleep oscillations and many others result from the dynamics of set of a neural network. Some of these behaviors are involved in the degradation of brain activity.

1.4 Mathematical Neuron Models

The functional complexity of the neuron, and more importantly, the great complexity of a neural network, require the use of new tools beyond simple physiological considerations to better understand the ability of neurons to mutually exchange information. One of the best tools in this regard is the development of mathematical models to accurately simulate

the dynamics of nerve impulses as well as the various biological phenomena that it may undergo during its propagation. The models in this category describe the relationship between neuronal membrane currents at the input stage, and membrane voltage at the output stage. The most extensive experimental inquiry in this category of models was made by Hodgkin-Huxley in the early 1950's using an experimental setup that punctured the cell membrane and allowed to force a specific membrane voltage/current.

1.4.1 Hodgkin-Huxley Model

The HH model is one of the most important models in computational neuroscience built on the basis of logical physiological assumptions. In biophysically based neural modeling, the electrical properties of a neuron are represented in terms of an electrical equivalent circuit. Capacitors are used to model the charge storage capacity of the cell membrane, resistors are used to model the various types of ion channels embedded in membrane, and batteries are used to represent the electrochemical potentials established by differing intra-and extracellular ion concentrations. In Fig.1.13, we have drawn the HH electrical equivalent circuit. Based on the simple application of Kirchhoff's laws, Hodgkin and Huxley derived a model of four first-order ordinary differential equations described by:

$$C_m\dot{V}_m = \bar{G}_K n^4(E_K - V_m) + \bar{G}_{Na} m^3 h(E_{Na} - V_m) + \bar{G}_L(E_L - V_m) + I_{ext}, \tag{1.1a}$$

$$\dot{n} = \alpha_n(V_m)(1-n) - \beta_n(V_m)n, \tag{1.1b}$$

$$\dot{m} = \alpha_m(V_m)(1-n) - \beta_m(V_m)m, \tag{1.1c}$$

$$\dot{h} = \alpha_h(V_m)(1-h) - \beta_h(V_m)h, \tag{1.1d}$$

where (.) denotes the derivative with respect to time. I_{ext} is the current per unit area, and α_i and β_i are rate constants for the i^{th} ion channel, which depend on voltage but not time. $\bar{G}_n$ is the maximal value of the conductance. n, m, and h are dimensionless quantities between 0 and 1 that are associated with potassium channel activation, sodium channel activation, and sodium channel inactivation, respectively. C_m is the membrane capacitance per unit area, V_m denotes the membrane potential; E_K, E_{Na} and E_L are the potassium, sodium and leak reversal potentials, respectively. The time-dependent functions α_i and β_i are given by:

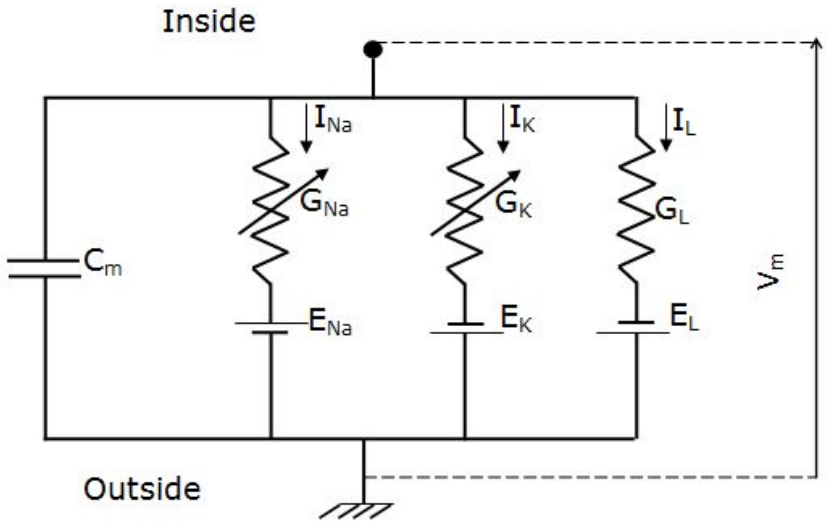

Figure 1.13: Electrical equivalent circuit for a short segment of squid giant axon according to [7]. The capacitor represents the capacitance of the cell membrane; the two variable resistors represent voltage-dependent Na^+ and K^+ conductances, the fixed resistor represents a voltage-independent leakage conductance and the three batteries represent reversal potentials for the corresponding conductances.

$$\alpha_n(V_m) = \frac{0.01(10 - V_m)}{\exp\left(\frac{10-V_m}{10}\right) - 1}, \quad \alpha_m(V_m) = \frac{0.1(25 - V_m)}{\exp\left(\frac{25-V_m}{10}\right) - 1}, \quad \alpha_h(V_m) = 0.07 \exp\left(-\frac{V_m}{20}\right),$$

$$\beta_n(V_m) = 0.125 \exp\left(-\frac{V_m}{80}\right), \quad \beta_m(V_m) = 4 \exp\left(-\frac{V_m}{18}\right), \quad \beta_h(V_m) = \frac{1}{\exp\left(\frac{30-V_m}{10}\right) + 1}.$$

The numerical values for the parameters of the HH model are given in the table 1.2. The HH model is known to exhibit only two main features namely tonic and chaotic spiking under the original values of parameters regime. But if the parameters are tuned, the HH model could exhibit other interesting neuro-computational properties including tonic, phasic and chaotic bursting, mixed mode, spike frequency adaptation, spike latency, subthreshold oscillations, rebound spike or burst just to cite a few. As we have already pointed out above, the HH model is one of the few neural models with a biological meaningful. Such models are important not only because their parameters are biophysically meaningful and measurable, but also because they allow to investigate questions related

Parameter	**Unit**	**Value**
C_m	$\mu F.cm^{-2}$	1.0
E_K	mV	$+12$
E_{Na}	mV	-115
E_L	mV	-10.63
$\bar{G}_K$	$mS.cm^{-2}$	36
$\bar{G}_{Na}$	$mS.cm^{-2}$	120
$\bar{G}_L$	$mS.cm^{-2}$	0.3

Table 1.2: HH model parameters [7].

to synaptic integration, dendritic cable filtering, effects of dendritic morphology, the interplay between ionic currents, and other issues related to single cell dynamics. But one of its disadvantages is that it has too many time-dependent parameters. Also the number of ordinary differential equations to integrate (in total four) makes its implementation very difficult. That is why Izhikevich said that one can use the HH formalism only to simulate a small number of neurons or when simulation time is not an issue.

1.4.2 Integrate and Fire Model

Because of its simplicity, the leaky IF model [8] is one of the most widely used models in computational neuroscience. It is only governed by one ordinary differential equation which describes the dynamics of membrane potential:

$$\dot{v} = a - bv + I, \quad if \quad v \geq v_{th}, \quad v \leftarrow c, \tag{1.2}$$

where v is the membrane potential, I is the input current, and a, b, c and v_{th} are the parameters. It is found that, when the membrane potential reaches the threshold value v_{th}, the neuron is said to fire a spike, and v is reset to c. The IF neuron is Class-1 excitable, i.e., the frequency of tonic spiking of neocortical regular spiking excitatory neurons depends on the strength of the input, and it may span the range from $2Hz$ to $200Hz$, or even greater; it can fire tonic spikes with constant frequency, and it is an integrator (IF neurons prefer high-frequency input; the higher the frequency the more likely they fire). Because of the lack of nonlinear terms in this model, it would be useless to explore it analytically.

1.4.3 FitzHugh-Nagumo Model

The FHN neuron model [5, 6] is the equivalent reduced HH model. To derive it, FitzHugh and Nagumo have used phase space methods (nonlinear mechanics). This model is a generic model of excitability and oscillatory dynamical behavior. This model is described by two ODEs given by:

$$\dot{x} = x(x-a)(1-x) - y + I, \tag{1.3a}$$

$$\dot{y} = \epsilon(x - \gamma y), \tag{1.3b}$$

where x represents the membrane potential, y is the slow ion current through the membrane and I stands for the input current. Model parameters are such that, $0 < a < 1$, $0 < \epsilon << 1$, $\gamma > 0$ and $1/\gamma - (1 - a + a^2)/3 > 0$, $(1 - a + a^2)/3 - \epsilon\gamma > 0$.

Indeed, Based on the seminal work by Hodgkin and Huxley combined to electrophysiological experiments, it is nowadays well accepted that information flow in neurons in the form of bioelectrical signals that have the form of impulses, originating from the potential difference across the cell membrane. The HH was refined to obtain the FHN model. The FHN model itself is a generalization of the Van der Pol (VDP) oscillator, whose modified version has been recently proposed with the assumption that the neural environment implies some periodic excitations. The importance given to the VDP model equation in recent years come from the fact that it describes self-excited or self-sustained oscillations, suitable to describe some important processes like those related to brain and cardiac waves [66]. This has been confirmed many years ago by some experimental data published by Brandt [67]. The FHN model is a generic model of excitability and oscillatory dynamical behavior in excitable media. It is confirmed that external stimuli can be effective to change the excitability and electrical activities of myocardial cells and neurons. Furthermore, it is argued [68, 69] that electrical and chemical autapses which are specific synapses connected to the body through closed loop, can modulate the electrical behaviors of neural and myocardial cells, and hence can regulate the collective behaviors in the network by inducing continuous pulses and wave fronts. Also, when reliable excitable models are set, with the modulation of astrocyte included [70], the collective behaviors such as synchronization and pattern selection can be carried out on the network of neurons under different topological connections. The electrical activities in neuron are also dependent on conductance of ions channels as channels blocking [71] can modulate the electrical modes of trans-membrane potential of neurons.

1.4.4 Hindmarsh-Rose Model

One of the most ubiquitous models explored by neuroscientists, the HR model [11] can be described by three ODEs written as:

$$\dot{x} = y - ax^3 + bx^2 - z + I, \tag{1.4a}$$

$$\dot{y} = c - dx^2 - ey, \tag{1.4b}$$

$$\dot{z} = r[s(x - x_e) - z], \tag{1.4c}$$

where dimensionless variables x, y and z are membrane potential, fast and slow current, respectively. I represents the excitation current, while parameters (a,b,c,d,e,r,s>0). x_e refers to the resting membrane potential which is generally negative and r is the ratio of fast/slow time scales. The original parameters values of this model are $a = 1.0$, $b = 3.0$, $c = 1.0$, $d = 5.0$, $e = 1.0$, $r = 0.006$, $s = 4.0$ and $x_e = -1.60$. In recall, HR model includes fast-variables known as x and y, then the slow variable indicated by z. Since y-variable is known to generate spike activity and z-variable to produce bursting-like activity, HR system exhibits a multi-time-scale spike-burst activity with more suitable values of input current I. The interplay between spiking and bursting regimes within this model allows it to reproduce a rich variety of membrane potential features of thalamic neurons classified from regular spiking/bursting, chaotic spiking/bursting or post-inhibitory rebound just to cite a few.

1.4.5 Izhikevich Model

Izhikevich's formalism [13, 14] is based on a model that reproduces the behavior of biological neurons. This model, described by a set of two first-order ordinary differential equations, is given by:

$$\dot{v} = 0.04v^2 + 5v + 140 - u + I, \tag{1.5a}$$

$$\dot{u} = a(bv - u), \tag{1.5b}$$

with the auxiliary after-spike resetting

$$if \;\; v \geq +30mV, \;\; then \;\; \begin{cases} v \leftarrow c \\ u \leftarrow u + d. \end{cases} \tag{1.6}$$

Here variable v represents the membrane potential of the neuron and u represents a membrane recovery variable, which accounts for the activation of K^+ ionic currents and inactivation of Na^+ ionic currents, and it provides negative feedback to v. The model can exhibit firing patterns of all known types of cortical neurons with the choice of parameters a, b, c and d given in Ref. [13].

1.4.6 Morris-Lecar Model

Morris and Lecar [9] suggested a simple 2-D model to describe oscillations in barnacle giant muscle fiber. It consists of a membrane potential equation with instantaneous activation of calcium ions current and an additional equation describing slower activation of current. The model reads:

$$C\dot{V} = g_L(V_L - V) + g_K n(V_K - V) + g_{Ca} m_\infty(V)(V_{Ca} - V) + I, \tag{1.7a}$$

$$\dot{n} = \lambda(V)(n_\infty(V) - n), \tag{1.7b}$$

where

$$\begin{aligned} m_\infty(V) &= \frac{1}{2}\left\{1 + \tanh\left[\frac{(V - V_1)}{V_2}\right]\right\}, \\ n_\infty(V) &= \frac{1}{2}\left\{1 + \tanh\left[\frac{(V - V_3)}{V_4}\right]\right\}, \\ \lambda(V) &= \bar{\lambda}\cosh\left[\frac{(V - V_3)}{2V_4}\right], \end{aligned} \tag{1.8}$$

with parameters: $C = 20\mu F.cm^{-2}$, $g_L = 2mS.cm^{-2}$, $V_L = -50mV$, $g_{Ca} = 4mS.cm^{-2}$, $V_{Ca} = 100mV$, $g_K = 8mS.cm^{-2}$, $V_K = -70mV$, $V_1 = 0$, $V_2 = 15mV$, $V_3 = 10mV$, $V_4 = 10mV$, $\bar{\lambda} = 0.1s^{-1}$, and applied current $I(\mu A.cm^{-2})$.

The model can exhibit various types of spiking, but could support tonic bursting only when an additional equation is added, e.g., slow inactivation of calcium ion current. In this case, the ML model becomes equivalent to the HH model since both have transient inward and persistent outward currents.

1.4.7 Comments on the various Models

Without being exhaustive, we have reviewed the most prominent neuronal models above. Some of them have biophysically meaningful and measurable parameters, notably HH and ML models. The others although not biophysically meaningful, exhibit the some

Models	biophysically meaningful	tonic spiking	phasic spiking	tonic bursting	phasic bursting	mixed mode	spike frequency adaptation	class 1 excitable	class 2 excitable	spike latency	subthreshold oscillations	resonator	integrator	rebound spike	rebound burst	threshold variability	bistability	DAP	accommodation	inhibition-induced spiking	inhibition-induced bursting	chaos	# of FLOPS
integrate-and-fire	-	+	-	-	-	-	-	+	-	-	-	-	+	-	-	-	-	-	-	-	-	-	5
integrate-and-fire with adapt.	-	+	-	-	-	-	+	+	-	-	-	-	+	-	-	-	-	+	-	-	-	-	10
integrate-and-fire-or-burst	-	+	+		+	-	+	+	-	-	-	-	+	+	+	-	+	+	-	-	-		13
resonate-and-fire	-	+	+	-	-	-	-	+	+	-	+	+	+	+	-	-	+	+	+	-	-	+	10
quadratic integrate-and-fire	-	+	-	-	-	-	-	+	-	+	-	-	+	-	-	+	+	-	-	-	-	-	7
Izhikevich (2003)	-	+	+	+	+	+	+	+	+	+	+	+	+	+	+	+	+	+	+	+	+	+	13
FitzHugh-Nagumo	-	+	+	-		-	-	+	-	+	+	+	-	+	-	+	+	-	+	+	-	-	72
Hindmarsh-Rose	-	+	+	+			+	+	+	+	+	+	+	+	+	+	+	+	+	+		+	120
Morris-Lecar	+	+	+	-		-	-	+	+	+	+	+	+	+		+	+	-	+	+	-	-	600
Wilson	-	+	+	+			+	+	+	+	+	+	+	+	+	+		+	+				180
Hodgkin-Huxley	+	+	+	+			+	+	+	+	+	+	+	+	+	+	+	+	+	+		+	1200

Table 1.3: Comparison of the neuro-computational properties of spiking and bursting models [14]; of FLOPS is an approximate number of floating point operations (addition, multiplication, etc.) needed to simulate the model during a $1ms$ time span. Each empty square indicates the property that the model should exhibit in principle (in theory) if the parameters are chosen appropriately, but the author failed to find the parameters within a reasonable period of time.

fundamental properties of thalamocortical spiking neurons, for this purpose we can mention FHN, HR, Izhikevich models. All other aspects of comparison between these models are contained in the table 1.3. Accordingly, HH, HR and Izhikevich models appear to be the three most powerful neuro-models that accurately reproduce a rich electrical activity of real neurons followed by ML and FHN ones. The IF model, although very simple to handle, remains one of the poorest models because it cannot exhibit even the most fundamental properties of cortical spiking neurons, and for this reason it should be avoided by all means.

Conclusion

This chapter has allowed us to understand the anatomy and physiology of biological neurons with the culminating point of interneuronal communication ensured by the synapses. It is through the synapses that a neuron is connected with its nearest neighbors to form a neural network in which information are shared. If chemical synapses are more abundant than electrical synapses, we must not forget the role played by the latter in the NS, a phenomenon known as the true source of many cerebral pathologies. Also, the most prominent computational models for reproducing the spikes and bursts-like patterns of the electrical activity of neurons have been studied from top to bottom. It appears that only the HH and ML models hold biologically acceptable properties, since the parameters of these two models have been deduced experimentally, unlike other models whose basic principle was to simulate the biological behavior of neurons observed experimentally. In this last category, we focused our attention on the HR model that does not fail this mission. This three-dimensional model accurately describes the biological mechanisms that accompany the generation, conduction, and transmission of nerve messages. Moreover, because of its nonlinear nature and its dynamics at multiple time scales characterized by emergence of spikes-bursts patterns known as the fundamental units of nervous message, the HR model can easily be explored both analytically and numerically and produce very interesting results to enrich the understanding of the functioning of the central nervous system. Therefore, in the rest of this work, we propose to study long-range, two-dimensional interneuronal communication and then analyze the phenomenon of neuronal synchronization by means of HR model.

Chapter 2

Improved models of FitzHugh-Nagumo and methodologies

Introduction

In the past years, mathematical and physical contributions devoted to neurological sciences have improved our understanding of pattern formation using the FHN mathematical model. Just to cite a few, simpler pulse solutions in the discrete FHN model have been constructed asymptotically [72–74]. Taking into account two different time constants, Panfilov and Hogeweg [75] modified the standard FHN model for excitable tissue and showed that a spiral wave can break up into an irregular spatial pattern. Dimitry *et al* [76] showed that particle-like behavior can lead to the formation of complex periodic and chaotic fractal-like spatiotemporal wave patterns in modified FHN network. Malevanets and Kapral [77] showed that fully developed labyrinthine pattern can be observed in a microscopic reaction model with a FHN mass action law. Very recently, Zhenga and Shena [78] showed that the FHN model has very rich dynamical behaviors, such as spotted, stripe and hexagon patterns. FHN model soliton solutions have been detected in different ways [79,80]. Daihai *et al* [81] using small-world connections in an inhomogeneous excitable medium obtained a well behaved pattern of spiral waves. It is confirmed that patterns like spiral waves and targeted waves and their breakdown show the complexity of brain and related to horrible disease in neuron system. Stripe, sported, and hexagon patterns are also revealed in a modified FHN model which are very similar to the case in reaction diffusion system. Different dynamical regimes are observed to be induced

by external noise. Stochastic resonance is reported to been enhanced in FHN model by colored noise [82].

One of the great challenges associated with the manipulation of developed mathematical models is the search for analytical solutions that give, in the long term, a clear view on the temporal or spatiotemporal dynamics of the studied systems. Therefore, given their complexity, these generic models are sometimes reduced to partial differential equations with soliton-like solutions using a well-known analytical methods such as the discrete multiple scale expansions [83–89] that lead to the discrete nonlinear Schrödinger (DNLS) equations; or the SDA [90–97] that lead whether in NLS equation or in the generalized Ginzburg-landau equation. These generally laborious methods require some skill on the part of the manipulator and provide more reliable results that are consistent with physical reality.

It is well-known that the FHN model can support solitary waves propagation as the best tool for nerve impulses transmission. These waves result from the interplay between nonlinearity and dispersion properties of the medium and are often highlighted by the MI phenomenon that has been extensively applied to a broad range of physical settings including nonlinear optics [98], hydrodynamics [99], nonlinear transmission lines (NLTLs) [91–93], biophysics [84, 85, 100], just to name a few.

The phenomenon of the MI studied through the linear stability analysis method unfortunately does not make it possible to make long-term predictions on the manifestations of the phenomenon. However, numerical methods such as the fourth-order Runge-Kutta integration method are generally exploited, not only to give a validity to the linear stability analysis, but also to reveal different patterns of the model. In this chapter, we will present the four important neuronal models that we have developed in the framework of this thesis with a particular focus on network morphology and the synaptic transmission known as the drive belt, or the bridge, which relays the nervous impulse from one neuron to an another. Also, we will apply the different analytical and numerical methods mentioned above in order not only to simplify them, but also to solve them.

2.1 Improved FHN models

2.1.1 The discrete FHN neural model under magnetic flow

It is well known that the standard FHN model is described by two variables $v(t)$ and $w(t)$ which represent the membrane potential and the recovery variables, respectively. Since the discovery of memristor, the fourth fundamental circuit element by Chua in 1971 [101], the effect of the electromagnetic flux has recently been introduced by Lv *et al.* [16] in the HR model. In the present work, we introduce the magnetic flux variable $\phi(t)$, which is used to describe the effect of electromagnetic induction. The equations for an improved FHN model for $N = 400$ identical neurons mutually coupled to their nearest neighbors through the gap junction is now made of three ordinary differential equations for the dimensionless variable $v(t)$, $w(t)$ and $\phi(t)$ as follows

$$\frac{dv_n}{dt} = K(v_{n+1} - 2v_n + v_{n-1}) + v_n(v_n - a)(2 - v_n) - w_n - k_1\rho(\phi_n)v_n + I_{ext}, \tag{2.1a}$$

$$\frac{dw_n}{dt} = \lambda(v_n - bw_n), \tag{2.1b}$$

$$\frac{d\phi_n}{dt} = v_n - k_2\phi_n + \phi_{ext}, \tag{2.1c}$$

with $i = 1, ...N$. The The parameter K is the coupling parameter between cells, while the parameter λrepresents the ratio of the time scales for $v_n(t)$and $w_n(t)$. The function $\rho(\phi_n) = \alpha + 3\beta\phi_n^2$ is the conductance developed from memristor and used for memory associated with magnetic field. According to the Faraday law of electromagnetic induction and description about memristor, the term $k_1\rho(\phi_n)v_n$ could be regarded as additive induction current on the membrane. ϕ_{ext} the external electromagnetic radiation which for simplicity is taken as a periodical function $\phi_{ext} = Acos(2\pi ft)$. The ion currents of sodium, potassium contribute the membrane potential and also the magnetic flux across the membrane; thus, a negative feedback term $-k_2\phi_n$ has been introduced in the third of Eqs. (2.1). I_{ext} represents the external forcing current. The parameter values used in this work are: $a = 0.3, b = 0.5, \lambda = 0.01, k_2 = 1, \alpha = 0.1$ and $\beta = 0.02$. The parameters K, k_1, I_{ext} and ϕ_{ext} will be selected so to display formation of complex patterns of the action potential.

The model of Eqs. (2.1) will be useful to evaluate the impact of internal magnetic induction and external electromagnetic radiation on the propagation of nerve impulses

in a network of electrically coupled neurons with nearest-neighbor interactions. For this purpose we will first reduce it to a DNLS equation using the multiple scale expansion and further we will integrate it numerically by the RK4 method in order to highlight some typical dynamical regimes under electromagnetic induction.

2.1.2 The discrete FHN myocardial model under magnetic flow

During the time period when electrical waves of excitations are emitted from the sinus node and spread among cardiac tissues, a time varying electromagnetic field is induced. The simple two variables FHN model proposed by Aliev and Panfilov [25, 26] does not include this important physical effect. The new model for myocardial excitations and electrical activities include the third variable $\phi_n(t)$, which is the magnetic flux parameter describing the physical effect of electromagnetic induction. The new three-variables dynamical equations for myocardial cell excitations and electrical activities are described as follows:

$$\frac{dv_n}{dt} = K(v_{n+1} - 2v_n + v_{n-1}) - kv_n(v_n - a)(v_n - 1.0) - v_n w_n + k_0\rho(\phi_n)v_n + I_{ext}, \quad (2.2a)$$

$$\frac{dw_n}{dt} = (\varepsilon + \frac{\mu_1 w_n}{v_n + \mu_2})[-w_n - kv_n(v_n - a - 1.0)], \quad (2.2b)$$

$$\frac{d\phi_n}{dt} = k_1 v_n - k_2\phi_n + \phi_{ext}. \quad (2.2c)$$

The system of equations above is a three species FHN equations, with $v_n(t)$ and $w_n(t)$ representing respectively, the fast variable trans-membrane potential and slow variable ions current. The first equation is finite difference discretized ordinary differential FHN equations with the cubic nonlinearity in $v_n(t)$, the second equation is a nonlinear ordinary differential equation in $w_n(t)$ and $v_n(t)$. The last one is a linear ordinary differential equation in $\phi_n(t)$. $-kv_n(v_n - a)(v_n - 1)$ is a nonlinear term representing the trans-membrane ionic currents per unit area. $\rho(\phi_n)$ is a nonlinear function representing the memdutance of memristor, used to describe the feedback of the time-varying electromagnetic field on the trans-membrane potential during electrical and ions concentration fluctuations in cells. It's given by $\rho(\phi_n) = \alpha + 3\beta\phi_n^2$. ϕ_n is the magnetic flux describing the effect of electromagnetic induction. $\phi_{ext} = H_0\cos(\Omega t)$ is a periodic forcing describing the influenced of electromagnetic radiation, where H_0 and Ω are the amplitude and angular frequency while $I_{ext} = I_0\sin(\omega t)$ is the mapped trans-membrane current from the external forcing current. We consider nearest neighbor interactions among myocardial cells in the network, where

cells only make electrical connections with their nearest neighbors. K represents the coupling strength of the gap junction. The parameter values used in this work are, a=0.15, k=8.0, μ_1=0.2, μ_2=0.3, k_1=0.2, k_2=1.0, ε=0.002, α=0.1, and β=0.2. The parameters K, k_0, I_{ext} and ϕ_{ext} will be selected so as to display the formation of complex patterns of the action potential.

The model realized will be useful to evaluate the impact of internal magnetic induction and external electromagnetic radiation on the propagation of waves in a myocardial network of electrically coupled cells with nearest-neighbor interactions. For this purpose we will first reduce it to a DNLS equation using the multiple scale expansion and further we will integrate it numerically by the RK4 method in order to highlight some typical dynamical regimes under electromagnetic induction and radiation.

2.1.3 The FHN neuronal network with memristive electromagnetic induction coupling

The FHN model is a generalization of the Bonhoeffer-Van der Pol oscillator. It suggests that an oscillating variable x, modulated by a damping function is modeled by the dynamical equation

$$\frac{\partial^2 x}{\partial t^2} + \frac{1}{a}(x^2 - 1)\frac{dx}{dt} + x = 0. \tag{2.3}$$

The term $\frac{1}{a}(x^2 - 1)$ represents the nonlinear damping function, dependent on the oscillating variable x while a is a positive constant. Eq. (2.3) can be broken down into two variables, first order differential equations(ODE) by introducing an auxiliary variable y, given by

$$\frac{dx}{dt} = \frac{1}{a}(x - \frac{x^3}{3} - y), \tag{2.4a}$$

$$\frac{dy}{dt} = ax. \tag{2.4b}$$

The above ODEs can be merged to obtain Eq. (2.3) by simply differentiating the first equation and substituting in the second equation. From the physical law of Maxwell Electromagnetic Induction(MEI), when the variable x is used as a membrane potential then the variable y can be thought as the magnetic flux variable($\dot{y} = ax$). The model is

then further improved to detect essence of electrical activity [102]. This enables Eq. (2.4) to be rewritten as

$$\frac{dx}{dt} = \frac{1}{a}(x - \frac{x^3}{3} - y + I_{ext}), \tag{2.5a}$$

$$\frac{dy}{dt} = ax - by + c, \tag{2.5b}$$

where x is the transmembrane potential and y, the traditional current variable now regarded as the magnetic flux from MEI theorem. I_{ext} is the external stimulus. Many researchers prefer to perform dynamical analyzes on reliable model rather than standard mathematical models to be consistent with biological experiments. During the fluctuation of inter-cellular and extra-cellular ion concentration in cells, time-varying electromagnetic field can be triggered [27]. The effect of electromagnetic induction should be considered during the dynamical analysis of the electrical behaviors of neuron and neuronal network. The memory effect of neuron can be described by using magnet flux on the Hindmarsh-Rose and other neuron models [29]. Magnetic flux is used to describe the effect of time-varying electromagnetic field, where the memristor is used to bridge the membrane potential and magnetic flux based on the consensus and consistency in physical units of variables in the neuron model. The induction current is then regarded as additive current on membrane.

Recent studies revealed that some neuronal networks with memristive synapse can portray abundant complex dynamics [45, 103, 104], significative of real brain dynamics. Inspired by these results, magnetic controlled gain in synaptic connection is proposed to model the synapse current using memristor coupling. This model detects essence of electrical activity and memory effect, holding more bifurcation parameters and can reproduce similar dynamical behaviors like the original FHN model. For simplicity in parameter manipulation and recognition, we let $\lambda = \frac{1}{a}$ and $y = \phi$. The dynamics of the chain network of n^{th}neurons is given by

$$\frac{dx_n}{dt} = \lambda(x_n - \phi_n - \frac{x_n^3}{3} + I_{ext}) + K\rho(\phi_n)(x_{n+1} - 2x_n + x_{n-1}), \tag{2.6a}$$

$$\frac{d\phi_n}{dt} = ax_n - b\phi_n + c + \phi_{ext}. \tag{2.6b}$$

The nonlinear term $K\rho(\phi_n)(x_{n+1}-2x_n+x_{n-1})$ is used to approach the synaptic current

associated with memristor. a calculates the effect of electromagnetic induction induced by the transport of ions in the cell, b represents the degree of polarization and magnetization, which may be regarded as the parameter adjusting the saturation of magnetic flux, c represents the threshold voltage. K is the feedback gain which bridges the coupling and modulation on gap junction membrane potential from magnetic field. K thus calculates memristive synaptic coupling strength. $\rho(\phi_n)$ calculates the memdutance of memristor, which is used to describe the modulation of time-varying electromagnetic field on the gap junction membrane. It's given by;

$$\rho(\phi_n) = \alpha + 3\beta\phi_n^2. \tag{2.7}$$

To be consistent with the previous work, we select the parameters as; $\alpha = 0.2, \beta = 0.2$ and $\phi_{ext} = A\cos(2\pi ft)$ selected as the external electromagnetic radiation of periodic type. A is the amplitude of the radiation while f is the frequency of the radiation. The rest of the parameters are set as; $a = 0.1, b = 0.8, c = 0.7, \lambda = 10$. The parameters K, I_{ext} and ϕ_{ext} will be selected so as to display formation of complex patterns of the action potential.

In what shall follows, we will use the discrete multiple-scaling expansion and show that the above system of coupled equations can be reduced to a single differential-difference equation, on which the linear stability analysis of MI will be performed. After discussing the possibility of modulated wave formation, full numerical simulations will be performed on the generic system (Eq. 2.6) to verify our analytical predictions. The effect of the memristive synaptic coupling parameter will be notably discussed with respect to pattern formation and synchronization.

2.1.4 The one dimensional diffusive FHN myocardial network under electromagnetic induction

Generally in NNs and particularly in FHN-NNs, the nerve or cardiac impulses can propagate in one dimension where the membrane potential will be given by $x_i(t)$ at the lattice point (i) reads:

$$\dot{v_i} = -\lambda v_i(v_i - a)(v_i - 1.0) - v_i w_i + I_{ext} + k_0\rho(\phi_i)v_i + D(v_{i+1} - 2v_i + v_{i-1}), \tag{2.8a}$$

$$\dot{w_i} = (\varepsilon + \frac{\mu_1 w_i}{v_i + \mu_2})[-w_i - \lambda v_i(v_i - a - 1.0)], \tag{2.8b}$$

$$\dot{\phi_i} = k_1 v_i - k_2\phi_i, \tag{2.8c}$$

with $1 \leq i \leq N$. Where N represents the node position in the network. v_i is the cardiac transmembrane potential, w_i is the slow variable for current, I_{ext} represents the mapped transmembrane current. D is the gap junction coupling between adjacent cells and $-\lambda v_i(v_i - a)(v_i - 1.0) - v_i w_i$ is the nonlinear representing the transmembrane ionic current per unit area. The rest parameter are carefully selected so as to reproduce the main properties of excitable medium. To be consistent with previous work on the model, we selected $a = 0.15, \mu_1 = 0.2, \mu_2 = 0.3, \lambda = 8.0$ and $\varepsilon = 0.002$.

During the rhythmic relaxation and shrinking of the heart so as to perform it's functional role of supplying blood to various organs of the body, complex electrophysiological activities have been detected in cardiac tissue. Indeed, during the fluctuation of concentration of ions in cells, a time-varying electromagnetic can be set up. This makes it important to consider the effect of electromagnetic induction according to Faraday's law of electromagnetic induction. In the above stated model, ϕ_i represents the magnetic flux variable used to describe the effect of this electromagnetic induction. As explained in Refs. [27, 29], the memristor is used to realize the modulation of the measured field on the transmembrane potential. The nonlinear $\rho(\phi_i)$ measures the memductance of memristor. The term $+k_0\rho(\phi_i)v_i$ is the positive induced current from electromagnetic induction. By expanding the nonlinear terms in Eq. (1), we have;

$$\dot{v}_i + \alpha_0 v_i = -\lambda v_i^3 + \alpha_1 v_i^2 - v_i w_i + \alpha_2 v_i \phi_i^2 + I_{ext} + D(v_{i+1} - 2v_i + v_{i-1}), \tag{2.9a}$$

$$\dot{w}_i + \varepsilon w_i = \beta_0 v_i + \beta_1 w_i^2 + \beta_2 v_i^2 + \beta_3 v_i w_i + \beta_4 v_i^2 w_i + \beta_5 v_i w_i^2, \tag{2.9b}$$

$$\dot{\phi}_i + k_2 \phi_i = k_1 v_i, \tag{2.9c}$$

where,

$$\begin{array}{lll} \alpha_0 = a\lambda - k_0\alpha & \beta_0 = (1+a)\varepsilon\lambda & \beta_3 = \lambda(1+a)\frac{\mu_1}{\mu_2} \\ \alpha_1 = \lambda(1+a) & \beta_1 = -\frac{\mu_1}{\mu_2} & \beta_4 = -\lambda(1+\frac{(1+a)}{\mu_2})\frac{\mu_1}{\mu_2} \\ \alpha_2 = 3\beta k_0 & \beta_2 = -\varepsilon\lambda & \beta_5 = \frac{\mu_1}{\mu_2^2}. \end{array}$$

Eqs. (2.9) can be transformed into a waveform by first differentiating Eq. (2.9a), which follows that:

$$\ddot{v}_i + \Omega_0^2 v_i + [\gamma_0 - 2\alpha_1 v_i + w_i - \alpha_2\phi_i^2 + 3\lambda v_i^2]\dot{v}_i + (\beta_0 - \varepsilon\alpha_1)v_i^2 + (\beta_2 + \varepsilon\lambda)v_i^3 + \alpha_2(2k_2 - \varepsilon)v_i\phi_i^2 - 2\alpha_2 k_1 v_i^2\phi_i + \beta_1 v_i w_i^2 + \beta_3 v_i^2 w_i + I_{ext} = D_0(v_{i+1} - 2v_i + v_{i-1}) + D_1(\dot{v}_{i+1} - 2\dot{v}_i + \dot{v}_{i-1}), \tag{2.10a}$$

$$\dot{w}_i + \varepsilon w_i = \beta_0 v_i + \beta_1 w_i^2 + \beta_2 v_i^2 + \beta_3 v_i w_i + \beta_4 v_i^2 w_i + \beta_5 v_i w_i^2, \tag{2.10b}$$

$$\dot{\phi}_i + k_2 \phi_i = k_1 v_i, \tag{2.10c}$$

with $\Omega_0^2 = \varepsilon\alpha_0$, $\gamma_0 = \varepsilon + \alpha_0$, $D_0 = \varepsilon D$ and $D_1 = D$. The above dynamical equations are similar to those generally used in modeling the dynamics of atomic chain. Nonlinear dynamical equations owing to their complexity, are typically not accessible to analytical approaches. It's only possible to obtain nearly exact solution through a special perturbation technique. In the process, we introduce the new variables;

$$\begin{aligned} v_i &= \epsilon\psi_i, \\ w_i &= \epsilon\varphi_i, \\ \phi_i &= \epsilon\sigma_i, \end{aligned} \tag{2.11}$$

with $\epsilon << 1$. It's important to remark that the variation of the membrane potential(ψ_i)is greater than that of the slow variable(φ_i). Since β_3 is the coefficient relating these two variables, the nonlinear term $\psi_i\varphi_i$ have then be perturbed to the order ϵ^2. As we are looking for exact solution in a weakly dissipative medium, $\gamma_0\dot{\psi}_i$ and $D_1(\dot{\psi}_{i+1} - 2\dot{\psi}_i + \dot{\psi}_{i-1})$ have also been perturbed to the order ϵ^2. We finally have the resulting system

$$\begin{aligned} \ddot{\psi}_i + \Omega_0^2\psi_i + \epsilon[\epsilon\gamma_0 - 2\alpha_1\psi_i + \epsilon\varphi_i - \epsilon\alpha_2\sigma_i^2 + 3\epsilon\lambda\psi_i^2]\dot{\psi}_i + \epsilon(\beta_0 - \varepsilon\alpha_1)\psi_i^2 + \\ \epsilon^2(\beta_2 + \varepsilon\lambda)\psi_i^3 + \epsilon^2\alpha_2(2k_2 - \varepsilon)\psi_i\sigma_i^2 - 2\epsilon^2\alpha_2 k_1\psi_i^2\sigma_i + \epsilon^2\beta_1\psi_i\varphi_i^2 + \epsilon^2\beta_3\psi_i^2\varphi_i = \\ D_0(\psi_{i+1} - 2\psi_i + \psi_{i-1}) + \epsilon^2 D_1(\dot{\psi}_{i+1} - 2\dot{\psi}_i + \dot{\psi}_{i-1}), \end{aligned} \tag{2.12}$$

$$\dot{\varphi}_i + \varepsilon\varphi_i = \beta_0\psi_i + \epsilon\beta_1\varphi_i^2 + \epsilon\beta_2\psi_i^2 + \epsilon^2\beta_3\psi_i\varphi_i + \epsilon^2\beta_4\psi_i^2\varphi_i + \epsilon^2\beta_5\psi_i\varphi_i^2, \tag{2.13}$$

$$\dot{\sigma}_i + k_2\sigma_i = k_1\psi_i. \tag{2.14}$$

The above system of equations are therefored those regulating the dynamics of the cardiac tissue under magnetic flow effect. The above equations show proofs of support of dispersive effect due to the presence of the term $D_0(\psi_{i+1} - 2\psi_i + \psi_{i-1})$. Dissipative effects brought about by the dissipative terms $\epsilon[\epsilon\gamma_0 - 2\alpha_1\psi_i + \epsilon\varphi_i - \epsilon\alpha_2\sigma_i^2 + 3\epsilon\lambda\psi_i^2]\dot{\psi}_i$ and $\epsilon^2 D_1(\dot{\psi}_{i+1} - 2\dot{\psi}_i + \dot{\psi}_{i-1})$. Nonlinear effects are supported by the rest of the nonlinear terms in the local kinetics of the above system of equations.

In what follows, the system of equations Eqs. (2.12)-(2.14) will be reduced into a CGL equation by applying the SDA, while the version Eqs. (2.8) will be numerically simulated using the RK4 method. Globally, the models will be used to show the existence of solitonic-like regimes in a one-dimensional FHN myocardial network.

2.2 Analytical and Numerical methods

2.2.1 The multiple scale expansion in the discrete approximation

Built by Leon and Manna [86], the multiple-scale allows to deduce simplified equations from a basic model without loosing its characteristic features. The method consists essentially in an asymptotic analysis of a perturbation series, based on the existence of different scales. More specifically, the method generates a hierarchy of (small) scales for the space and time variations of the envelopes of a fundamental (linear) plane wave and all the overtones. The scale is moreover directly related to the (small) amplitude of the wave itself. The multiple scale method is quite appropriate for the study of boundary value problems and leads to a DNLS equation (with reversed space-time), the goal being the study of a nonlinear dispersive chain with dispersion relation $\Omega(Q)$ where Ω represents the wave frequency and Q the wave number of the carried wave. The physical problem we are concerned with is the following: the first particle of the chain (say $n = 0$) is given an oscillation (or is submitted to an external force) at frequency Ω. Would the chain be linear that this oscillation would propagate without distorsion as the plane wave $\exp[i(\Omega t + Qnd)]$, with d being the lattice spacing. But the nonlinearity induces some deviations from the value Ω, namely, the wave propagates with actual frequency ω and wave number q that are defined as:

$$\omega = \Omega + \epsilon\lambda, \quad \text{and} \quad q = Q + \epsilon\frac{\lambda}{v_g} + \epsilon^2 c_g\lambda^2 + ... \tag{2.15}$$

where $v_g = \frac{\partial\Omega}{\partial Q}$ is the group velocity and $2c_g = \frac{\partial^2 Q}{\partial\Omega^2}$ represents the group velocity dispersion. λ is a small deviation from the natural frequency Ω.

The principle of this method can be summarized as follow: given a discrete differential equation in the form

$$F(\ddot{u}_n, \dot{u}_n(t), u_n(t), u_{n+1}(t), u_{n-1}(t), u_n^2(t), u_n^3(t), ..., u_n^r(t)) = 0. \tag{2.16}$$

One first seeks a solution of Eq. (2.16) in the form of a Fourier expansion in harmonics of the fundamental $A(n,t) = \exp[i(\Omega t + Qnd)]$, where the Fourier components are developed in a Taylor series in power of the small parameter ϵ measuring the amplitude of the initial wave, that is to say

$$u_n(t) = \sum_{p=1}^{\infty} \epsilon^p \sum_{l=-p}^{p} \psi_p^{(l)}(m,\tau) A^{(l)}(n,t). \tag{2.17}$$

Note that the above serie includes all overtones $A(n,t) = \exp[i(\Omega t + Qnd)]$ up to order p. These are generated by the nonlinear terms which explain that the corresponding coefficients are of maximum order ϵ^p. Here we have the real-valued-ness condition

$$\psi_p^{(-l)}(m,\tau) = \left(\psi_p^{(l)}(m,\tau)\right)^*, \tag{2.18}$$

with the asterisk denoting complex conjugations. The slow variables $\xi_n = m$ and $\tau_n = \tau$ are introduced via

$$\tau = \epsilon(t + \frac{nd}{v_g}), \quad m = \epsilon^2 n. \tag{2.19}$$

We then insert solution (2.17) into Eq.(2.16) to obtain a linear homogeneous system for $\psi_p^{(l)}(m,\tau)$ polynomial in $A^{(l)}(n,t)$. Finally we can proceed to collect and solve different orders of ϵ^p and harmonics l, order (p,l) in the obtained equation or system of equations. Note that it is enough to consider $l > 0$ as negative values follow from the reality condition (2.18). The culminating stage comes from order $(3,1)$ where the cubic DNLS equation is derived. In addition, the general formulas of this method are given as follows:

$$\begin{aligned} u_{n+1} - u_{n-1} = & \left[A^{(l)}(n+1,t) - A^{(l)}(n-1,t)\right]\psi_p^{(l)}(m,\tau) \\ & + \epsilon\left[A^{(l)}(n+1,t) + A^{(l)}(n-1,t)\right]\left(\frac{d}{v_g}\right)\frac{\partial}{\partial\tau}\psi_p^{(l)}(m,\tau) \\ & + \frac{\epsilon^2}{2}\left[A^{(l)}(n+1,t) + A^{(l)}(n-1,t)\right]\left[\psi_p^{(l)}(m+1,\tau) - \psi_p^{(l)}(m-1,\tau)\right] \\ & + \frac{\epsilon^2}{2}\left[A^{(l)}(n+1,t) - A^{(l)}(n-1,t)\right]\left(\frac{d}{v_g}\right)^2\frac{\partial^2}{\partial\tau^2}\psi_p^{(l)}(m,\tau) \end{aligned} \tag{2.20}$$

and

$$\begin{aligned} u_{n+1} - 2u_n + u_{n-1} = & \left[A^{(l)}(n+1,t) - 2A^{(l)}(n,t) + A^{(l)}(n-1,t)\right]\psi_p^{(l)}(m,\tau) \\ & + \epsilon\left[A^{(l)}(n+1,t) - A^{(l)}(n-1,t)\right]\left(\frac{d}{v_g}\right)\frac{\partial}{\partial\tau}\psi_p^{(l)}(m,\tau) \\ & + \frac{\epsilon^2}{2}\left[A^{(l)}(n+1,t) + A^{(l)}(n-1,t)\right]\left(\frac{d}{v_g}\right)^2\frac{\partial^2}{\partial\tau^2}\psi_p^{(l)}(m,\tau) \\ & + \frac{\epsilon^2}{2}\left[A^{(l)}(n+1,t) - A^{(l)}(n-1,t)\right]\left[\psi_p^{(l)}(m+1,\tau) - \psi_p^{(l)}(m-1,\tau)\right] \end{aligned} \tag{2.21}$$

2.2.1.1 Derivation of DNLS equation with coefficients depending on MF parameter

As a reminder, the system of Eqs. (2.1) has three equations with three unknowns, describing the FHN model under MF effect. The general solution of this equation can be considered in the form

$$U_n(t) = \sum_{p=1}^{\infty} \epsilon^p \sum_{l=-p}^{p} U_p^{(l)}(m,\tau) A^{(l)}(n,t), \tag{2.22}$$

with $A^{(l)}(n,t) = \exp[il(\Omega t + qn)]$ and the lattice spacing was taken equal to unit, and the state variables $U_n(t) = \{v_n(t), w_n(t), \phi_n(t)\}$ and $U_p^{(l)}(m,\tau) = \{\eta_p^{(l)}(m,\tau), \psi_p^{(l)}(m,\tau), \phi_p^{(l)}(m,\tau)\}$. By substitution of solution (2.22) into Eqs. (2.1), we obtain a linear homogeneous system for $\eta_p^{(l)}(m,\tau)$, $\psi_p^{(l)}(m,\tau)$ and $\phi_p^{(l)}(m,\tau)$ polynomial in $A^{(l)}(n,t)$ that will be solved at different orders of the small parameter ϵ, with the corresponding harmonics l. For the leading order (1,l), with $l = 0$, the solutions

$$\eta_1^0(m,\tau) = \psi_1^0(m,\tau) = \phi_1^0(m,\tau) = 0 \tag{2.23}$$

are found, while for $l = 1$ the dispersion relation

$$\Big[(i\Omega - 2K(\cos(q) - 1) + 2a + \alpha k_1)(i\Omega + \lambda b) + \lambda\Big](i\Omega + k_2) = 0 \tag{2.24}$$

should be satisfied for the system to admit non-trivial solutions in the form

$$\begin{aligned} \eta_1^1(m,\tau) &= \eta(m,\tau), \\ \psi_1^1(m,\tau) &= \frac{\lambda}{i\Omega + \lambda b}\eta(m,\tau), \\ \phi_1^1(m,\tau) &= \frac{\eta(m,\tau)}{(i\Omega + k_2)}. \end{aligned} \tag{2.25}$$

The order $(2,l)$, when $l = 0$, has the solutions

$$\begin{aligned} \eta_2^0(m,\tau) &= \frac{2b(2+a)}{1 + b(2a + \alpha k_1)}|\eta(m,\tau)|^2, \\ \psi_2^0(m,\tau) &= \frac{2(2+a)}{1 + b(2a + \alpha k_1)}|\eta(m,\tau)|^2, \\ \phi_2^0(m,\tau) &= \frac{2b(2+a)}{k_2(1 + b(2a + \alpha k_1))}|\eta(m,\tau)|^2. \end{aligned} \tag{2.26}$$

The case $l = 1$, with a zero determinant, should satisfy the Fredholm condition

$$V_g = \frac{2iK(i\Omega + \lambda b)^2}{(i\Omega + \lambda b)^2 - \lambda} \sin(q) \tag{2.27}$$

For the solution to be found in the form

$$\begin{aligned} \eta_2^1(m,\tau) &= \delta(m,\tau), \\ \psi_2^1(m,\tau) &= \frac{-\lambda}{(i\Omega + \lambda b)^2} \frac{\partial \eta(m,\tau)}{\partial \tau} + \frac{\lambda}{(i\Omega + \lambda b)} \delta(m,\tau), \\ \phi_2^1(m,\tau) &= \frac{-\lambda}{(i\Omega + k_2)^2} \frac{\partial \eta(m,\tau)}{\partial \tau} + \frac{1}{(i\Omega + k_2)} \delta(m,\tau), \end{aligned} \tag{2.28}$$

where $\delta(m,\tau)$ is an arbitrary function. At the same order, but for $l = 2$, solutions are derived in the form

$$\begin{aligned} \eta_2^2(m,\tau) &= \frac{(2+a)(2i\Omega + \lambda b)}{\Delta'} \eta^2(m,\tau), \\ \psi_2^2(m,\tau) &= \frac{\lambda}{(2i\Omega + \lambda b)} \eta^2(m,\tau), \\ \phi_2^2(m,\tau) &= \frac{1}{(2i\Omega + k_2)} \eta^2(m,\tau), \end{aligned} \tag{2.29}$$

where

$\Delta' = (2i\Omega - 2K(\cos 2q - 1) + 2a + \alpha k_1)(2i\Omega + \lambda b) + \lambda = 0.$

Finally, we solve the system for $\eta_3^1(m,\tau), \psi_3^1(m,\tau)$ and $\phi_3^1(m,\tau)$,which is obtained for $p = 3$ and $l = 1$, which yields, after making use of the previous solutions, the amplitude equation in η_m as follows:

$$iP(\eta_{m+1} - \eta_{m-1}) + Q \frac{\partial^2 \eta_m}{\partial \tau^2} + R|\eta_m|^2 \eta_m = 0, \tag{2.30}$$

where

$$\begin{aligned} P &= K \sin(q), \\ Q &= -\frac{\lambda}{(i\Omega + \lambda b)^3} - \frac{((i\Omega + \lambda b)^2 - \lambda)^2 \cos(q)}{4K(i\Omega + \lambda b)^4 \sin^2(q)}, \\ R &= \frac{4(2+a)^2(2i\Omega + \lambda b)}{\Delta'} - \frac{6\beta k_1}{(i\Omega + k_2)^2} \\ &\quad + \frac{4b(2+a)^2}{1 + b(2a + \alpha k_1)} - 3. \end{aligned} \tag{2.31}$$

The global form of Eq. (2.30) is now similar to the one obtained by Leon and Manna [87] in the case of electrical transmission lines. This equation will be used only for the

linear stability analysis, while the direct numerical experiments will be performed on the generic Eqs. (2.1).

2.2.1.2 Derivation of a DNLS equation with coefficients depending on the EMI gain

The four-variables model of the system of Eqs. (2.2) describes the dynamics of myocardial action potential under EMI and EMR. The general solution of such equations according to the multiple scale expansion reads:

$$\begin{aligned} v_n(t) &= \sum_{p=1}^{\infty} \epsilon^p \sum_{s=-p}^{p} \psi_p^s(\zeta_n, \tau_n) A^s(n,t), \\ w_n(t) &= \sum_{p=1}^{\infty} \epsilon^p \sum_{s=-p}^{p} \eta_p^s(\zeta_n, \tau_n) A^s(n,t), \\ \phi_n(t) &= \sum_{p=1}^{\infty} \epsilon^p \sum_{s=-p}^{p} \varphi_p^s(\zeta_n, \tau_n) A^s(n,t), \end{aligned} \tag{2.32}$$

with $A^{(s)}(n,t) = \exp[is(\Omega t + Qn)]$ and the lattice spacing was taken equal to one unit. By substitution of solution (2.32) into Eqs. (2.2), we obtain a linear homogeneous system for $\psi_p^{(s)}(m,\tau)$, $\eta_p^{(s)}(m,\tau)$ and $\varphi_p^{(s)}(m,\tau)$ polynomial in $A^{(s)}(n,t)$. At the leading order $(1,s)$, we obtain a homogeneous set of equations, where when $s=0$, gives:

$$\psi_1^0(m,\tau) = \eta_1^0(m,\tau) = \varphi_1^0(m,\tau) = 0. \tag{2.33}$$

Similarly, taking $s=1$ leads to a linear system whose determinant is null, yielding the dispersion relation:

$$\Big[i\omega - 2K(\cos(q)-1) + \alpha_0\Big](i\omega+\varepsilon)(i\omega+k_2) = 0. \tag{2.34}$$

According to the above dispersion relation given by Eq. (2.34), the non-trivial solutions ψ_1^1, η_1^1 and φ_1^1 of the resulting homogeneous set of equations can be looked out in the form:

$$\begin{aligned} \psi_1^1(m,\tau) &= \chi(m,\tau), \\ \eta_1^1(m,\tau) &= \frac{\varepsilon + i\omega}{\beta_0} \times \chi(m,\tau), \\ \varphi_1^1(m,\tau) &= \frac{k_1}{k_2 + i\omega} \times \chi(m,\tau), \end{aligned} \tag{2.35}$$

with $\chi(m,\tau)$ being an arbitrary function of m and τ. At the order $(2,s)$, when $s=0$, the solutions of the resulting system equations give

$$\begin{aligned}\psi_2^0(m,\tau) =&(\frac{2\alpha_1}{\alpha_0}-\frac{2\varepsilon}{\beta_0})\times \mid \chi(m,\tau)\mid^2,\\ \eta_2^0(m,\tau) =&[\frac{\beta_0}{\varepsilon}(\frac{2\alpha_1}{\alpha_0}-\frac{2\varepsilon}{\beta_0})+\frac{2\beta_1}{\varepsilon\beta_0^2}(\varepsilon^2-(i\omega)^2)\\ &+\frac{2\beta_2}{\varepsilon}]\times \mid \chi(m,\tau)\mid^2,\\ \varphi_2^0(m,\tau) =&\frac{k_1}{k_2}(\frac{2\alpha_1}{\alpha_0}-\frac{2\varepsilon}{\beta_0})\times \mid \chi(m,\tau)\mid^2 .\end{aligned} \tag{2.36}$$

With a zero determinant, the case $s=1$ should satisfy the Fredholm condition

$$V_g = 2iK\sin(q). \tag{2.37}$$

For the solution to be found in the form

$$\begin{aligned}\psi_2^1(m,\tau) &= \delta(m,\tau),\\ \eta_2^1(m,\tau) &= \frac{\beta_0}{(\varepsilon+i\omega)}\delta(m,\tau)-\frac{1}{\beta_0}\frac{\partial\chi(m,\tau)}{\partial\tau},\\ \varphi_2^1(m,\tau) &= \frac{k_1}{(k_2+i\omega)}\delta(m,\tau)-\frac{k_1}{(k_2+i\omega)^2}\frac{\partial\chi(m,\tau)}{\partial\tau},\end{aligned} \tag{2.38}$$

where $\delta(m,\tau)$ is taken to be an arbitrary function. At the same order, but for $s=2$, solutions are derived in the form

$$\begin{aligned}\psi_2^2(m,\tau) &= \frac{\alpha_1\beta_0-(\varepsilon+i\omega)}{\beta_0(2i\omega-2K(\cos(2q)-1)+\alpha_0)}\times\chi(m,\tau)^2,\\ \eta_2^2(m,\tau) &= \frac{1}{(\varepsilon+2i\omega)}[(\frac{\alpha_1\beta_0-(\varepsilon+i\omega)}{\beta_0(2i\omega-2K(\cos(2q)-1)+\alpha_0)})\\ &\quad+\frac{\beta_1}{\beta_0^2(\varepsilon+i\omega)^2}+\beta_2]\times\chi(m,\tau)^2,\\ \varphi_2^2(m,\tau) &= \frac{k_1[\alpha_1\beta_0-(\varepsilon+i\omega)]}{\beta_0(k_2+2i\omega)[(2i\omega-2K(\cos(2q)-1)+\alpha_0)]}\times\chi(m,\tau)^2.\end{aligned} \tag{2.39}$$

Finally, we solve the system for $\psi_3^1(m,\tau)$ and $\eta_3^1(m,\tau)$, obtained for $p=3$ and $s=1$, which yields, while making use of the previous solutions, the amplitude equation in $\chi(m,\tau)=\chi_m$ as:

$$iP(\chi_{m+1}-\chi_{m-1})+Q\frac{\partial^2\chi_m}{\partial\tau^2}+R|\chi_m|^2\chi_m=0, \tag{2.40}$$

with

$$\begin{aligned} R &= 2\alpha_1(\frac{2\alpha_1}{\alpha_0} - \frac{2\varepsilon}{\beta_0} + \theta_2) + \alpha_2 k_1^2[\frac{1}{(k_2+i\omega)^2} + \frac{2}{k_2^2-(i\omega)^2}] \\ &\quad + \frac{(\varepsilon+i\omega)}{\beta_0}(\frac{2\varepsilon}{\beta_0} - \frac{2\alpha_1}{\alpha_0}) - (3k+\theta_1+\theta_2+\theta_3), \\ Q &= \frac{-\cos(q)}{4K\sin^2(q)}, \\ P &= K\sin(q), \end{aligned} \tag{2.41}$$

where

$$\begin{aligned} \theta_1 =& \frac{1}{(\varepsilon+2i\omega)}[(\frac{\alpha_1\beta_0 - (\varepsilon+i\omega)}{\beta_0(2i\omega - 2K(\cos(2q)-1)+\alpha_0)}) \\ &+ \frac{\beta_1}{\beta_0^2(\varepsilon+i\omega)^2} + \beta_2], \\ \theta_2 =& \frac{\alpha_1\beta_0 - (\varepsilon+i\omega)}{\beta_0(2i\omega - 2K(\cos(2q)-1)+\alpha_0)}, \\ \theta_3 =& \frac{\beta_0}{\varepsilon}(\frac{2\alpha_1}{\alpha_0} - \frac{2\varepsilon}{\beta_0}) + \frac{2\beta_1}{\varepsilon\beta_0^2}(\varepsilon^2 - (i\omega)^2) + \frac{2\beta_2}{\varepsilon}. \end{aligned} \tag{2.42}$$

This equation is similar to one obtained in the previous section, but with neural networks.

2.2.1.3 Derivation of a DNLS equation with coefficients depending on the MSC parameter

The two-variable model of FHN equation Eqs. (2.6) detects essence of electrical activity and memory effect, holding more bifurcation parameters and can reproduce similar dynamical behaviors like the original FHN model but in which neurons are coupled through the memristive synaptic coupling created from EMI. The general solution of such equations according to the multiple scale expansion reads:

$$\begin{aligned} x_n(t) &= \sum_{p=1}^{\infty}\epsilon^p \sum_{l=-p}^{p}\eta_p^l(m,\tau)A^l(n,t), \\ \phi_n(t) &= \sum_{p=1}^{\infty}\epsilon^p \sum_{l=-p}^{p}\psi_p^l(m,\tau_n)A^l(n,t). \end{aligned} \tag{2.43}$$

Inserting the above expressions in the generic system of equations, we arrive at

$$\begin{aligned}\eta_1^0 =&\psi_1^0 = 0, \eta_1^1 = \Phi,\\ \psi_1^1 =&\frac{a}{(i\Omega + b)}\Phi, \eta_2^0 = \psi_2^0 = 0,\\ \eta_2^1 =&\delta, \psi_2^1 = \psi_1^1 - \frac{a}{(i\Omega + b)^2}\frac{\partial \Phi}{\partial \tau}, \eta_2^2 = \psi_2^2 = 0,\end{aligned} \tag{2.44}$$

where $\Phi = \Phi(m, \tau) = \Phi_m(\tau)$ and $\delta = \delta_m(\tau)$ are the new unknowns. The dispersion relation found, expressed as;

$$(i\Omega)^2 + U(i\Omega) + bU - b^2 + \lambda = 0, \tag{2.45}$$

where $U = 4K\alpha \sin^2 \frac{q}{2} - \lambda + b$. This allows the determination of the group velocity, following the Fredholm solvability condition given by;

$$V_g = \frac{\partial \Omega(q)}{\partial q} = \frac{2iK\alpha(i\Omega + b)^2 \sin(q)}{(i\Omega + b)^2 - \lambda}. \tag{2.46}$$

Solving then the system for ψ_3^1 and η_3^1, the unknown function $\delta = \delta_m(\tau)$ cancels out and the system eventually reduces to;

$$\frac{i}{2}(\Phi_{m+1} - \Phi_{m-1}) + Q\frac{\partial^2 \Phi_m}{\partial \tau^2} - R|\Phi_m|^2\Phi_m = 0, \tag{2.47}$$

with the coefficients, Q and R depending on the memristive synaptic coupling(K) and wave number(q) given by;

$$\begin{aligned}Q =& \frac{\cot(q)}{2V_g^2} + \frac{\lambda}{2\alpha K(i\Omega + b)^3 \sin(q)},\\ R =& \frac{12\beta \sin^2(\frac{q}{2})}{b^2 - (i\Omega)^2} + \frac{\lambda}{2\alpha K \sin(q)}.\end{aligned} \tag{2.48}$$

The continuous version of Eq. (47) is a well known model for boundary value problems in optical fibres. It has features of cubic Schrödinger equation and recently been reported in other biophysical settings such as in calcium and cardiac wave propagation [84, 138].

2.2.2 The semi-discrete approximation

The SDA is a perturbation technique in which the carrier waves are kept discrete while the amplitude is treated in the continuum limit. Applying this method allows one to study the modulation of a plane wave caused by nonlinear effects. Its principle is

almost identical to the full-discrete approximation, but the derived amplitude equations are either the NLS type or the generalized CGL. In practice, having a nonlinear differential equations as in Eqs. (2.12)-(2.14), one seeks solutions in the form:

$$u_n(t) = U(\xi,\tau)e^{i\theta_n} + U^*(\xi,\tau)e^{-i\theta_n} + \epsilon[V(\xi,\tau) + W(\xi,\tau)e^{2i\theta_n} + W^*(\xi,\tau)e^{-2i\theta_n}], \quad (2.49)$$

where the slow variables ξ and τ are related to fast ones n and t as

$$\xi = \epsilon(n - v_g t) \;\; and \;\; \tau = \epsilon^2 t \quad (2.50)$$

with $0 < \epsilon << 1$ and $\theta_n = kn - \omega t$. Note that index n denotes the cell number. Parameters k, v_g and ω, respectively stand for the wave number, group velocity and angular frequency and they are known to be related by the dispersion relation, or the solvability condition that determines the group velocity as

$$v_g = \frac{\partial \omega}{\partial k}. \quad (2.51)$$

Then such solution (2.49) is inserted into model of Eqs. (2.12)-(2.14) yield a linear homogeneous system for U, V and W polynomial in $e^{il\theta_n}$, $l = 0, 1, 2$ that will be solve later. In order to evaluate the diffusion term $u_{n+1}(t) - 2u_n(t) + u_{n-1}(t)$, it is worthy to treat amplitudes U, V and W like the continuum functions such that $U(\xi_{n\pm1},\tau)$, $V(\xi_{n\pm1},\tau)$ and $W(\xi_{n\pm1},\tau)$ are developed up to order ϵ^2 in Taylor series as

$$U(\xi_{n\pm1},\tau) = U(\xi,\tau) \pm \epsilon\frac{\partial U(\xi,\tau)}{\partial \xi} + \frac{\epsilon^2}{2}\frac{\partial^2 U(\xi,\tau)}{\partial \xi^2} + O(\epsilon^2). \quad (2.52)$$

Therefore, we obtain the following formula

$$\begin{aligned} u_{n+1} - 2u_n + u_{n-1} = &\left(2U\big(\cos(k) - 1\big) + 2i\epsilon\sin(k)\frac{\partial U}{\partial \xi} + \epsilon\cos(k)\frac{\partial^2 U}{\partial \xi^2}\right)e^{i\theta_n} \\ &+ \left(2\epsilon W\big(\cos(2k) - 1\big) + 2i\epsilon^2\sin(2k)\frac{\partial W}{\partial \xi}\right)e^{2i\theta_n} + c.c. + O(\epsilon^3). \end{aligned} \quad (2.53)$$

Furthermore the temporal derivative operators are given by

$$\begin{aligned} \frac{\partial}{\partial t} &= \left(\epsilon^2\frac{\partial}{\partial \tau} - \epsilon v_g\frac{\partial}{\partial \xi} - il\omega\right), \\ \frac{\partial^2}{\partial t^2} &= \left(\epsilon^2 v_g^2\frac{\partial^2}{\partial \xi^2} - 2il\omega\epsilon^2\frac{\partial}{\partial \tau} + 2il\omega\epsilon v_g\frac{\partial}{\partial \xi} - l^2\omega^2\right) + O(\epsilon^3). \end{aligned} \quad (2.54)$$

2.2.2.1 Derivation of damped CGL equations for myocardial cell WP.

Here, we will attempt to apply the technique of the SDA on the model of Eqs. (2.12)-(2.14) whose trial solutions are given by:

$$\psi_i = A(X,T)e^{i\theta} + \epsilon C(X,T) + \epsilon D(X,T)e^{2i\theta} + c.c + 0(\epsilon^2), \tag{2.55a}$$

$$\varphi_i = E(X,T)e^{i\theta} + \epsilon F(X,T) + \epsilon G(X,T)e^{2i\theta} + c.c + 0(\epsilon^2), \tag{2.55b}$$

,

$$\sigma_i = H(X,T)e^{i\theta} + \epsilon Q(X,T) + \epsilon P(X,T)e^{2i\theta} + c.c + 0(\epsilon^2), \tag{2.55c}$$

where the change of variables $X = \epsilon(n - v_g t)$ and $T = \epsilon^2 t$ has been applied, with v_g being the group velocity that will be defined later. We should however notice that according to the new variables, the direction n is the dominant one. In solutions (2.55), $\theta_n = kn - \omega t$ is the phase of the carrier wave and $c.c.$ represents the complex conjugate. Inserting the above trial solutions (2.55) into system of Eqs. (2.12)-(2.14), we obtained at the order $\epsilon^0 \times e^{i\theta}$, the dispersion relation

$$\omega^2 = \Omega_0^2 + 4D_0 \sin^2(\frac{q}{2}). \tag{2.56}$$

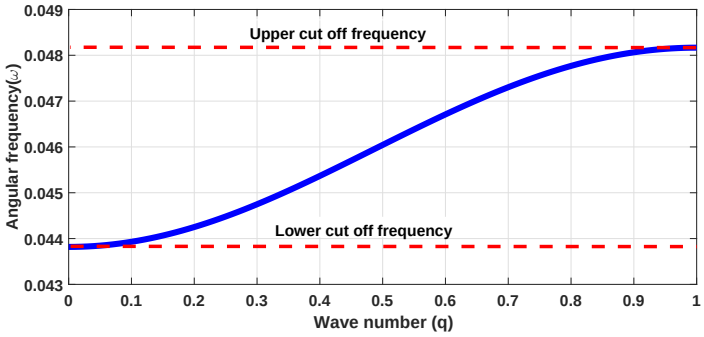

Figure 2.1: Panel displays the plot of angular frequency (ω), vs. the wave number (q), as given by the dispersion relation in Eq. (2.56), for $D_0 = 0.05$ and $k_0 = 1.2$

We plot the angular frequency(ω) versus the wave number(q) [Fig. (2.1)]. This plot is similar to that of the pass band filter, with corresponding lower and upper cutoff frequencies. The influence of feedback gain through the memristor coupling is clearly

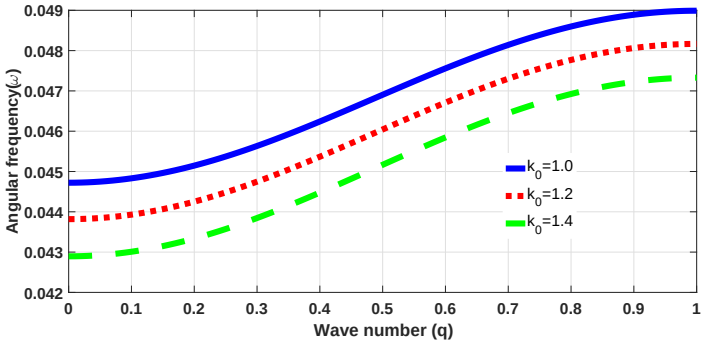

Figure 2.2: Panel shows how ω is a decreasing function of the memristor coupling parameter k_0. The lower and upper cut off frequencies are lowered as the effect of electromagnetic induction is increased thus more cells could be recruited into conduction process. The parameter values are the same as in Fig. (2.1)

depicted in Fig. (2.2) to be a decreasing function of the angular frequency. As the memristor coupling is increased, the lower cut off frequency is observed to be lowered.

The rest of the system equations give the following relations

$$\begin{aligned} E &= (a_1 + ia_2)A, \\ H &= (b_1 + ib_2)A \end{aligned} \tag{2.57}$$

with

$$\begin{aligned} a_1 &= \frac{\beta_0 \varepsilon}{\varepsilon^2 + \omega^2}, a_2 = \frac{\beta_0 \omega}{\varepsilon^2 + \omega^2}, \\ b_1 &= \frac{k_0 k_2}{k_2^2 + \omega^2}, b_2 = \frac{k_0 \omega}{k_2^2 + \omega^2}. \end{aligned} \tag{2.58}$$

At the order $\epsilon^1 \times e^{i\theta}$, we have the group velocity relation;

$$V_g = \frac{D_0 \sin(q)}{\omega}. \tag{2.59}$$

A plot of the group velocity relation is clearly revealed in Fig. (2.3) and the influence of feedback gain depicted in Fig. (2.4). The group velocity is an increasing function of the memristor coupling parameter.

As our first analytical prediction, it's confirmed that the effect of electromagnetic induction describing time-varying electromagnetic field set up in cardiac tissue during the fluctuation of ionic concentration has strong effect on the dynamical properties of electrical signals and wave propagation. Electromagnetic induction effect lowers the pass

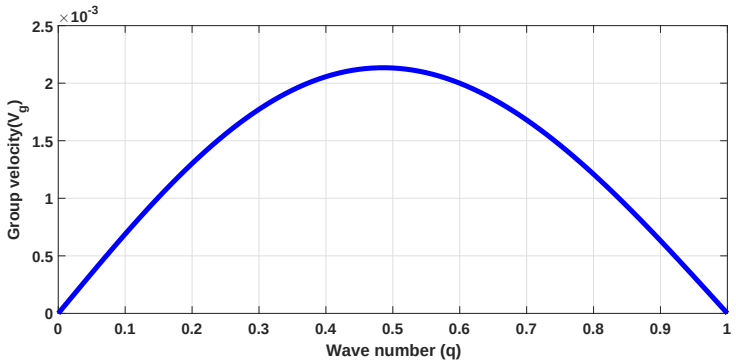

Figure 2.3: Panel displays the plot of group velocity (V_g) vs. the wave number (q), as given by the dispersion relation in Eq. (2.59), for $k_0 = 1.0$

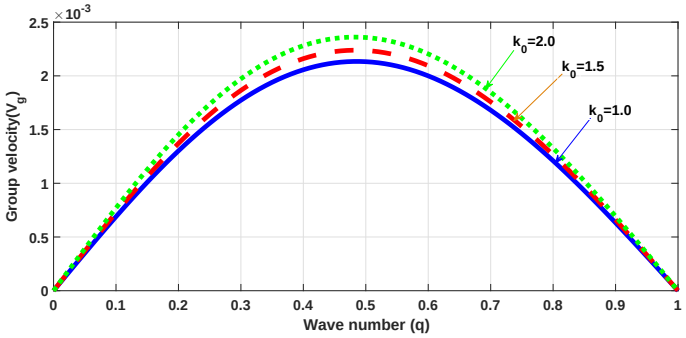

Figure 2.4: Group velocity is an increasing function of the memristor coupling.

band frequencies of signal,with the speed of the signals correspondingly enhanced by this effect. This is indicative that the feedback effect of magnetic flow can modulate the excitation behavior of cardiac tissue by changing the firing rate of cells.

At the order $\epsilon^1 \times e^{0i\theta}$ and $\epsilon^1 \times e^{2i\theta}$, we obtain some useful relations

$$\begin{aligned} C &= a_{11} \times |A|^2, \\ F &= a_{22} \times |A|^2, \\ Q &= a_{33} \times |A|^2, \end{aligned} \tag{2.60}$$

where,

$$\begin{aligned} a_{11} =& \frac{2(a_2\omega - \beta_0 + \varepsilon\alpha_1)}{\Omega_0^2}, \\ a_{22} =& \frac{2(a_2\omega - \beta_0 + \varepsilon\alpha_1) + 2\Omega_0^2(\beta_1 a_1^2 + \beta_1 a_2^2 + \beta_2)}{\varepsilon\Omega_0^2}, \\ a_{33} =& \frac{2k_1(a_2\omega - \beta_0 + \varepsilon\alpha_1)}{k_2\Omega_0^2}. \end{aligned} \tag{2.61}$$

At the order $\epsilon^1 \times e^{2i\theta}$, we obtained as well, the following relations

$$\begin{aligned} D =& (c_1 + ic_2) \times A^2, \\ G =& (d_1 + id_2) \times A^2, \\ P =& (e_1 + ie_2) \times A^2, \end{aligned} \tag{2.62}$$

where

$$c_1 = \frac{a_2\omega + \beta_0 - \varepsilon\alpha_1}{3\Omega_0^2 + 16sin^4(\frac{q}{2})}, c_2 = \frac{\omega(2\alpha_1 - a_1)}{3\Omega_0^2 + 16sin^4(\frac{q}{2})}, \tag{2.63}$$

$$\begin{aligned} d_1 =& \frac{\varepsilon\beta_0 c_1 + 2\beta_0 c_2\omega + \varepsilon\beta_1(a_1^2 - a_2^2) + 4\beta_1 a_1 a_2\omega}{\varepsilon^2 + 4\omega^2}, \\ d_2 =& \frac{\varepsilon\beta_0 c_2 - 2\beta_0 c_1\omega - 2\beta_2\omega - 2\beta_1\omega(a_1^2 - a_2^2) + 2\beta_1 a_1 a_2\varepsilon}{\varepsilon^2 + 4\omega^2}, \end{aligned} \tag{2.64}$$

$$e_1 = \frac{k_1(c_1 k_2 - 2c_2\omega)}{k_2^2 + 4\omega^2}, e_2 = \frac{k_1(c_2 k_2 + 2c_1\omega)}{k_2^2 + 4\omega^2}. \tag{2.65}$$

Finally at the order $\epsilon^2 \times e^{i\theta}$, while making use of the previous, we obtained the useful relation;

$$i\frac{\partial A}{\partial T} + \frac{P_r}{2}\frac{\partial^2 A}{\partial X^2} + (Q_r + iQ_i)|A|^2 A + i\frac{R_r}{2}A = 0. \tag{2.66}$$

Eq. (2.66) corresponds to the modified CGLE, with subscripts r and i representing the real and imaginary parts for real parameters given by

$$P_r = \frac{D_0\omega^2\cos(q) - D_0^2\sin^2(q)}{\omega^3}, \tag{2.67}$$

$$\begin{aligned} Q_r =& c_1a_2 + c_2(\alpha_1 - a_1) + \frac{1}{2}(d_2 - b_2\alpha_2) + \frac{1}{\omega}[3b_1k_1\alpha_2 - (\beta_0 - \alpha_1\varepsilon)(a_{11} + c_2)] \\ & - \frac{1}{2\omega}[3(a_1\beta_3 + \beta_2 + \varepsilon\lambda) + \beta_1(3a_1^2 + a_2^2) + \alpha_2(2k_2 - \varepsilon)(3b_1^2 + b_2^2)], \end{aligned} \tag{2.68}$$

$$\begin{aligned} Q_i =& \frac{3\lambda}{2} - \alpha_1(a_{11} + c_1) + \frac{1}{2}[\alpha_2(b_1 - 2b_1^2 - 2b_2^2) - (d_1 - a_{22} - 2a_1c_1 - 2a_2c_2)] + \frac{1}{\omega}[k_1k_2b_2 - c_2(\beta_0 - \varepsilon\alpha_1) \\ & - (2k_2 - \varepsilon)b_1b_2\alpha_2 - a_1a_2\beta_1] - \frac{a_2\beta_3}{2\omega}, \end{aligned} \tag{2.69}$$

$$R_r = \gamma_0 + 4D_1\sin^2(\frac{q}{2}). \tag{2.70}$$

The Complex Ginzburg-Landau Equation(CGLE) and many of its modified versions have drawn great attentions and subjected to wide investigations due to its merits in describing both at the qualitative and even quantitative levels, many physical and biophysical phenomena. In many domains of Physics, the one dimensional CGLE has been revealed to be the generic equation, describing dissipative phenomena above point of bifurcation [106]. We recall that dissipative systems driven far from equilibrium always supports soliton-like localized states. The modified CGLE plays an important in the description of broad spatiotemporal gap and optical solitons in optical wave guides [107]. CGLE plays vital roles in describing transition of Bose-Einstein condesnsation to liquid cystals and dynamics of insulin in glucose-blood system [89]. The CGLE has been proposed recently in the study of nonlinear neural impulses in a diffusive Hindmarsh Rose model [90]. In this work, one proposes to explore the existence of localized excitations in the FHN cardiac network with magnetic flow effect included.

The CGLE obtained in this context is very significant from biophysical point of view. Eq. (2.66) reveals that the modified Complex Ginzburg-Landau Equation describes the evolution of the modulated cardiac impulses in the cardiac tissue. Indeed, electrical signals and waves emitted from the sinus node propagates within the cardiac tissue using both space and time domains in order to regulate heart beat as powerful pacemaker. In another regards, the oscillation of myocardial cells at the sinus node generate a spatiotemporal dynamics of waves between cells as modified by the effect of electromagnetic induction set up during ions fluctuation inside and outside of the cell. Then, the spatiotemporal modulated waves in physiological environment travel not only across individual cells, but also from one myocardial cell to its neighbors. This proposition is related to a physiological

regard like calcium waves propagation between cells through intercellular waves capable of propagating across many cells.

In the CGLE [Eq. (2.66)], we remark that the dispersion and dissipation coefficients are real, while the nonlinearity coefficient is complex. This is indicative that the dynamics of modulated cardiac impulses in our model will always be described by the CGLE even when the dissipation coefficient is neglected. The variation of P_r, Q_r, Q_i, R_r and $P_r \times Q_r$ versus the wave number(q) are presented.

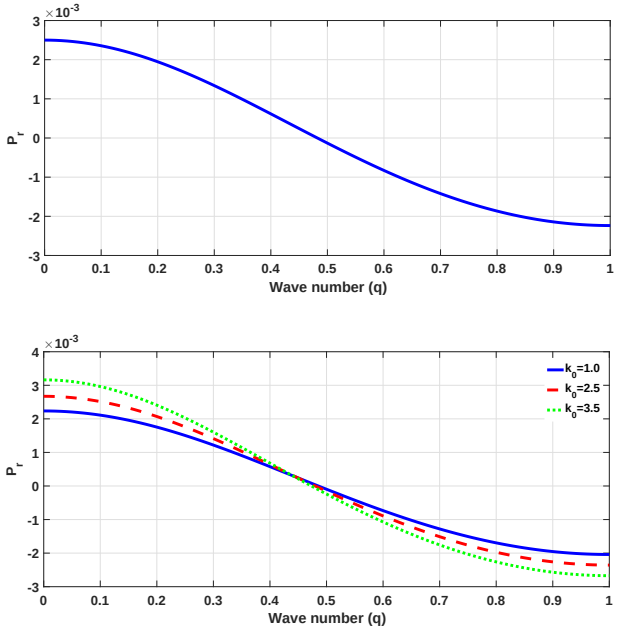

Figure 2.5: A plot of the dispersion coefficient vs. wave number in panel (a) and the influence of memristor coupling depicted in panel (b).

Fig. (2.5a) illustrates the variation of the dispersion coefficient with respect to the wave number while Fig. (2.5b) portraits the influence of electromagnetic induction. In the region where P_r is positive, the influence of electromagnetic induction through the memristor coupling increases P_r and vice versa where P_r is negative.

Fig. (2.6a) shows the variation of the dissipation coefficient R_r with respect to the wave number while Fig. (2.6b) indicates the influence of the memristor coupling. Higher value of memristor coupling is observed to reduce the dissipation coefficient. That is, the dissipation coefficient is seen to be a decreasing function of the memristor coupling.

In Fig. (2.7a) and (2.7b), the variation of the real part of the nonlinearity coefficient (Q_r) with respect to the wave number and the effect of memristor coupling are depicted.

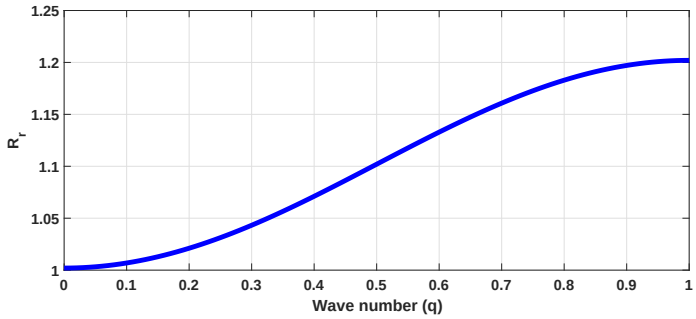

(a)

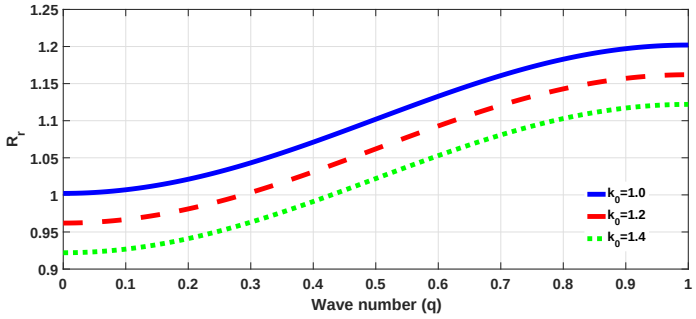

(b)

Figure 2.6: A plot of the dissipation coefficient vs. wave number in panel (a) and the influence of memristor coupling depicted in panel (b).

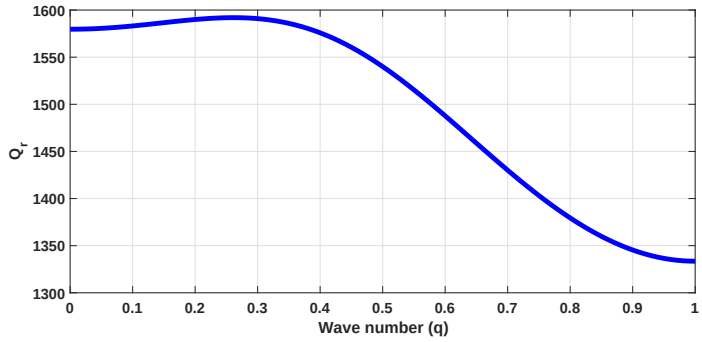

(a)

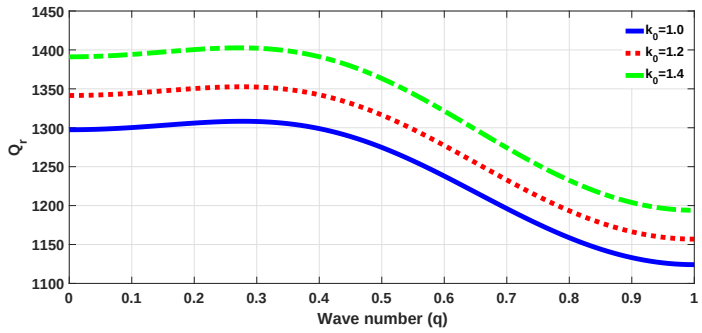

(b)

Figure 2.7: A plot of the real part of nonlinearity coefficient vs. wave number in panel (a) and the influence of memristor coupling depicted in panel (b).

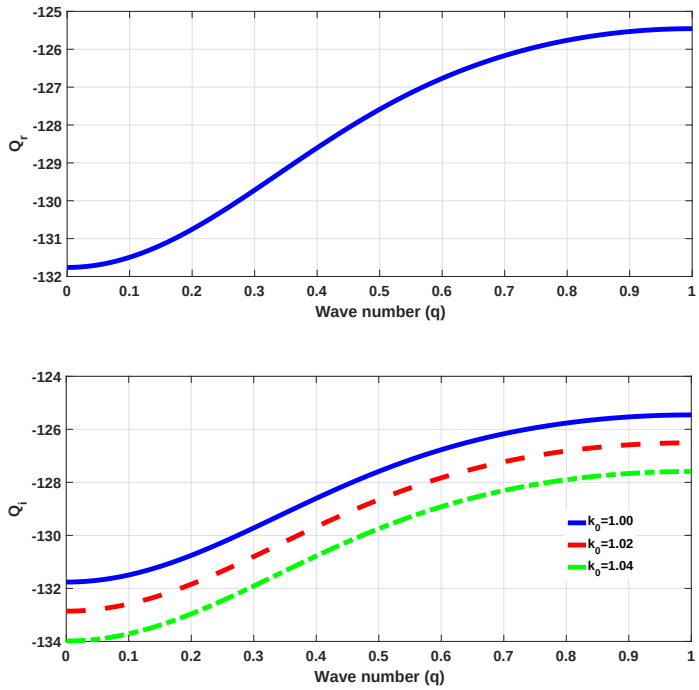

Figure 2.8: A plot of the imaginary part of nonlinearity coefficient vs. wave number in panel (a) and the influence of memristor coupling depicted in panel (b).

Q_r is an increasing function of the memristor coupling. In Fig. (2.8a) and (2.8b), variation of the imaginary part of nonlinearity and the influence of memristor are illustrated. Once again the coefficient is sensitive to the effect of electromagnetic induction translated by the memristor.

According to Benjamin-Feir instability criteria, the stability of the network plane waves depends on the sign of $P_r \times Q_r$. We recall that the plane waves under modulation will become unstable when $P_r \times Q_r$ is positive while the waves will be stable when $P_r \times Q_r$ is negative. Figs. 9 depicts the variation of this criterium with respect to the wave number. It clearly reveals regions where unstable waves are expected in the network structure ($P_r \times Q_r > 0$). It is important to remark that this criterium only indicates region where we expect the propagating plane waves to evolve into a localized periodic wave train and not the manner in the the wave will propagate in the network. The dependence of this criterium on the memristor coupling is also revealed in Figs. (2.9). We remarked from the figure that when the memristor is fixed at 1.0 is increased to 3.0, the critical wave number is observed to reduce from 0.48π to 0.45π.

The clear dependence of the CGLE coefficients and the Benjamin-Feir instability cri-

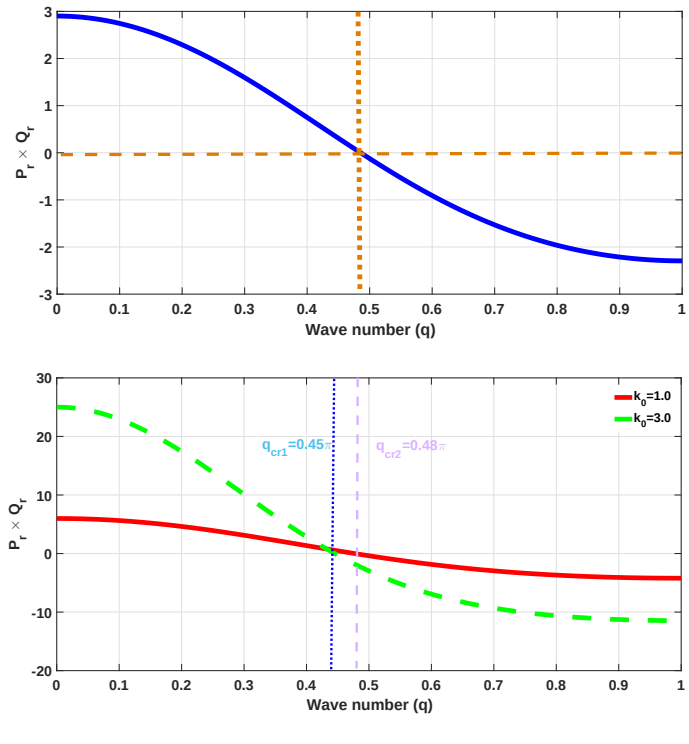

(a)

(b)

Figure 2.9: A plot of the instability criteria coefficient vs. wave number in panel (a) and the influence of memristor coupling depicted in panel (b).

teria on the memristor coupling is important from both physical and biophysical point of view. Firstly, as earlier stated, the whole system dynamical equations are showed to be described by the CGLE. This indicates how electrical signals and waves emitted from the heart sinus node propagates within the physiological environment using both space and time domains in order to regulate heart beat as powerful pacemaker. Secondly, instability criteria and the various solutions of the CGLE being functions of P_r, Q_r, Q_i, R_r, sensitive to the memristor coupling are also highly relevant. It indicates the dependance of wave propagation in the heart physiological environment on magnetic flow effect. In the next paragraph, we shall be dedicated to fining the various solitonic solutions of the CGLE.

2.2.2.2 Exact solutions of the modified CGLE

As earlier stated, getting exact solution of systems of nonlinear equations are usually challenging. The technique employed here was to convert these equations to a more manipulable and integrable equation, without losing it's real characteristics nature. Through the application of a specific perturbation approach and multiple scale analysis in the semi-discrete limit, the obtained integrable equation in this context corresponds the modified

CGLE. In the next paragraph we derive and plot the exact solution of the CGLE. The effect of some important system parameters on the resulting wave solution profile shall be clearly examined.

We rewrite Eq. (2.66) in the form

$$i\frac{\partial A}{\partial T}+\frac{P_r}{2}\frac{\partial^2 A}{\partial X^2}+Q_r|A|^2A=-i(Q_i|A|^2+\frac{R_r}{2})A. \tag{2.71}$$

The left hand side of the above equation corresponds to the well known Nonlinear Schrödinger (NLS) equation whose exact solution is well known, depending on the sign of P_rQ_r. When P_rQ_r is positive, the solution corresponds to envelopes. It's very important to point out from physical perspective that the results of the plot of above clearly illustrates how the region where these envelops are expected strongly depends on the memristor coupling. The general solution of the left hand side of Eq. (2.71) is given by

$$A(X,T)=A_0 sech[A_0(\frac{Q_r}{P_r})^{\frac{1}{2}}X]\exp i(\frac{Q_rA_0^2}{2})T \tag{2.72}$$

The solution of Eq. (2.71) is now obtained by using the change of variable

$$F(X,T)=A(X,T)\exp i(\sigma T), \tag{2.73}$$

where A(X,T) is the general solution of NLSE, given by Eq. (2.71). Inserting Eq. (2.73) in Eq. (2.66) yields

$$\sigma=-i(Q_i|A|^2+\frac{R_r}{2}). \tag{2.74}$$

By making use of useful previous relations, we write the solution as

$$\begin{aligned} v_i(n,t)=&2V_0 sech[V_0(\frac{Q_r}{P_r})^{\frac{1}{2}}(n-V_gt)]\cos[qn+(\frac{Q_rV_0^2}{2}-\epsilon^2\omega)t]\times \\ &\exp[-(\frac{\epsilon^2R_r}{2}+Q_iV_0^2 sech^2[V_0(\frac{Q_r}{P_r})^{\frac{1}{2}}(n-V_gt)])]+0(\epsilon^2), \end{aligned} \tag{2.75}$$

with $V_0=2A_0$. The above equation represents the exact soultion of the obtained CGLE.

The soliton solution of the ionic wave amplitude Eq. (2.66) can also be obtained using the Nozaki and Bekki ansatz [108, 109]. This ansatz is given by

$$A(n,t)=\frac{A_0e^{\varrho}}{1+e^{(\varrho+\varrho^*)(1+i\nu)}}, \tag{2.76}$$

with

$$\begin{aligned}\varrho =&\epsilon q(n - V_g t) - \epsilon^2 \omega t,\\ \nu =&\frac{3Q_r}{2Q_i} \pm \frac{\sqrt{8Q_i^2 + 9Q_r^2}}{2Q_i}.\end{aligned} \tag{2.77}$$

The above ansatz can be written in the form

$$A = A_r + iA_i, \tag{2.78}$$

where

$$\begin{aligned}A_r &= A_0[\frac{e^{-\varrho} + \cos(2\nu\varrho)e^{\varrho}}{2(\cosh(2\varrho) + \cos(2\nu\varrho))}],\\ A_i &= -A_0[\frac{\sin(2\nu\varrho)e^{\varrho}}{2(\cosh(2\varrho) + \cos(2\nu\varrho))}].\end{aligned} \tag{2.79}$$

Using the above ansatz, we obtained

$$v_n(t) = 2\epsilon(A_r \cos\theta - A_i \sin\theta) + \epsilon^2[C + 2(D_r \cos 2\theta - D_i \sin 2\theta)], \tag{2.80}$$

where D_r and D_i are the real and imaginary part of D where

$$\begin{aligned}C =&a_{11}(A_r^2 + A_i^2)\\ D_r =&c_1(A_r^2 - A_i^2) - 2c_2 A_r A_i,\\ D_i =&c_2(A_r^2 - A_i^2).\end{aligned} \tag{2.81}$$

2.2.2.3 Linear stability analysis on a discrete NLS equation

In order to perform the linear stability analysis, we assume solution in the form $\eta_m(\tau) = \eta_0(\tau)e^{i(\nu m - \mu\tau)}$ for the amplitude Eq. (2.30), where the complex amplitude and frequency are related to the perturbation wave number ν via the nonlinear dispersion relation

$$\mu^2 = \frac{R}{Q}\Big[|\eta_0|^2 - \frac{2D\sin(q)}{R}\sin(\nu)\Big]. \tag{2.82}$$

Unstable waves will develop in the modified FHN model if $\mu^2 < 0$. Such a condition depends both on the signs of R/Q and $\Big[|\eta_0|^2 - \frac{2D\sin(q)}{R}\sin(\nu)\Big]$. In fact, $\sin(\nu)$ is bounded, and

$$\text{if} \quad R/Q < 0, \quad \text{then} \quad |\eta_0|^2 > \frac{2D\sin(q)}{R} = \eta_{0,cr}^2. \tag{2.83}$$

When the above condition is satisfied, the plane wave will be say to be unstable under modulation, and wave patterns will be expected in the system. Otherwise, the plane wave will be stable. Along the same line, if $R/Q < 0$, there will instability given that $|\eta_0|^2 > |\eta_{0,cr}|^2$. For this to be possible, we have fixed $\nu = \pi/2$. From Eq. (2.83), we extract the expression of the threshold amplitude given by:

$$\eta_{0,cr} = \sqrt{\frac{2K}{R}\sin(q)}. \tag{2.84}$$

The same approach can be applied on Eq. (2.40) and Eq. (2.47) to yield the same result obtained above and which yields

$$\eta_{0,cr} = \sqrt{\frac{1}{R}}. \tag{2.85}$$

Obviously, the two expressions, although similar, are quite different because one carries the information related to the coupling between the membrane potential and the magnetic flux induced by its memory effects in the neuronal network and the others carry information related to the same effect but in cardiac tissue as well information related to MSC in neuronal network and will be used in the next chapter.

2.2.3 The RK4 numerical integration method

In numerical analysis, the Runge-Kutta methods are a family of implicit and explicit iterative methods, which include the well-known routine called the Euler Method, used in temporal discretization for the approximate solutions of ordinary differential equations [110]. These methods were developed around 1900 by the German mathematicians C. Runge and M. W. Kutta. Amongst those, the RK4 method is the most widely used in programming. Let us examine the main steps of this ubiquitous method. Given the initial value problem specified as follows:

$$\dot{y} = f(t, y), \quad y(t_0) = y(0), \tag{2.86}$$

where y is an unknown function (scalar or vector) of time t, which we would like to approximate; we are told that $\dot{y}$, the rate at which y changes, is a function of t and of y itself. At the initial time t_0 the corresponding y-value is y_0. The function f and the data t_0, y_0 are given. Therefore the formulas of RK4 method are given by:

$$\begin{aligned} y(n+1) &= y(n) + \frac{1}{6}(k_1 + 2k_2 + 2k_3 + k_4) \\ t(n+1) &= t(n) + h \end{aligned} \tag{2.87}$$

for $n = 0, 1, 2, 3, ...$, using

$$\begin{aligned} k_1 &= hf\bigg(t(n), y(n)\bigg) \\ k_2 &= hf\bigg(t(n) + \frac{h}{2}, y(n) + \frac{k_1}{2}\bigg) \\ k_3 &= hf\bigg(t(n) + \frac{h}{2}, y(n) + \frac{k_2}{2}\bigg) \\ k_4 &= hf\bigg(t(n) + h, y(n) + k_3\bigg) \end{aligned} \tag{2.88}$$

where $h > 0$ represents the step-size and n stands for the iteration number. $y(n+1)$ is the RK4 approximation of $y(t_{n+1})$, and the next value $(y(n+1))$ is determined by the present value $(y(n))$ plus the weighted average of four increments, where each increment is the product of the size of the interval, h, and an estimated slope specified by function f on the right-hand side of the differential equation. The RK4 method is a fourth-order method, meaning that the local truncation error is on the order of $O(h^5)$, while the total accumulated error is on the order of $O(h^4)$. Note that the above results are necessary and sufficient to find the numerical solutions of Eq.(2.86) as long as it remains continuous. However, considering a discrete model, one needs moreover to these results, additional conditions called boundary conditions whose choice depends on the studied problem. Throughout our experiments, we have adopted periodic boundary conditions since the different models explored are assumed to be cyclic. For example, a network of N neurons with nearest neighbors interactions obeys the following boundary conditions

$$x(0) = x(N) \text{ and } x(N+1) = x(1). \tag{2.89}$$

Conclusion

This chapter has been organized around two main themes. The presentation of the four improved FHN models; the model with the consideration of the electromagnetic effects induced by a memristive coupling on both neural and myocardial networks, and then the coupled model with MSC. In addition, the analytical methods such as the multiple scale expansion, the linear stability analysis and the RK4 numerical integration method furnished the second part of the chapter. Thanks to the SDA, we have been able to reduce the challenging generic equations to a NLS and CGL equations whose solutions

have been extensively developed in the literature. Then the analysis of the linear stability allowed us to determine the critical amplitude above which the plane wave would become unstable. We are therefore interested not only in the various patterns induced by the MI phenomena, but also in the study of the different phenomena that are associated with the transmission of nerve impulses when taking into account the effects of MSC, EMI and EMR.

Chapter 3

Results and Discussion: Linear Stability Analysis and Spatiotemporal Patterns under Magnetic Flow

Introduction

Wave propagation, synchronization and pattern formation are among the most investigated research areas in field of both cardiac and brain researches. In this chapter we first study MF effect in a discrete FHN neural network. The impact of the MC on the emergence of nonlinear patterns is discussed analytically and numerically, via the MI. Some features of the critical amplitude are given by the relation (2.84) will be presented with an emphasis on the modifications of instability zones when the MC parameters are modified. Also a numerical study will be done on the various generic models in order to confirm our analytical results. Furthermore, other mechanisms of pattern formation is presented when the network is exposed to EMR. Secondly, the same mechanism is applied to the network of myocardial cells and a possible mechanism of heart failure suggested when exposed to continuous EMR. Thirdly, we will study both analytically and numerically the conditions for the formation of synchronized nonlinear patterns in electrically coupled Memristive based FHN under EMR. MSC is showed to importantly modified instability feature. The stability of WP under EMR will also be further discussed. Finally the formation of localized modulated wave in the improved model for myocardial cell through analytical and numerical methods will be presented. We end with a summarized results

of our investigation.

3.1 MF patterns in FHN neural networks

Here we study pattern formation in the FHN model with MF through the MI technique. In that respect, effects of some parameters on nonlinear patterns such as the Memristor coupling, electric synaptic coupling, external stimulus current and electromagnetic radiation ϕ_{ext} are investigated both analytically and numerically.

3.1.1 Analytical analysis of MI

To remind the critical amplitude is a threshold value of the plane wave amplitude above which the plane wave becomes unstable under modulation, and wave patterns are expected in the system. Such critical amplitude should be useful to predict the MI phenomenon in our system. We therefore propose to examine the critical amplitude $\eta_{0,cr}$ of Eq. (2.84) as a function of the wave number q of the plane wave.

We have plotted the critical amplitude vs. the wave number in Figs. (3.1), where the stable and unstable regions are clearly displayed. We take the memristor coupling parameter $k_1 = 1.5$ and the coupling parameter between cells $K = 0.1$. However, since the main purpose is to bring out the effect of the magnetic flux through the memristor coupling parameter, we plot in Fig. (3.1b) the critical amplitude $\eta_{0,cr}$ for three different values of the memristor coupling parameter k_1, namely $0.2, 1.0$ and 1.7. We take the coupling parameter $K = 0.1$. It is observed that the critical amplitude is an increasing function of k_1, thus showing how the electromagnetic induction could be important in the process of intercellular communication in neural networks via MI activation. Comparing Fig. (3.1a) and (3.1b), it is observed that the increasing of the coupling parameter K also increases the critical amplitude $\eta_{0,cr}$.

The direct effect of the latter, however, is to expand the interval of instability, thus increasing the possibility of finding the investigated wave patterns. Unfortunately, this is just a consequence of the linearization of the perturbation around the plane wave solution, and could not give more information on the way wave patterns could emerge in the network, neither can it tell us about the longtime evolution of the perturbed plane wave.

We therefore intend to perform full numerical simulations on the generic Eqs. (2.1).

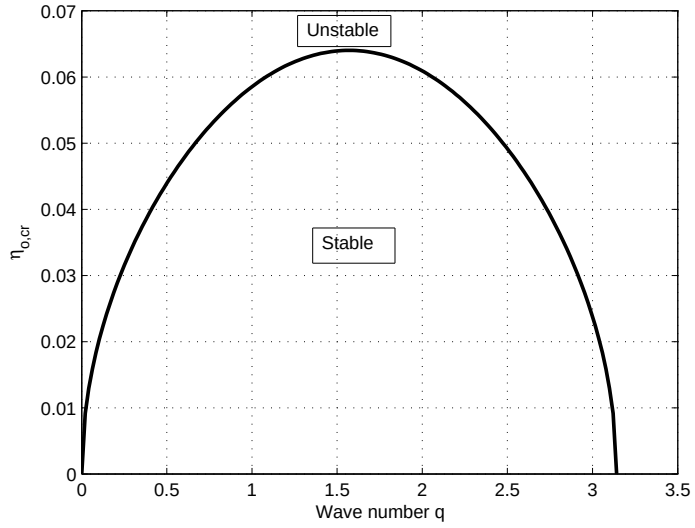

(a)

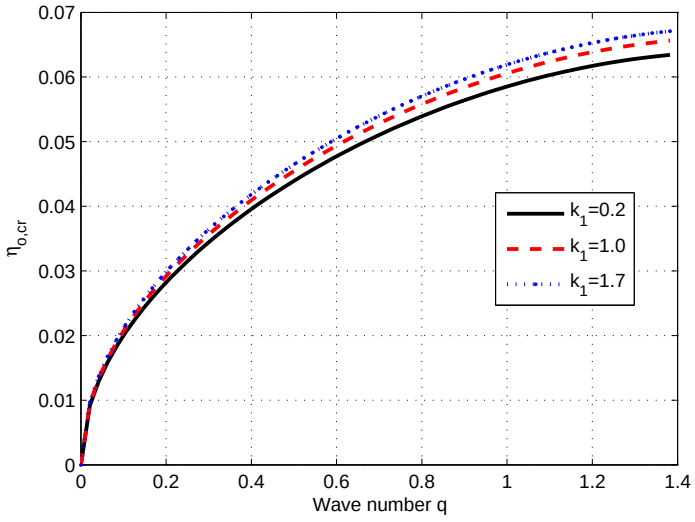

(b)

Figure 3.1: Panels display the critical amplitude $\eta_{0,cr}$, vs. the wave number q, as given by the instability criterion (20). Panel (a) displays the critical amplitude for $k_1 = 0.1$ and $K = 0.05$, while panel (b) shows how $\eta_{0,cr}$ is an increasing function of the MC parameter for $K = 0.5$

3.1.2 Numerical analysis of MI

The linear stability analysis does not give any information about the long-time evolution of the modulated waves, since it is mainly based on the linearization around an unperturbed plane wave. We therefore intend to perform full numerical simulations on the generic system given by Eq. (2.1). Results are obtained via the fourth-order Runge-Kutta computational scheme with periodic boundary conditions and time-step $\Delta t = 10^{-2}$. The

number of FHN neurons forming the network has been chosen in order to avoid wave reflexion, while initial conditions correspond to the combination of the respective solutions used both in the analytic calculations and through the linear stability analysis. The wave number q has been chosen in regions of instability as $q = 0.15\pi$, while we have considered $\nu = 0.1\pi$. For further investigations, the MF effects are investigated and the features of the subsequent waves patterns of the membrane potential $v_n(t)$ are discussed.

In Figs. (3.2), we perform the numerical simulations for $K = 0.05$. That is to say we have considered two nearest neighbors coupling in a weak coupling regime. A weak coupling between neighboring cells is also related with a situation that arises in the study of non-linear oscillating waves in the β-cell islets of the pancreas, which secrete insulin in response to glucose in the blood [111]. In the detected regions of instability, one should expect different behaviors of the system, depending on the value of k_1, which indubitably influences the instability features. Therefore, we can control the feature of pattern through the variation of parameter k_1. Then, we fix all the other parameters and play on the values of k_1 for the suitable phenomena of memristor coupling in pattern formation to be described. It is well known that time and space are of high importance in the process of interneuronal communication, some good examples being visual, sensory motors and olfactory cortices [112]. Therefore, we represent the spatiotemporal dynamics of the membrane potential in Figs. (3.2) and (3.3) under low dispersive effect. We use two different values of k_1, namely k_1=1.5[Fig. (3.2)] and k_1=2.5[Fig. (3.3)]. As one can remark, the system presents multiple states comprised of patterns with different topologies. The obtained patterns confirm our analytical expectations as one observes patterns of waves. This once more confirms the fact that wave patterns are possible in all systems where dispersion and nonlinearity are present. In Fig. (3.2) that is for k_1=1.5, we observe the formation of quasi-periodic wave patterns with swimming behavior. As interestingly observed in Fig. (3.2), the (X,Z) plane presents breathing modes. Such generated rhythmic behaviors like breathing or swimming have been observed in central pattern generators (CPGs) [113] and are particularly important in brain researches due to their striking capacity to produce a considerable variety of coordinated patterns in response to their surrounding changes and their behavior needs. Inspired by the fact the CPGs have some similarity and are able to share their morphological dynamical properties, Yuste et al. [114] introduced and developed the idea of considering CPGs as the theoretical framework to understand cortical micro-circuits. The oscillations connected to the rate

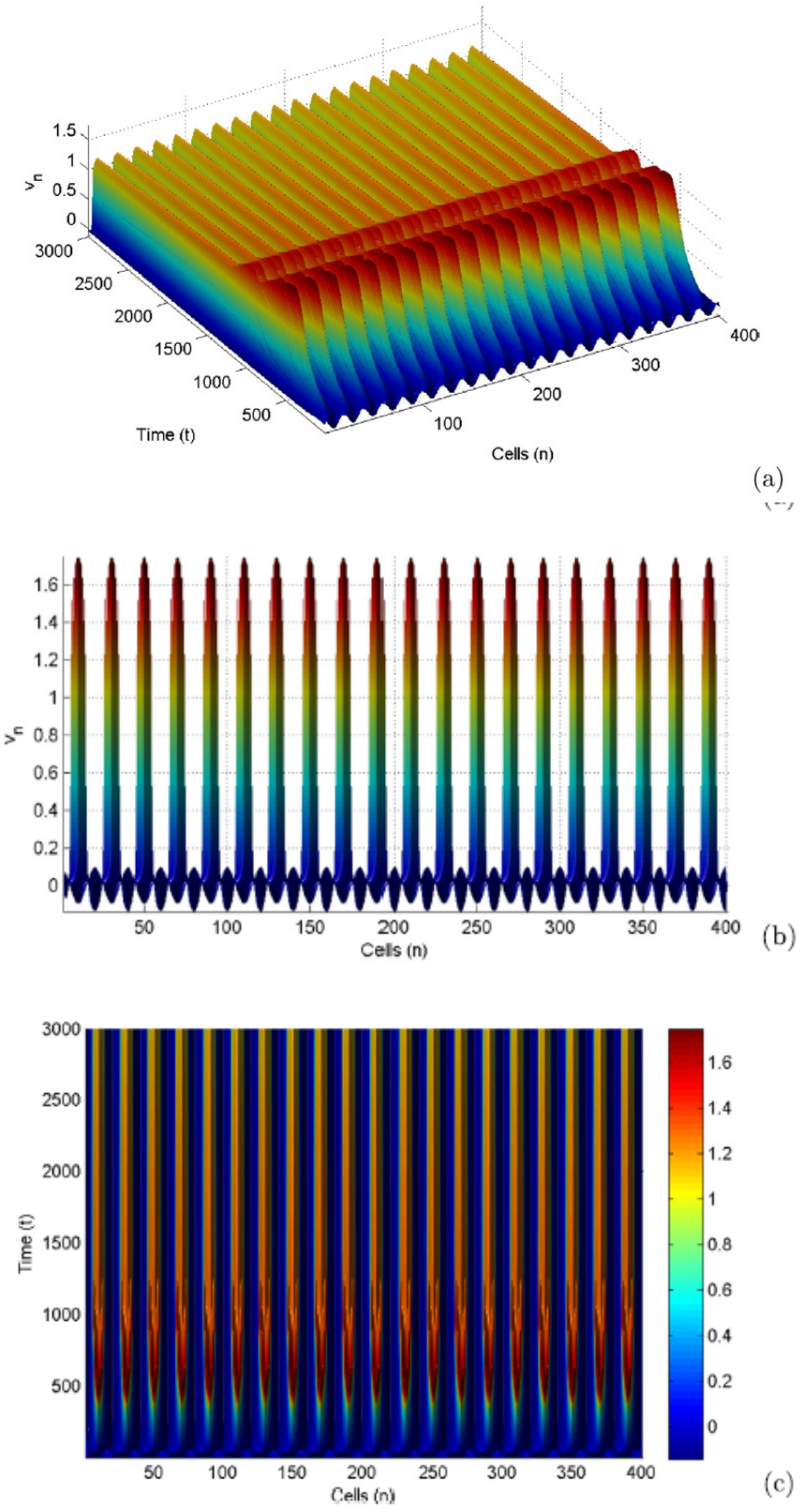

Figure 3.2: Panels show the spatiotemporal features of patterns at fixed parameters k_1=1.5, $K = 0.05$ and $I_{ext} = 0.05$, (a) 3D feature, (b) X, Z plane and (c) X, Y plane

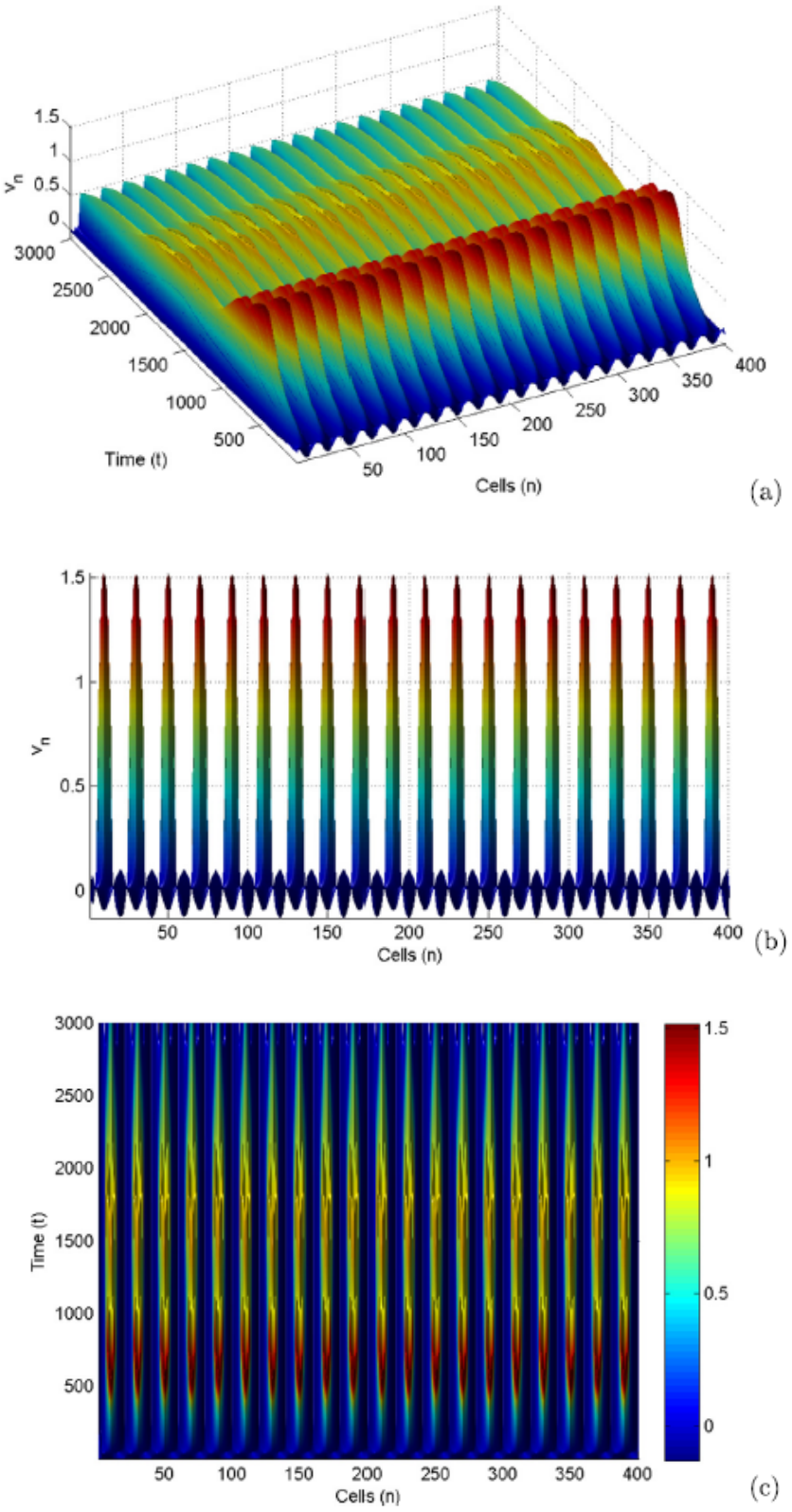

Figure 3.3: Panels show the spatiotemporal features of patterns at fixed parameters k_1=2.5, $K = 0.05$ and $I_{ext} = 0.05$, (a) 3D feature, (b) X, Z plane and (c) X, Y plane

of breathing are very tied to bringing sensory data together as perceptions [115]. In fact, breathing is highly connected to altering perceptions related to emotions and different physical activities [115].

Still, we do not change the value of k_2, but as the memristor coupling parameter k_1 increases, we expect the formed patterns to change their features as this is the case for Fig. (3.3), where we have fixed $k_1 = 2.5$. The features observed in Fig. (3.2) are affected, as swimming patterns are now more visible. Then, feedbacks can also modulate the traveling waves and can produce complex spatial patterns in various developmental contexts [116]. We observe also in Fig. (3.3c) that each structure generated is well separated from each other. Also, the amplitude of patterns decreases when the memristor coupling parameter increases, however this leads to a more observation of swimming patterns in the second case. Synchronization can be enhanced at different levels, that is, the constraints on which the synchronization appears. Those can be on the trajectory amplitude, requiring the amplitudes of oscillators to be equal, giving place to complete synchronization [117]. Figs. (3.2c) and (3.3c) give an example of this where patterns of membrane potential display synchronized states described by the obtained quasi-periodic patterns. Such synchronized patterns may represent a generic property of globally coupled neural networks, which might be of interest for experimental studies. There are evidences that such patterns may be related to a series of processes in the brain such as movement control and cognition [118–120]. Although quasi-periodic-like behaviors are significative for brain functions, they should be controlled to avoid some pathological brain rhythms such as the Parkinson's disease and epileptic seizure, which have identical physiological anatomic structures [121].

In Fig. (3.4), the numerical simulations are performed for $k_1 = 2.5$ under higher coupling strength between cells $K = 0.5$, while the other parameters remain unchanged. It is observed that the increasing of the coupling strength K more depicts the breathing in swimming of patterns as time progresses. In fact, as one can observe in Fig. (3.4), the initial wave gives rise to additional vagueness that tend to form visible swimming patterns. More interesting, such dynamical properties are seen in many forms of cortical activity [122]. On the other hand, strong coupling between neurons under the effect of electromagnetic radiation can give rise to visible swimming or breathing patterns in excitable systems.

We have plotted in Fig. (3.5), the spatial evolution of patterns for $K = 0.5$ and $k_1 = 2.5$. These patterns, being plotted at different times, see their behaviors change as

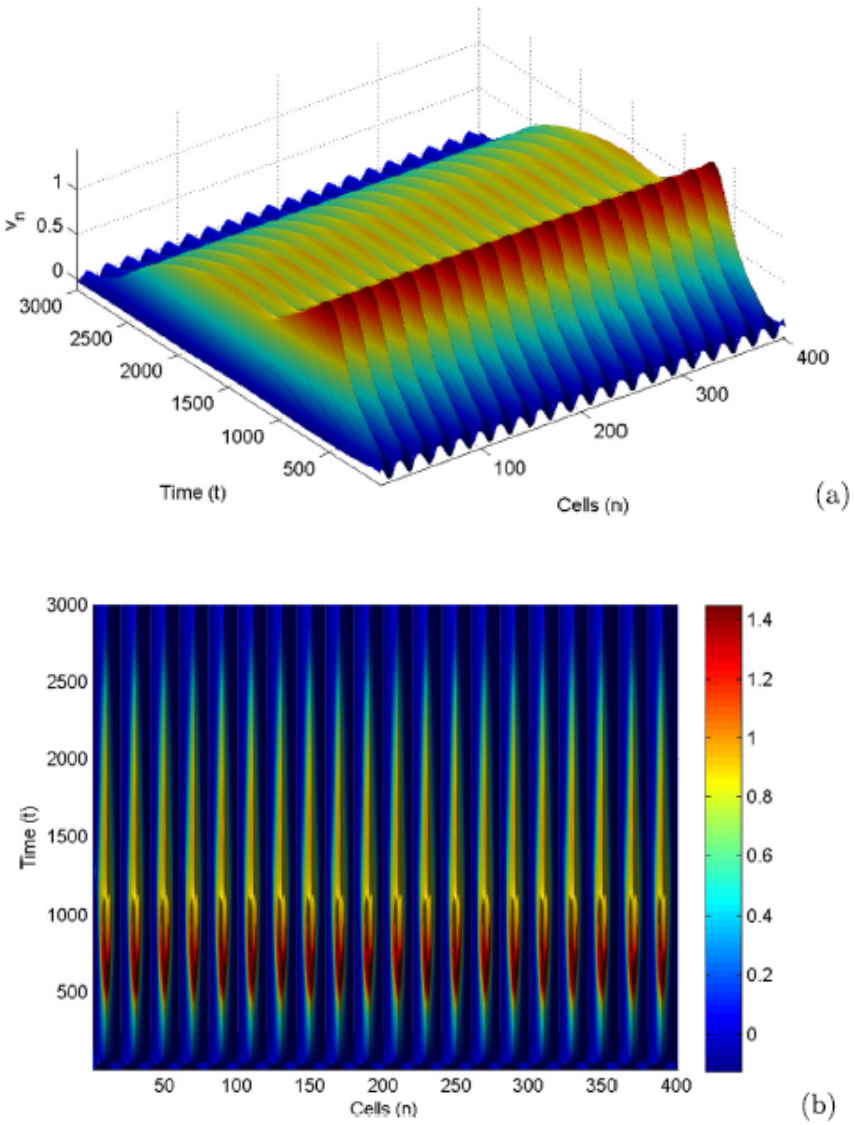

Figure 3.4: Panels depict the (X,Z) and (X,Y) planes of spatiotemporal features of patterns for K=0.5 at fixed parameters k_1=2.5 and $I_{ext} = 0.05$

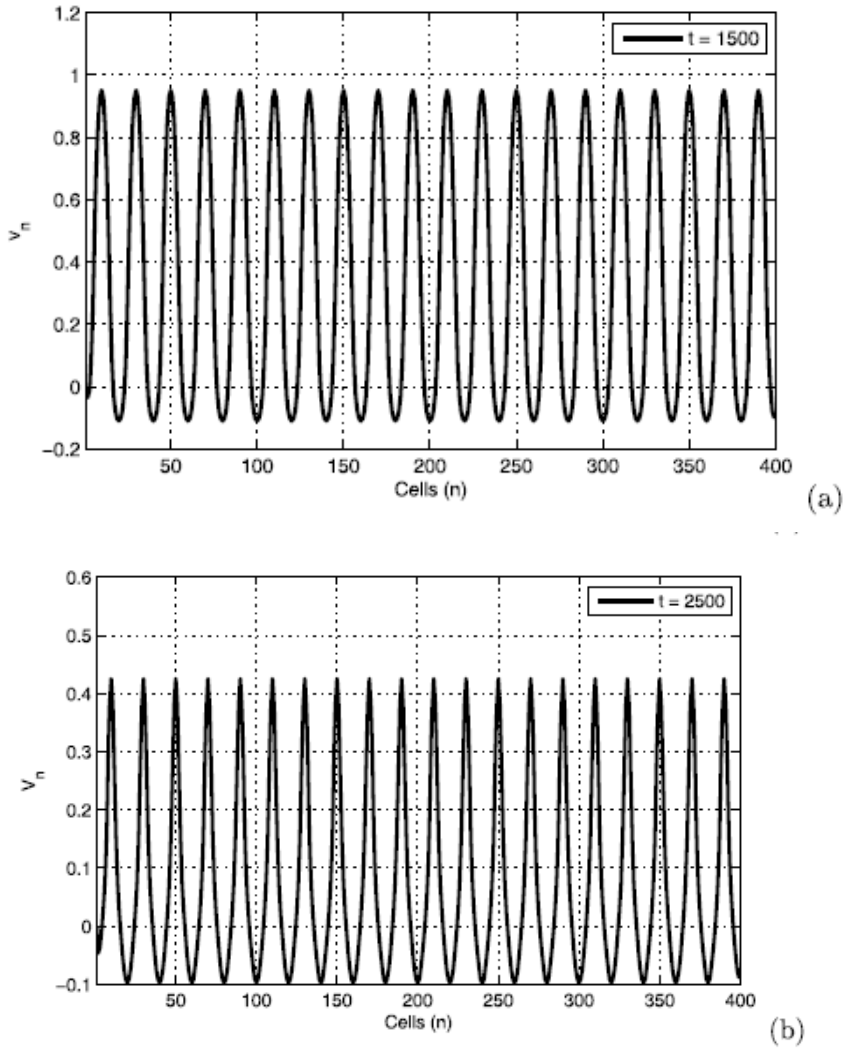

Figure 3.5: Panels show the spatial features of patterns at fixed parameters $k_1 = 2.5$, K=0.5 and $I_{ext} = 0.5$ at: (a) t=1500 and (b) t=2500

time increases. Remarkably, at $t = 2500$, series of spikes are obtained [this can be seen in Fig. (3.5b)], and their behaviors clearly picture memristor coupling effects. We clearly notice that cells display the same dynamics. These oscillations depicted in Figs. (3.5) are nonlinear oscillations with some features of synchronization as already mentioned above. Synchronous oscillations from groups of neurons have been shown to correlate with quickly changing mental states, such as absorbing and analyzing new information [123]. Along the same line, synchronized firing of neurons also forms the basis of periodic motor commands for rhythmic movements [124]. We should however stress that the observed behaviors reinforce the efficiency in describing waves flowing in discrete networks of coupled cells which can behave as excitable media.

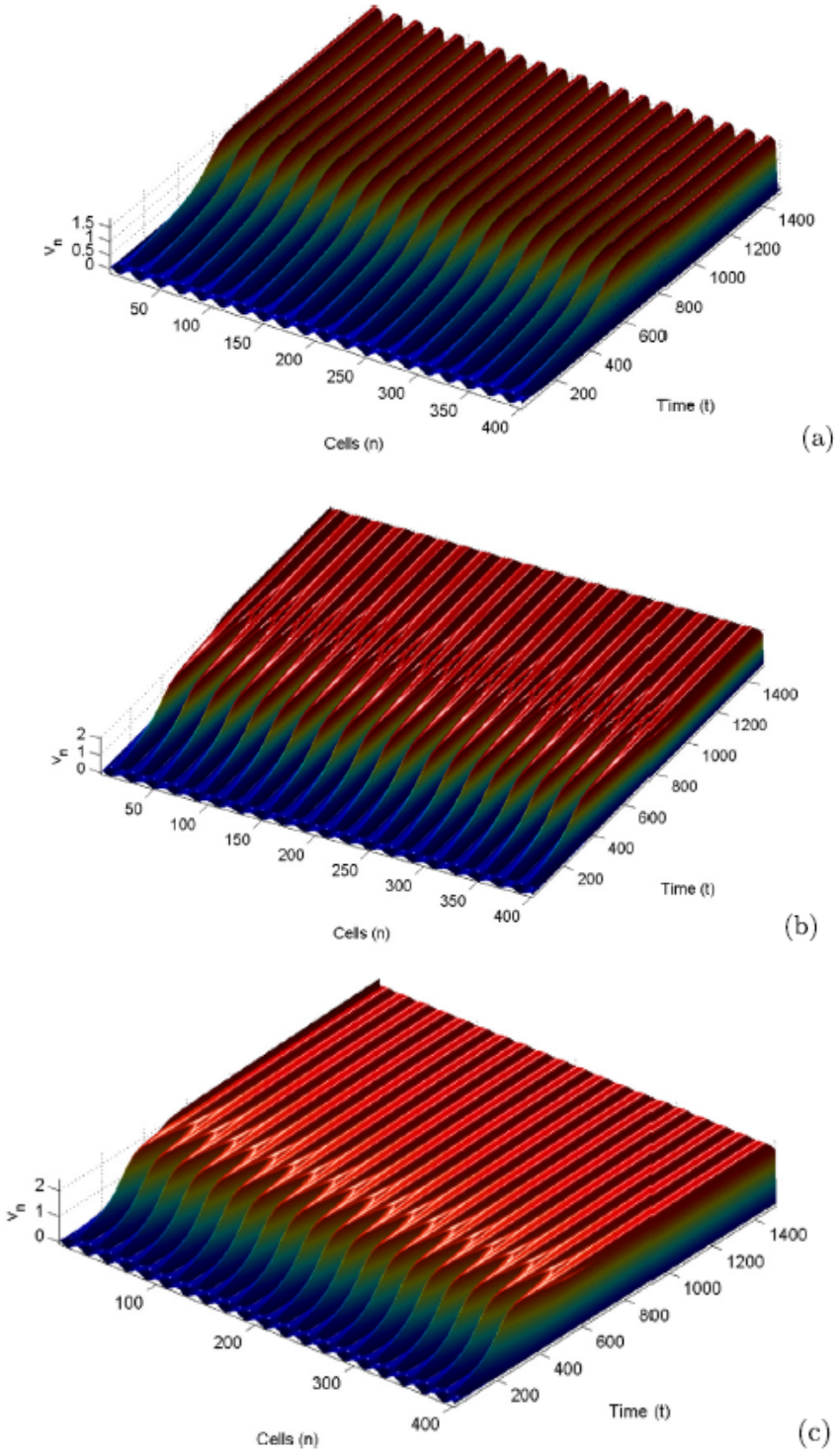

Figure 3.6: Panels show the features of patterns by setting different transmembrane currents at fixed parameters K=0.5, ω=0.05, $k_1 = 1.5$ for (a) I_0=0.01, (b) I_0=1.00 and (c) I_0=2.50

In Fig. (3.6), distinct patterns for membrane potential are observed. The transmembrane current is taken in the form of a periodical function $I_{ext} = I_0 sin(\omega t)$ and I_0 is selected to detect the mode response of electrical activities. In Fig. (3.6a) for $I_0 = 0.01$, it is observed the generation of pulses. However, when I_0 is increased, these pulses are linked each other from the time $t = 800$ for $I_0 = 1$ and from $t = 600$ for $I_0 = 2.5$. In fact, patterns are individually localized at the beginning, but after a given time, there appear linked structures which suggest connectivity between cells. Interestingly, the linked structures, when the transmembrane current is appropriate should tend to become linear as displayed by Fig. (3.6c). In the latter, information is effectively shared between all the cells from $t = 600$, so that as time increases, intercellular communication tends to become perfect. Then Fig. (3.6) reveals that various states for patterning can be observed by varying the transmembrane current. These results confirm those recently obtained by Ma *et al.* [28] who found that transmembrane current can be responsible for complex modes of the action potential in excitable media.

It is found in Figs. (3.7) that the electrical activity of cells can present multiple types of pattern with increasing the angular frequency. In Figs. (3.7a) that is for $\omega = 0.1$, as displayed in Figs. (3.6), from $t = 600$ intercellular communication is favored due to the emergence of linked structures with solitonic features. In Figs. (3.7b), that is for $\omega = 0.5$, patterns are robust and periodically separated in time while in Figs. (3.7c), that is for $\omega = 1.5$, they appear as individual entities in the form of lobes. Spatiotemporal pattern and synchronization dynamics are very crucial in understanding normal function and dysfunction of neuronal systems, but they rely on specific frequencies. Experimentally, such frequencies are known and lots of contributions have been devoted to their subsequent wave patterns, especially those related to pathological rhythmic brain activity in ParkinsonŠs disease, essential tremor, and epilepsies.

In Figs. (3.8), different feedback gains k_1 are applied by selecting $\omega = 0.5$ and $I_0 = 1$. It is observed various patterns depend-ing of the choice of k_1. As k_1 increases, the formed patterns display rows which are obviously separated. The linear stability analysis could not predict the emergence of separated structures, which in present work is new and appears to be a consequence of discreteness effects. This is the main characteristic of MI, which involves sequences of lattice cells in collective oscillations. These results confirm the fact that modulated traveling waves and complex spatial patterns can be produced by feedbacks in various developmental contexts [116]. The numerical results reported in

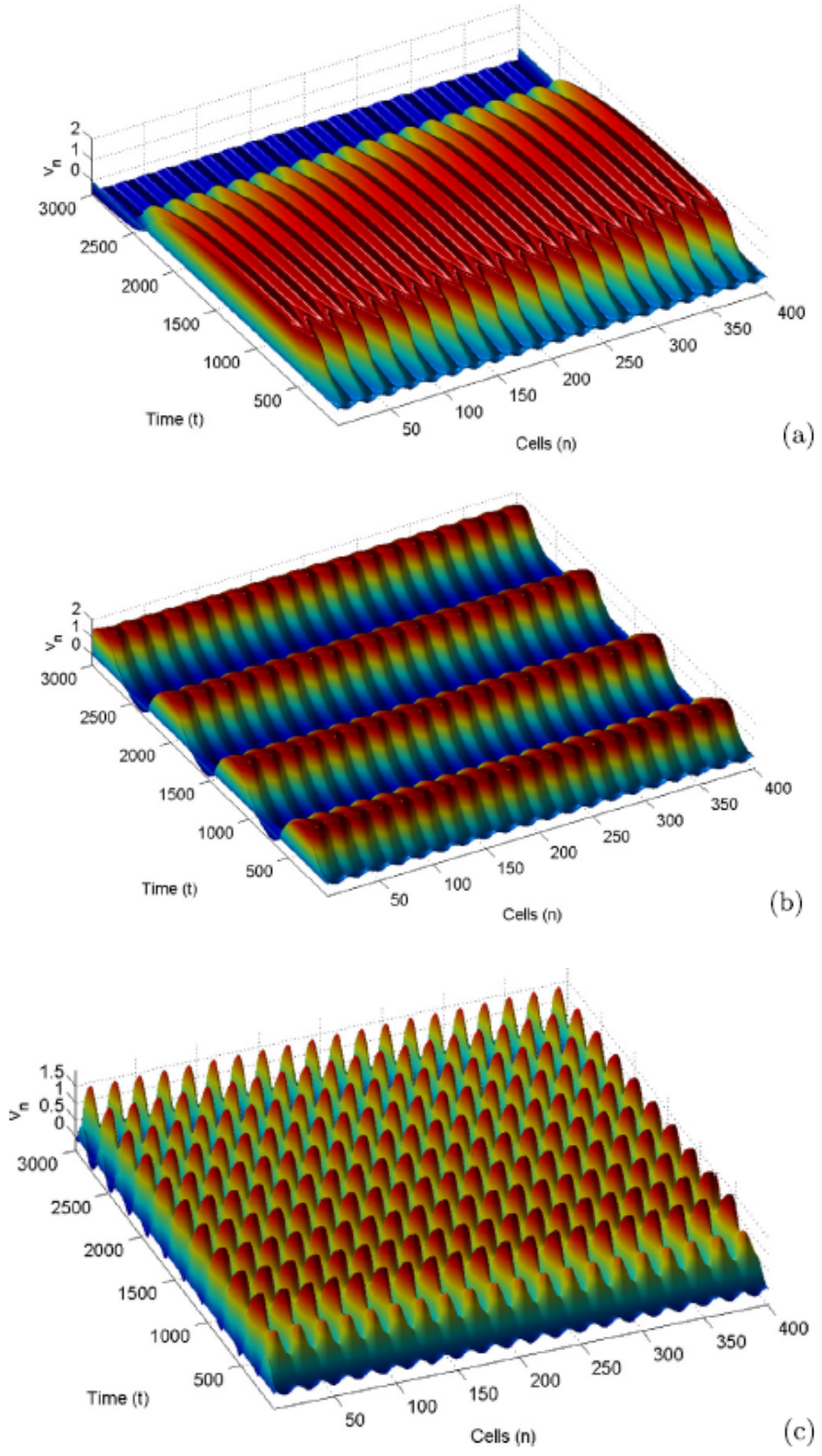

Figure 3.7: Panels show the features of patterns by setting different values of angular frequency of transmembrane currents at fixed parameters $K = 0.5, k_1 = 2.5, I_0 = 1$ for (a) $\omega = 0.1$, (b) $\omega = 0.5$ and (c) $\omega = 1.5$

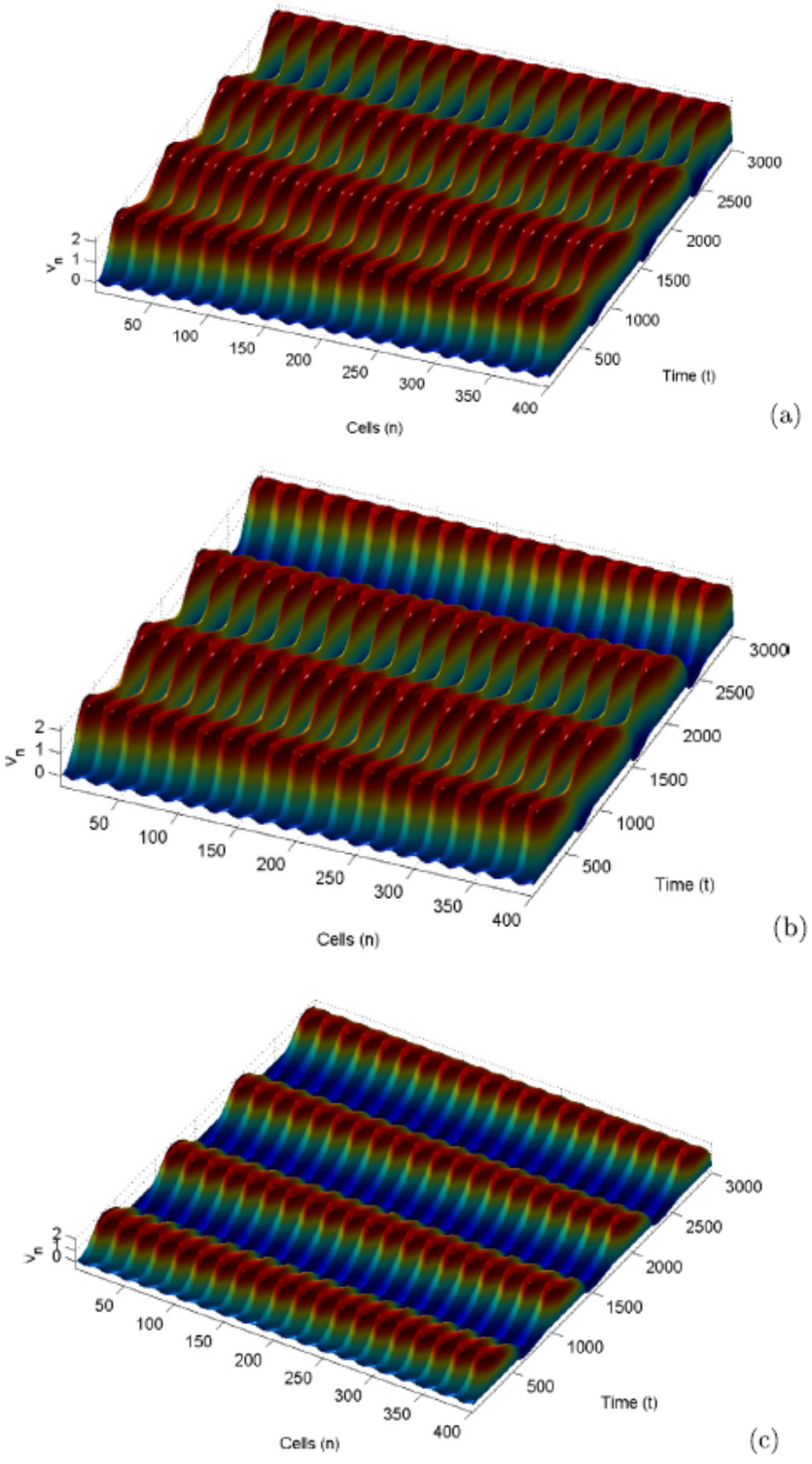

Figure 3.8: Panels show the features of patterns when induction current $k_1\rho(\phi_n)v_n$ is generated with different intensities. The parameters are selected by $K = 0.5, \omega = 0.5, I_0 = 1.0$ for (a) $k_1 = 0.1$, (b) $k_1 = 0.5$ and (c) $k_1 = 2.5$

this subsection 3.1 can be extended to account for these processes.

As a partial conclusion, the above work was devoted to pattern formation via the modulational instability analysis in excitable media under the effect of electromagnetic induction. We have shown that a simple and physically-motivated modification of the FitzHughŰNagumo equations can mimic the coexistence of dynamical motifs seen as swimming or breathing patterns. Analytically, it has been shown that increasing the value of the feedback gain considerably modifies the instability features. Numerical simulations have been carried out to confirm analytical predictions. The results have suggested that the effect of electromagnetic induction through the memristor coupling in excitable cells enhances efficient information transfer among coupled cells, therefore can lead to memory signaling. However, another point of interest is to understand in the main time the effect of MF in coupled myocardial cell interneuronal communication under electromagnetic radiation.

3.2 MF patterns in FHN cardiac tissue under electromagnetic radiation

During the time period when electrical waves of excitations are emitted from the sinus node and spread among cardiac tissues, a time varying electromagnetic field is induced. Here we study pattern formation in the FHN myocardial model with MF through the MI technique. In that respect, effects of some parameters on nonlinear patterns such as the Memristor coupling, external stimulus current and electromagnetic radiation are investigated both analytically and numerically.

3.2.1 Analytical analysis of MI

In engineering nowadays, modulated waves are highly preferred to non-modulated ones since they can be transmitted along much longer distances. It generally has the form of soliton-like objects and one of the mechanisms to generate such waves is via MI. MI has been demonstrated to be a pathway to energy localization in bio-molecules and in discrete systems, in general. It results from the interplay between nonlinearity and dispersion. To remind, modulated waves generally arise when the plane wave solution of the system equation, becomes unstable under slight modulation. Using the same stability of MI used

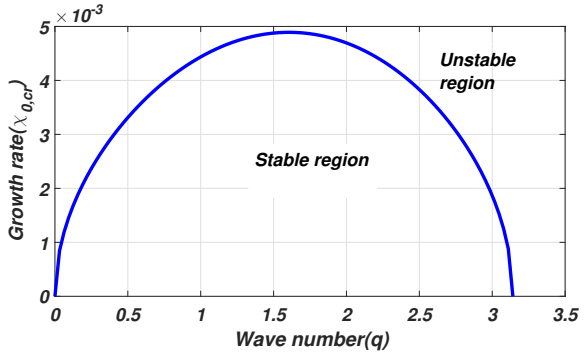

Figure 3.9: Figure displays the plot of critical amplitude $\chi_{0,cr}$, vs. the wave number q, as given by the instability criterion (3.5), with $k_0 = 1.6$ and $K = 0.01$

in the previous section, we construct an approximate solution $v_n(t)$ of Eq. (2.40) as

$$v_n(t) = \epsilon\chi(m,\tau)e^{i(qn-\omega t)} + \lambda(\epsilon^2) + c.c, \tag{3.1}$$

from where we can now express the slightly perturbed solution of the paradigm equation as

$$\chi(m,\tau) = \chi_0 e^{i(\vartheta m - \Gamma\tau)} \tag{3.2}$$

with the wave number ϑ and the frequency of perturbation Γ obtained by inserting Eq. (3.1) in Eq.(2.4). It gives the nonlinear dispersion relation

$$\Gamma^2 = \frac{1}{\gamma(q)}[|\chi_0|^2 - \frac{2K\sin(q)}{R}\sin(\vartheta)]. \tag{3.3}$$

Unstable waves will emerge when $\Gamma^2 < 0$. This can be achieved by technically considering the sign of $\gamma(q) = \frac{Q}{R}$ and $|\chi_0|^2 - \frac{2K\sin(q)}{R}\sin(\vartheta)$. We are deally with a boundary condition problem as ϑ is bounded due to discreteness effect, thus we set $\sin(\vartheta) = 1$. The quantity $\gamma(q) < 0$, implies MI result when $|\chi_0|^2 - \frac{2K\sin(q)}{R} > 0$. We can now express the later term as

$$|\chi_0|^2 > \frac{2K\sin(q)}{R} = \chi_{0,cr}^2. \tag{3.4}$$

When the above condition is not respected, the wave remains stable and will propagates via the lattice without distortion. The instability condition can now be stated exclusively as

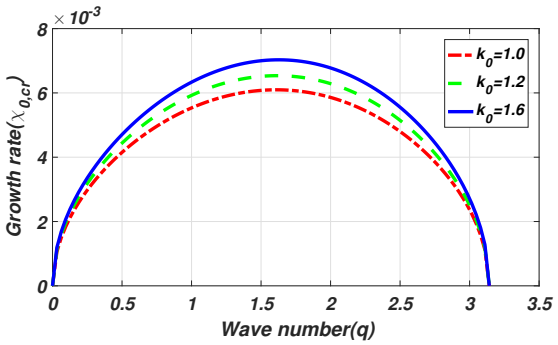

Figure 3.10: Figure displays the plot of critical amplitude $\chi_{0,cr}$, vs. the wave number q, as given by the instability criterion (3.5) for different values of memristor coupling k_0, with $K = 0.02$. We observe; $\eta_{0,cr}$ is an increasing function of memristor coupling k_0

$$\gamma(q) < 0; |\chi_0|^2 > \chi_{0,cr}^2 \tag{3.5}$$

It's expected from the above analyzes that when the parameters fall inside the unstable region, unstable patterns of waves should be observed via the cell lattice through the activation of MI.

We have therefore plotted the critical amplitude $(\chi_{0,cr})$ versus(vs.) the wave number(q) in Fig.1, where the stable and unstable regions are clearly presented. In order to picture the effect of induced electromagnetic gain created by the external electromagnetic field, we have also plotted $\chi_{0,cr}$ vs. q for different values of the memristor coupling k_0 as indicated in Fig. (3.9). The critical amplitude is seen to be an increasing function of the memristor coupling, thus showing how important electromagnetic induction created from the external field could be vital in the process of intercellular myocardial communication through the activation of MI. The reader should remark that in Fig. 1, the gap junction coupling was set at $K = 0.01$ and in Fig. (3.10), its value has been increased to $K = 0.02$. Comparing Fig. (3.9) and Fig. (3.10), there is an increased in threshold amplitude as the value of the gap junction coupling is increased. This is an indication of its importance in cell communication due to its ability to modify instability features. In the next paragraph this analytical prediction will be confirmed through numerical simulation by using initial conditions whose parameters values are chosen from the instability region of our analytical prediction.

3.2.2 Spatiotemporal patterns and biological implications

We numerically integrate the generic model of Eq. (2.2) using the fourth-order Runge-Kutta computational scheme with time-step h=0.01 and periodic boundary conditions. The initial conditions are selected to be a slightly modulated plane waves [**?**, 31] with $q = 0.01\pi, a_0 = 0.001$, $\vartheta = 0.12\pi$ and $v_0 = 0.01$. The corresponding values of w_0 and ϕ_0 follow from Eqs. (2.35);

$$\begin{aligned} v(t=0) =& v_0(1 + a_0\cos(qn))\cos(\vartheta n), \\ w(t=0) =& w_0(1 + a_0\cos(qn))\cos(\vartheta n), \\ \phi(t=0) =& \phi_0(1 + a_0\cos(qn))\cos(\vartheta n). \end{aligned} \tag{3.6}$$

Our aim in this numerical analysis is to bring out the impact of the effects of electromagnetic induction through the memristor coupling and radiation imposed as a periodic forcing on the magnetic flux variable equation, on the occurrence of unstable wave patterns activated by MI.

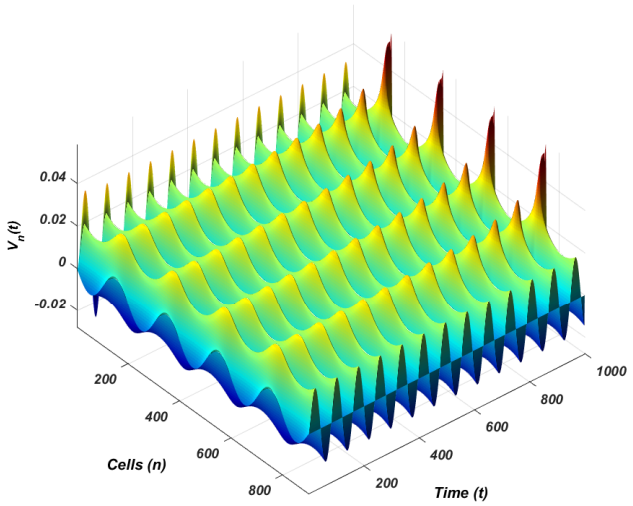

Figure 3.11: Figure shows the spatiotemporal features (the 3D feature) of patterns for the magnetic flux gain $k_0 = 2.51, t = 200$. Other parameter values used are; $K = 0.5, I_0 = 0.035$ and $\omega = 0.8$

It is well known that time and space are of high importance in the process of intercellular communication, with some good examples being visual, sensory motors and olfactory

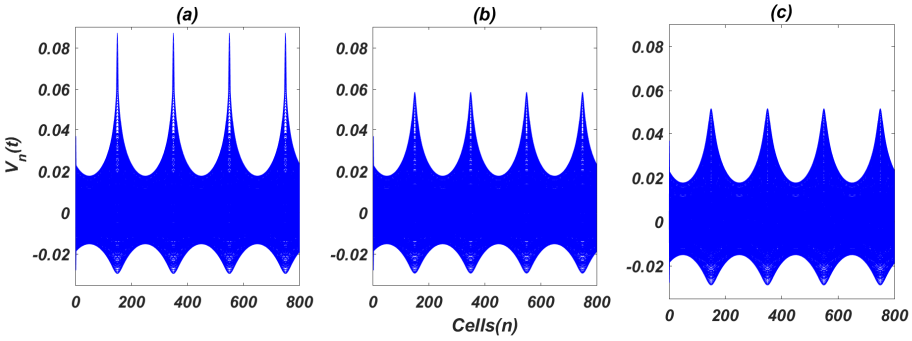

Figure 3.12: Panels show the spatial features of patterns for different magnetic flux gain k_0; (a) 2.51, (b) 2.53 and (c) 2.58

cortices [125]. Therefore, we represent the spatiotemporal dynamics of the cardiac action potential under low dispersive effect. In Fig. (3.11), the spatiotemporal features(3D) of patterns for the magnetic flux gain $k_0 = 2.51$ is represented. Using three different values of magnetic flux gain, the spatial features(2D) of the patterns are represented[Fig. (3.12)]. As a first remark, the introduced plane wave breaks into trains of waves, which have the appearance of soliton-like shape objects. This is as expected from the linear stability analysis, when appropriate values of wave numbers q and k_0 are chosen. This suggests that the fundamental question for the existence of nonlinear excitations with soliton-like shape in our myocardial tissue model, as predicted by analytical predictions, appears to have been answered by numerical experiments. Such excitations are known to be robust and usually important in the coherent transfer of energy. This once more supports the suggestion that wave patterns exist in all systems where there is the presence of dispersion and nonlinearity. We recall that the localized unstable wave oscillations obtained in this work have been reported in many other biophysical systems, where under certain conditions , they can move and transport energy along the system [126, 127]. In [126], such localized oscillations are known to be precursors of bubbles that appear in the thermal denaturation of DNA and have been reported to describe the breaking of the hydrogen bonds linking two bases.

Furthermore, it's also expected that depending on the value of k_0, one should observe different behaviors of the system in the detected regions of instability, which should unquestionably affects the instability features. We can thus control these characteristics features of pattern through the variation of parameter k_0. As one expected, there is a modification in the obtained pattern as the value of the magnetic flux gain, via the

memristor coupling is increased. We observe in Figs. (3.12), how the localized patterns have been modified. There is a gradual decreased in amplitudes of the soliton-like shape objects. Such decreased in amplitude could be associated with the suppression of oscillating behavior of electrical activities, where heartbeat can be terminated. More so, the effect of electromagnetic radiation can be detected and investigated when neurons or cells are exposed to electromagnetic field [128]. A periodical type of electromagnetic radiation($H_0 \cos(\Omega t)$) is imposed to change the distribution of magnetic field and also the magnetic flux. To discern this effect of electromagnetic radiation, the forcing current I_{ext} is set at I_0 =0.035 and ω =0.08. In Figs. 5, different values of radiation amplitude H_0 are applied to observe the influence on pattern formation. The angular frequency is kept constant at Ω =0.05. Figs. (3.13) reveal localized structures appearing in the form of a breather-like coherent excitation. Zdravkovi et al. [127] suggested these oscillations to be triggering signal for motor proteins to start moving along microtubule systems. In the brain, such generated rhythmic behaviors like breathing or swimming have been reported in the central pattern generators(CPGs) [113] and are particularly important in brain researches due to their striking capacity to produce a considerable variety of coordinated patterns in response to their surrounding changes and their behavior needs. In fact, breathing is highly connected to altering perceptions related to emotions and different physical activities [115].

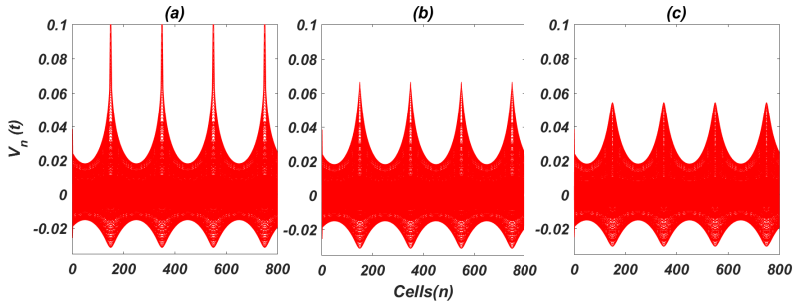

Figure 3.13: Panels show the spatial features of patterns for the electromagnetic intensity (a) H_0=2.50, (b) H_0=2.54 and (c) H_0=2.65, with $k_0 = 1.50$

This result has clearly revealed mode transition in oscillating behaviors as the angular frequency of the external electromagnetic radiation is increased with strong amplitude. The induced multiple modes in electrical activities have been reported to be consistent with biological experiments [129]. This dynamical response could be related to the magnetization and polarization of the heart medium. That is, when the external radiation is low,

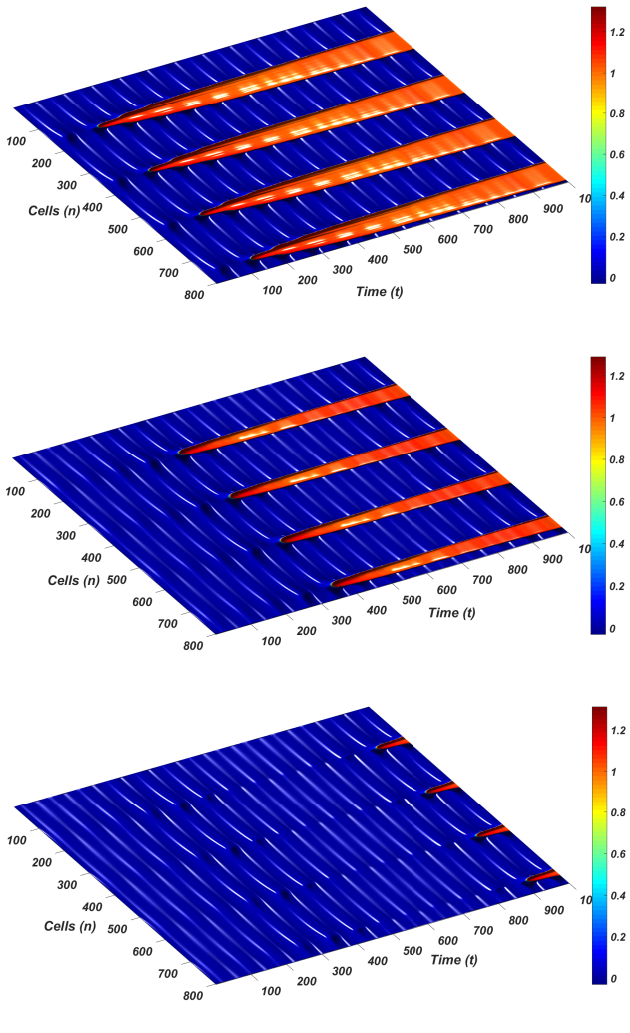

Figure 3.14: Panels show the spatiotemporal features of patterns for the memristor coupling parameter (a) k_0=0.50, (b) k_0=1.50 and (c) k_0=2.04, with H_0=1.3

the medium can absorb the radiation, with the cell still being able to select appropriate modes in electrical activities. In the case of a high-frequency electromagnetic radiation, the heart medium can be polarized and magnetized alternatively when the medium is exposed to an external electromagnetic field. This effect can thus contribute in suppressing electrical behaviors. This confirms the work reported in [28]. It could thus account for information encoding of myocardial cells. In the next paragraph, parameters are set as $H_0 = 1.3, I_0 = 0.035, \omega = 0.05, \Omega = 0.08$, then different feedback gains k_0 are applied to observe its influence on pattern formation. The results are presented in Figs. (3.14).

Figs. (3.14) presents spatially broadened pulses, or front waves, ubiquitous in excitable media like neurons and cell membranes [130]. In the heart, they have the responsibility

to trigger harmonized contractions, whose failure can lead to important physiological disturbances [131]. We remark also that, as the value of the feedback k_0 is increased, the amplitude of the pulses are greatly reduced, with a diminishing pattern. Once again such disappearing patterns suggest once more the suppression of myocardial cell excitations. As such, the normal electrical activities of myocardial cells can be seriously disturbed. In the next paragraph, we present the effect of increasing the intensity of the trans-membrane current at a constant angular frequency (Ω =0.05). The observed patterns are presented in Figs. (3.15).

Figs. (3.15) present pulses which are linked together as the intensity of the trans-membrane current is increased, notably at t=300 and t=500 in Figs. (3.15c). This formation of some extra-patterns, between the localized mode as the intensity of forcing current is increased, could mediate intercellular communication among myocardial cells. This once more prove that MI is an excellent and a direct mechanism that lead to the formation of solitons and train of waves in systems where there are permanent competitive effects between nonlinearity and dispersion [132]. The cardiac tissue and brain consist of billions of neurons, which forms a complex network. It could be better to further discussed this problem by setting different topological network of neurons [81] for better dynamical analysis and potential disease occurrence. Based on this new model, different noise-like electromagnetic radiation can be used to better investigate the dynamical response in excitation and electrical activities. This could improve our understanding of potential mechanism of nervy diseased induced by electromagnetic radiation.

Modulational instability was used to study pattern formation in an improved cardiac model, whose cells are exposed to external electromagnetic radiation of periodic type. This improved model included the magnetic flux variable used to describe the effect of electromagnetic induction in cells, created during the fluctuation of electrical activities and ions concentration from Faraday electromagnetic induction theory. Indeed, appropriate electromagnetic field can be induced in cardiac tissue, when exposed or surrounded by external electromagnetic radiation. We use the powerful discrete multiple scale expansion method to reduce the generic equations to a single differential-difference amplitude nonlinear equation, on which linear stability analysis is performed. Using data obtained from our linear stability analysis, we performed the numerical experiments. As earlier predicted from our stability analysis, the system supports multiple localized modes, with different topologies, consistent with biological experiments. This include breather-like excitations,

soliton-like in shapes, where under certain conditions, have been reported to move and transport energy along biophysical systems. This result suggests from biological point of view that the electrical wave of excitations initiated from sinus node can propagate in cardiac tissue in the form of localized modulated solitonic waves thereby regulating heart beat. Other patterns include spatially broadened pulses or front waves reported in triggering harmonized contractions in the heart, whose failure can lead to important physiological disturbances. We remark as well that, pattern dynamics generally presents a diminishing pattern under a high frequency electromagnetic radiation with high intensity. Such pattern disappearance under a high frequency electromagnetic radiation with high intensity could greatly reduce oscillating behavior in electrical activities and heartbeat terminated. This can possibly cause the heart not being able to pump enough blood to supply the body needs, leading to a collapse of the body normal functioning. The result of this subsection 3.2 recommends prevention against electromagnetic radiation, vital for the healthy functioning of the heart.

Due to the complex topology of neural constitution in the brain, it would be very interesting to investigate the effect of EMR on neural dynamics coupled by memristive synaptic coupling.

3.3 Effect of EMR on the dynamics of spatiotemporal patterns in memristor-based neuronal network

In this section, we discuss the effects of electromagnetic radiation on the electrical activity of neurons coupled by a memristive synapse. For this purpose, we study analytically and numerically the MI phenomenon, first by representing the different profiles of the critical amplitude given by the relation (2.85), then by numerically integrating the system of Eq. (2.6) which describes the spatiotemporal dynamics of the action potential influenced by memristive synapse and external electromagnetic radiation . We find that small memristive synaptic coupling may be responsible for regular bursting patterns and may enhance synchronous states in the network. However, with increasing the coupling, full synchronization is difficult to realize and leads to irregular spatiotemporal patterns of action potentials. It is confirmed that under strong electromagnetic radiation, the propagating waves encountered turbulent electrical activities, with patterns breakdown into a homogeneous state. This disordered state, collapse and instability of traveling

pulse is monitored and analyzed using the sampled time series for membrane potential. It decreases to quiescent state under strong electromagnetic field.

3.3.1 Analytical features of MI

In a discrete lattice, MI phenomenon can be predicted from the profiles of the critical amplitude which characterizes the threshold amplitude of the plane wave above which the latter become unstable under a slight disturbance due to the interplay between nonlinearity and dispersive effects of the medium. Indeed, the critical amplitude B_{cr} given by Eq. (2.85) depends on several parameters such as the wave numbers q and ϑ of carrier and plane waves, respectively and the memristive synaptic coupling strength K just to cite a few. In what follow we will attempt to picture the variations of the threshold amplitude as a function of q and K as a system control parameters.

Fig. (3.16) depicts the variation of critical amplitude (B_{cr}) with respect to the wave number (q). The stable and unstable regions of MI are clearly displayed. To bring out the effect of the memristive synaptic coupling (K), the critical amplitude has been plotted for different values of K. The critical amplitude is found to be an increasing function of the memristive synaptic coupling, thus showing how important such coupling could be in the process of signal processing in the brain. However, linear stability analysis is based mainly on linearization around the unperturbed plane wave, valid only when the amplitude of the perturbation is small in comparison with the amplitude of the carrier wave. This makes such linear approximation to fail at large time scales as the amplitude of the unstable sideband grows exponentially. In addition, linear stability analysis minimizes the consequence problem of wave-mixing, by not taking into account extra, additional combination of waves formed through this process, which albeit small at the onset stage, will not remain negligible at great time scales hence cannot give us the long time evolution of a modulated nonlinear plane wave. In the next paragraphs, the generic model will be integrated numerically to explore the long-time evolution of the slightly modulated plane wave propagating in the networks.

3.3.2 Numerical analysis of MI

To confirm the analytical results, we have solved numerically the generic Eqs. (2.6) using the RK4 computational scheme with time-step $h = 0.01$. The initial conditions

correspond to slightly modulated plane waves, with wave numbers selected as $q = 0.15\pi$ and $\vartheta = 0.1\pi$, chosen from the instability regions of the MI [Fig. (3.16)]. It is therefore expected that for these selected values of q and ϑ, while fixing K, unstable wave patterns will emergence in the cell lattice. In the rest of the paper, we investigate through pattern formation and time series analysis, the effect of memristive synaptic coupling and electromagnetic radiation on the features of subsequent wave patterns of the membrane potential. Firstly, we fix K=0.05 and the results plotted in Fig. (3.17).

The panel in Fig. (3.17) presents spatially homogeneous patterns, with temporal periodic-like structures. This obtained pattern confirmed our analytical prediction as the system clearly displays separated rows of localized wave pattern. As earlier predicted, this is the consequence of the simultaneous effect of dispersion and nonlinearity in the system. The formation of separated structures with rows appeared as a consequence of the highly pronounced discreteness effect, which involves the sequencing of the cells lattice involved in collective oscillations. We further investigate the effect of memristive synaptic coupling gain on pattern formation by increasing its value, which will indubitably affects the behavior of the system. The results are presented in Fig. (3.18).

As expected, higher value of memristive synaptic coupling has greatly influenced the calculated spatiotemporal patterns. As the value of the memristive synaptic coupling is increased from left to the right of Figs. (3.18) , we observed a modification in the spatial pattern, through the formation of more curved localized wave patterns [Figs. (3.18c)]. The formation of these curved patterns clearly destroys the formal synchronized patterns obtained for small memristive coupling. The large memristive synaptic coupling K with corresponding unsynchronized patterns in Figs. (3.18c) could implies strong information transmission through the lattice and can account for the variation of sleep rhythms at different stages in thalamocortical networks [133]. Dynamical properties accompanied by the destruction of coherency by strong interactions have been confirmed to be a general phenomenon in neural networks [134]. As a potential mechanism, diversity in synaptic connection between neurons may initiate traveling wavefronts in the network to act as regulator of collective electrical behaviors. However, strong interactions may give rise to small radiation, with features of incoherent wave collisions. As such, in a large neural population, when firing is done simultaneously, a number of multiple collisions could be undergone by the subsequent waves, which could unquestionably destroy coherency as observed in Figs. (3.18c) . The time series for membrane potential at are calculated at

different nodes and results plotted in Figs. (3.19).

Figs. (3.19) presents nonlinear quasi-periodic oscillations with some features of synchronization. This is highly significant from biological point view and has been reported to account for large dynamical range of sensory cortex [135]. Synchronous oscillations from groups of neurons have been shown to correlate with quickly changing mental states, such as absorbing and analyzing new information [123]. It is known that external stimuli can be effective to change the excitability and electrical activities of neurons. By setting appropriate forcing for I_{ext}, the results are presented in Figs. (3.20).

It is found in Figs. (3.20) that electrical activities are modulated by appropriate trans-membrane current under memristive synaptic interactions. Distinct oscillatory properties are observed in the sampled time series for trans-membrane potential and confirmed that electrical activities are controlled by external stimuli. Networks with complex topology can display complex spatiotemporal patterns essential for a higher coordination of brain functions as well as it ability to adapt to a variety of different environmental conditions. Though the emergence of spatial disordered state under strong coupling interactions are recognized general phenomena of neural networks, they should be controlled to avoid some pathological brain rhythms such as Parkinson's and epileptic seizures, which have been reported to have the same anatomical-physiological structures [121]. In the past years many contributions have been made towards eliminating some nerve diseases by stimulating some closely packed cells in the internal regions of the brain [136]. We further investigate the effect of an external forcing on the resulting disordered patterns created by the strong memristive synaptic coupling. The results are plotted in Figs. (3.21).

The results of Figs. (3.21) suggests the possibility of achieving spatial regularity or coherency in the network by increasing the value of the external forcing. The rise in the use of electromagnetic portable instruments, multiplications of electrical devices in flats, nearness of manufacturing industries to the domain of habitations have increased electromagnetic interactions in human biological cells, notably the cells of the brain and the heart. We approached this effect of electromagnetic radiation by considering a periodical type of radiation($\phi_{ext} = A\cos(2\pi ft)$), imposed to change the distribution of magnetic field and also the magnetic flux. We first set the frequency f=0.2, and amplitude A=0.04, with the observed patterns and corresponding time series presented in Figs. (3.22).

The results in Figs. (3.22) confirmed the modulation in electrical activities of cells in the presence of an external electromagnetic radiation. The spatiotemporal pattern

revealed the breakdown of the initial separated localized wave pattern in the cell lattice into a clearly disordered state under electromagnetic radiation. The sampled time series which is helpful in predicting the occurrence of breakdown in a network is also presented in Figs. (3.22) at the cell node 300. It is observed that the cells excitability are highly reduced by this external influence of electromagnetic radiation. At about 350 time units, oscillatory behavior are observed to have completely reduced to the quiescent state. To better comprehend this effect, we keep the frequency of the electromagnetic radiation fixed and the effect of the electromagnetic radiation intensity on pattern formation is examined. The results are plotted in Figs. (3.23) as the amplitude of the electromagnetic radiation is increased.

It is observed in Figs. (3.23) clear modification in the obtained pattern of waves as the intensity of electromagnetic radiation is increased. This is witnessed through the formation of more scattered patterns as the intensity of electromagnetic radiation is increased. With the amplitude fixed, the effect of the electromagnetic radiation frequency is investigated, with results illustrated in Figs. (3.24).

Figs. (3.24) depicts the effect of high frequency electromagnetic radiation on the network. We observe a gradual breakdown in network synchronized spatial patterns into scattered and chaoting patterns as the frequency of the electromagnetic radiation is increased. The results in Figs. (3.24) related to high frequency electromagnetic radiation could result from uncontrolled firing of nerves. This uncontrolled firing leads to uncontrolled transfer of information which is sometimes noticed in corticothalamic circuits in the case of epileptic seizure [137]. Indeed, large intensity of electromagnetic radiation can cause complex responses in myocardial and neural networks [138]. The sampled time series for trans-membrane potential is plotted in Figs. (3.25).

It is found in Figs. (3.25) that the sampled time series for membrane potentials decrease to quiescent state with the increase of calculating time when external electromagnetic radiation is imposed on the media. In another regards, at a low frequency electromagnetic radiation, the media may absorb the electromagnetic radiation, and the cell can select appropriate modes in electrical activities. At a high frequency electromagnetic radiation, the oscillating behavior of electrical activities are seriously suppressed. In the case of high-frequency electromagnetic radiation, the media becomes polarized by the external electromagnetic field thus the electrical activities can be greatly affected.

Strong coupling in a network may enhance pattern formation while a collapsed or

breakdown in the lattice is usually observed when it suffers an external attack. It could also be much better to discuss this problem on networks with different topological connection so to reflect the real nature of brain neuronal connection. This may be achieved by including the action of chemical synapse, field coupling, synapse plasticity. Improved models with autapse can also be used to investigate the effect of noise-like electromagnetic radiation such as white Gaussian noise, necessary for potential mechanism of disease occurrence to be understood.

In short, based on the modified diffusive FitzHugh-Nagumo neural network model with memristive coupling, the conditions and mechanisms leading to the formation and propagation of modulated wave in neural tissues via the activation of modulational instability are exclusively addressed. By reducing the whole system networks to a single differential-difference nonlinear equation with features of cubic Schrödinger equation , we perform linear stability with emphasizes on the magnetic flux. The memristive synaptic coupling K is found to importantly modify instability features. Our analytical predictions are confirmed via numerical experiments on the generic model, where the system is revealed to support localized excitation mode. This mode identified as nonlinear quasi-periodic wave patterns with feature of synchronization are highly relevant from biophysical point of view. It has been observed in the thalamic relay neurons to mediate interneuronal communication [139]. Among others, we further observed a modification in excitation patterns, through the formation of more curved localized wave patterns as K is increased. A potential mechanism is suggested to be related to strong interactions which give rise to small radiations, with features of incoherent wave collisions. That is, its possible to say that in a large number of neurons, when firing is done simultaneously, a number of multiple collisions could be undergone by the subsequent waves, which could unquestionably destroy coherency.

With electromagnetic radiation imposed as a periodic forcing on the improved model, large intensity electromagnetic radiation has clearly been found to induce the breakdown of spatial patterns of the neural network wave patterns. It's thought that when the external radiation is weak, the media may absorb the electromagnetic radiation, and the cell can select appropriate modes in electrical activities. Otherwise, in the case of high-frequency electromagnetic radiation, the media becomes seriously polarized by the external electromagnetic field thereby suppressing the electrical activities neurons. It indicates that brain functioning can be impaired, when it is exposed to external electromagnetic field

with strong radiation intensity. This could provide helpful potential mechanism in understanding and better investigating various brain seizures. It tells us that prevention against electromagnetic radiation is essential and helpful for our normal brain functions.

3.4 Modulated wave solution of diffusive myocardial network under magnetic flow effects

Analytical study has revealed the existence of localized modulated wave in the diffusive FitzHugh-Nagumo myocardial network, through the analytical solution for membrane action potential $x_{n,m}(t)$ which has been proposed with direct dependence on the electromagnetic induction gain and certain parameters which are know to be strongly influenced by such frequency regimes. Also analytical expressions of angular frequency and group velocity have also been derived and their dependence on electromagnetic induction gain clearly illustrated. Our analytically predicted solution is then verified numerically.

As earlier stated from Benjamin-Feir instability criteria, the stability of the network plane waves depends on the sign of $P_r \times Q_r$. Modulated unstable wave arise in the region $P_r \times Q_r > 0$. This is possible only when the propagating plane wave has wave number less than the threshold or critical wave number q_{cr} as illustrated in Figs. (2.9). In accordance to this criterium, we shall in all our numerical plot use wave number always far less than the threshold wave number.

Figs. (3.26) shows the form of the cardiac ionic impulse propagating in the network in all the computational domains for $q = 0.02\pi$. It clearly shows how the solution Eq. (2.80) has the form of an asymmetric envelope soliton. Fig. (3.26a) depicts the three-dimensional spatiotemporal evolution of the traveling cardiac ionic impulse with an oscillatory profile inside an envelope. Fig. (3.26b) shows upper view of the pulse while Fig. (3.26c) depicts its spatial profile at $t = 3010$. The spatial profile is clearly a single asymmetric pulse expected to carry information from one site to another for a better coordination of some important cardiac processes on one side, and in pathological situations on the other [131].

The effect of perturbation on the form of the soliton development is illustrated in Fig. (3.27). The variation of the parameter ϵ does not affect the form of the ionic wave but its amplitude. The perturbation increases the amplitude of the cardiac ionic wave.

The impact of the induction current created by time-varying electromagnetic field as a result of internal bioelectricity fluctuation of cardiac tissue is illustrated in (3.27).

Increasing the memristor coupling decreases the ionic wave amplitude. This indicates that a higher positive feedback gain in induction current can provoke higher excitability capable of blocking wave propagation in the network. This confirms some of the predictions by Takembo et al in Ref. [138], where electromagnetic induction and radiation is imposed on myocardial cells and the mechanism of heart failure explained.

The above outcomes show that signal processing and transmission in cardiac tissue are achievable by means of localized excitations. These nonlinear excitations are generally known to be localized solutions of widespread category of weakly nonlinear dispersive partial differential equations. They were originally observed in surface water wave by John Scott Russel [126] and is well known to originate from the balance between nonlinearity, dispersion and dissipation. Motivated by the presence of these features as earlier identified from Eq. (2.12), we predicted the existence of this solitary wave as confirmed by the present outcome.

Solitary waves are ideal communication tools in diverse domain of physics due to their regenerative character, which gives it's robustness and stability. Nevertheless a challenge still remain, being that of concomitantly conveying not only safely but also quantitatively, a huge diversity of information. This challenge of simultaneously transmitting huge set of harmonics along biochemical milieu can be addressed by relying on stimulus in the form of wave packet. In the next paragraph, we search for an envelope soliton solution of our nonlinear equation of motion.

A form of the soliton solution of the ionic wave amplitude Eq. (2.66) obtained using the Nozaki and Bekki ansatz [82, 109] is given by Figs. (3.29) below

Figs. (3.29) portrays the shape and behavior of cardiac ionic wave in all the computational domains, from Figs. (3.29). It is clear this analytical solution emerges in the form of a single asymmetric pulse, propagating along the medium. These figures show the 3D spatiotemporal evolution [Figs. (3.29a)] of the traveling ionic impulse where, its upper view is presented in Figs. (3.29b), and its spatial profiles at $t = 10$ in Fig. (3.29c).

The solution plotted in Figs. (3.29) depict once again envelope solitons that have all the features of the impulses, ubiquitous in excitable media like neurons and cell membranes. They have in fact an oscillatory profile inside an envelope and carry information from one site to another for a better coordination of some important cardiac processes on one side, and in pathological situations on the other. In [140], for example, it was showed that due to the presence of dissipation, these waves could be unstable, and influenced by time as

clearly depicted in Figs. (3.30).

We note the influence of the parameter ϵ in helping us differentiate the orders of development of the solitonic pulse. This is presented in Fig. (3.31). We notice that as the perturbation increases, the oscillation remains breather modulated solitonic excitation and the amplitude of the ionic wave enhanced. A similar phenomenon has already been observed diffusively coupled Hindmarsh-Rose neural networks [90].

3.4.1 Numerical experiments

We recall that the results already obtained and discussed in the previous section were realized after some approximations. The main objective of this section is to ascertain the ability of the original FHN neuronal network model to support the type of analytical solutions obtained above. For this reason, we solve the generic set of Eqs. (2.8) via the standard fourth-order Runge-Kutta computational scheme with time-step of 0.01 and periodic boundary condition. To achieve this initial value integration, we select the analytical solution given by Eq. (2.80) as the initial conditions. Figs. (3.29) depicts the time behavior of the numerical solution of the generic set of Eqs. (2.8). As earlier predicted analytically, the time behavior of the obtained solution depicts a propagating breather soliton. This result testifies that our discrete model supports breathing solution and hence our analytical solution agrees with numerical experiments.

Usually, trains of modulated waves obtained in this context are generally the result of the activation of modulational instability, and some results on this issue are reported for example in Refs. [127, 141]. In Refs. [127], such solitonic waves in microtubule model are understood as triggering signals for motor proteins to commence motion. As well, modulated solitonic waves have been suggested to be precursor of bubbles that appear in DNA thermal denaturation, responsible for the breaking of hydrogen bond linking the bases [141].

The often non-observance clinical effect attributed to some pathological heart diseases, motivated this paper in the light of obtaining the type of localized structures that propagate in the polynomial form of the realistic cardiac tissue networks using fairly standard perturbation approach. Comprehending the mechanisms underlying such waves in cardiac tissues is of deep importance, relevant in understanding both physiological and pathological phenomena. Bursting features in excitable media is a recurrent alternation between quiescent phases (small amplitude oscillations) and active phases (large amplitude oscil-

lations). Investigating the characteristics of regularly and irregularly oscillating localized structures could be fruitful for fundamental insights into spatiotemporal dynamics and chaos in the cardiac population. This could stimulate possible further investigation in the domain of cardiac cells population information encoding and transmission where several cells fire within a population.

In summary, the main objective of this subsection 3.4 was to study nonlinear localized excitations in an improved FitzHugh-Nagumo (FHN) cardiac networks where adjacent cells are connected through gap junction with nearest neighbor interactions. We begin our investigation by transforming the three variable model equations into wave form, with the equation governing the motion of the membrane voltage in a Lienard form. We proceed to find low amplitude modulated wave solution of the FHN cardiac tissue networks. To achieve this, the multiple scale analysis in the semi-discrete limit is employed. We obtain at the first and second order, the dispersion and group velocity relations of the stimulus dependent on the memristor coupling and other system parameters. At the third order of approximation, we obtain a modified Complex Ginzburg-Landau equation (CGLE) from the transmembrane potential equation of motion, which is an equation governing the evolution of modulated waves in the coupled cardiac networks. From biophysical point of view, electrical signals and waves emitted from the sinus node propagates within the cardiac tissue using both space and time domains in order to regulate heart beat as powerful pacemaker. In another regards, the oscillation of myocardial cells at the sinus node generate a spatiotemporal dynamics of waves between cells as modified by the effect of electromagnetic induction set up during ions fluctuation inside and outside of the cell.

By direct resolution of the obtained CGLE, the analytical solution portrays an asymmetric envelope soliton with features of impulses. This modulated soliton properties are showed to be greatly influenced by memristor coupling as well as the impact of small perturbation. Furthermore, using the Nozaki and Bekki ansatz, the soliton solution of the ionic amplitude equation is obtained. Once again, the obtained analytical solution is an envelop soliton, appearing in the form of a breather-like coherent excitation. In another regards, such structures have been showed to be mechanically relevant in other biophysical settings [127, 141]. For example, in microtubule model they are understood as triggering signals for motor proteins dynamics [127]. They have also been suggested to be precursor of bubbles that appear in DNA thermal denaturation, responsible for the breaking of hydrogen bond linking the bases [141]. The relationship with the present paper may indicate

the essential role of breathers and other nonlinear excitations in regulation of heartbeat.

Conclusion

The effect of the physical phenomenon of magnetic flow; electromagnetic induction and radiation, on co-operative behaviors; wave propagation, synchronization and pattern formation, have been studied in this chapter in order to better understand the complex functioning of biological excitable cells. The phenomenon of MI due to the combined effects between nonlinearity and the dispersion of the explored systems, allowed to realize that the transport and the transfer of nerve and cardiac impulses can be ensured by a soliton-like solitary wave, thus consolidating the theory on the solitonic essence of nerve impulses. Indeed, we have shown that the phenomenon of MI is affected by electromagnetic induction and radiation. Electromagnetic induction feedback gain in both neuronal network and cardiac tissue promotes MI via the formation of multiple localized wave patterns. However, in the presence of an external magnetic field induced by the memristive current, MI phenomenon is reduced for high electromagnetic induction thus giving rise to the synchronization phenomenon. It was showed that MI phenomenon and synchronization are complementary phenomena since MI can be used analytically to predict the emergence of nonlinear synchronous patterns in neural networks. High intensity electromagnetic radiation initiates turbulent behaviors in electrical activities of excitable cells via pattern breakdown. It is hopeful that this work will improve our knowledge of the role of electromagnetic induction and radiation in mediating intercellular communication in both neuronal and cardiac networks.

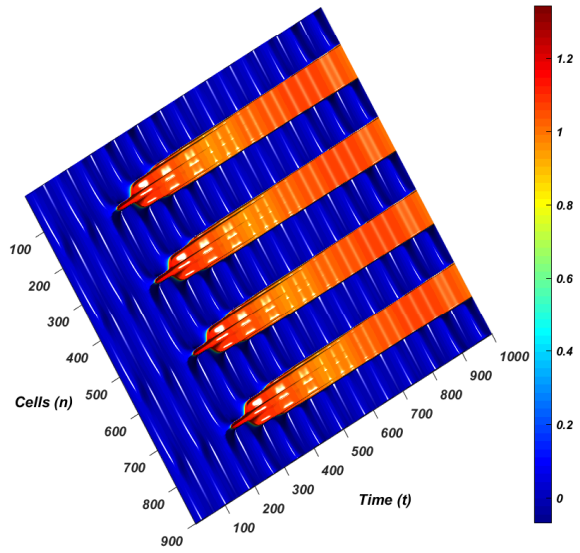

(a)

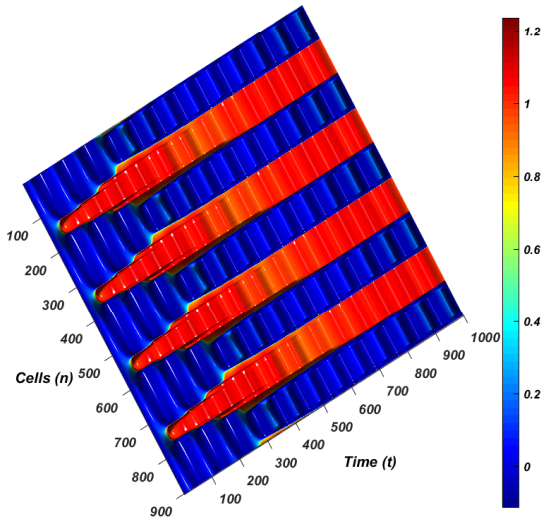

(b)

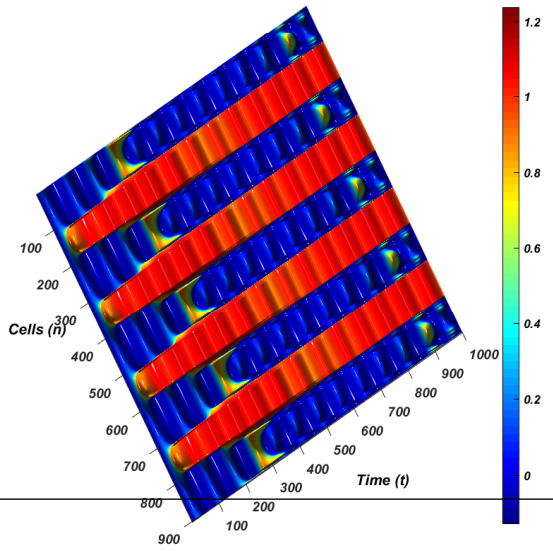

(c)

Figure 3.15: Panels show the spatiotemporal features of patterns for the stimulation

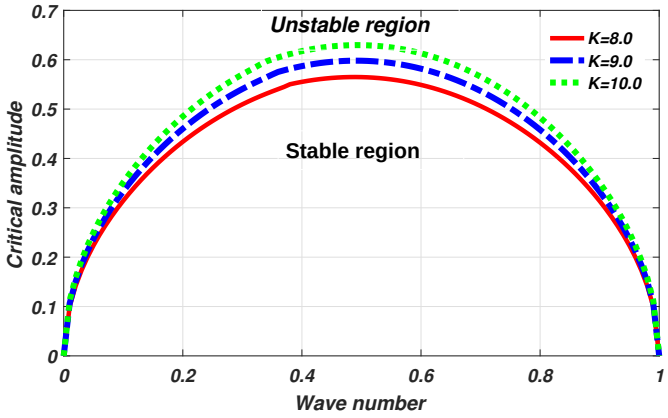

Figure 3.16: Plot of critical amplitude, vs. the wave number for different values of memristive synaptic coupling (K). The growth rate of modulational instability is an increasing function of the memristive synaptic gain(K).

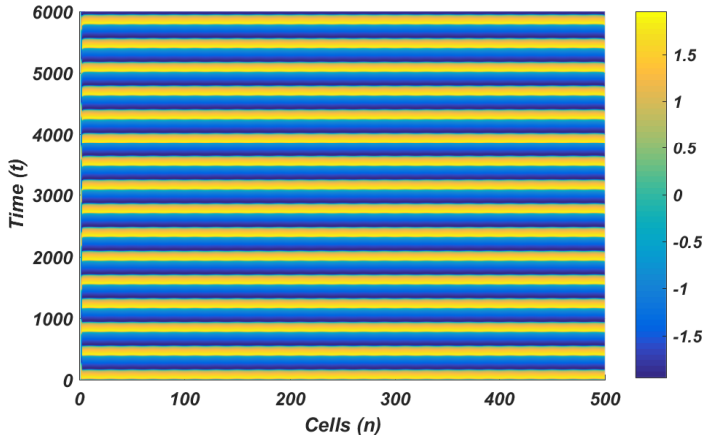

Figure 3.17: Panel presents spatially homogeneous patterns, with temporal periodic-like structures calculated for the memristive synaptic gain $K = 0.05$, with $I_{ext} = 0.6$

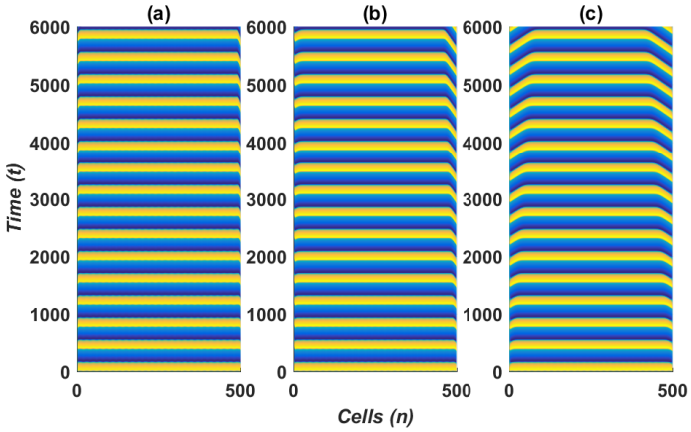

Figure 3.18: Panels show the spatiotemporal features for different values of the memristive synaptic gain; (a) K=1.0, (b) K=5.0, and K= 10.0, with $I_{ext} = 0.6$

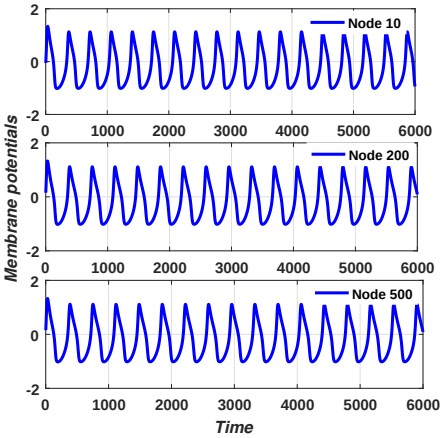

Figure 3.19: Time series for membrane potential at the nodes 10, 200, and 500 with K=0.05 and $I_{ext} = 0.6$

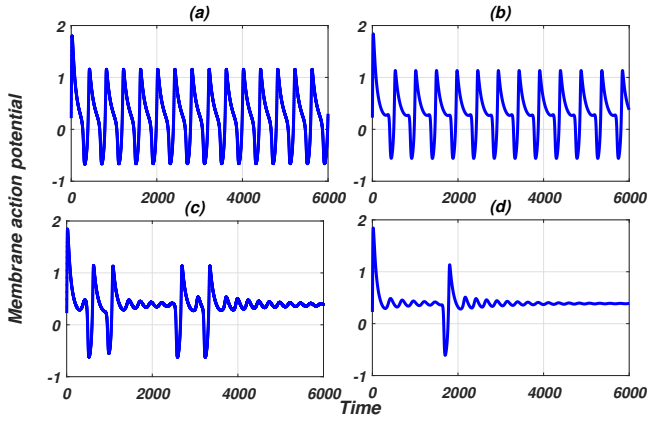

Figure 3.20: Time series of the node 300 for different external stimuli; (a) $I_{ext} = 1.300$ (b) $I_{ext} = 1.410$ (c) $I_{ext} = 1.418$ and (d) $I_{ext} = 1.421$

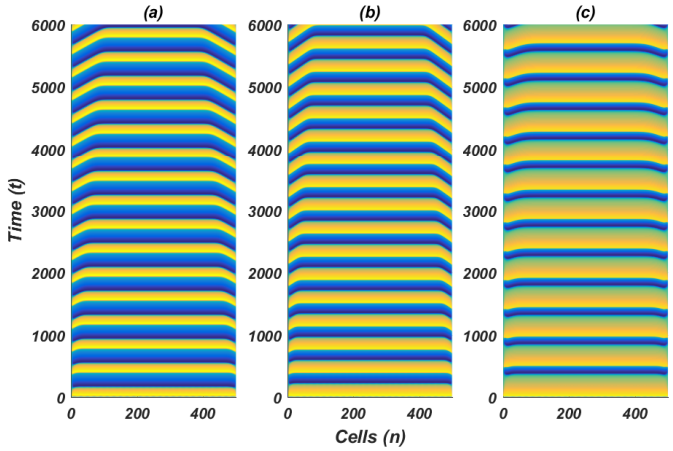

Figure 3.21: Spatiotemporal evolution of the membrane action potential and the effect of an external stimulus on wave patterns. It has been plotted for (a) $I_{ext} = 0.60$, (b) $I_{ext} = 1.0$ and (c) $I_{ext} = 1.4$ for K=10.0

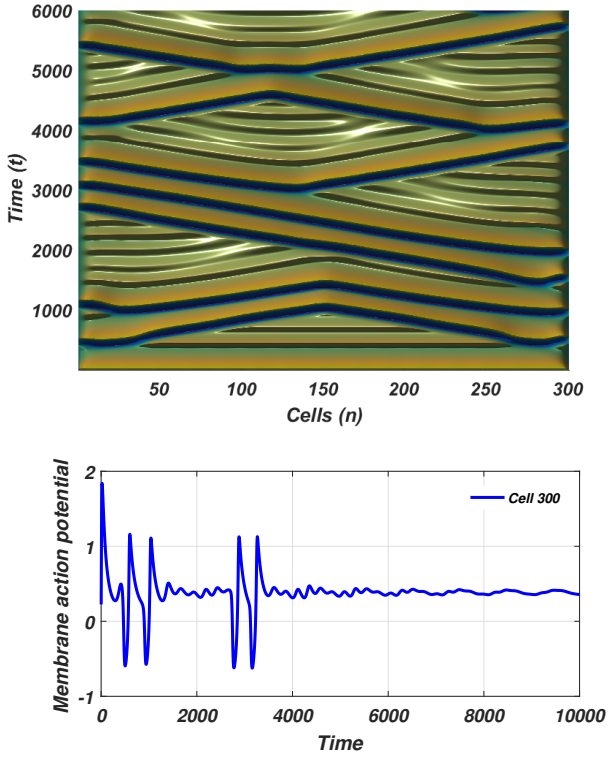

Figure 3.22: Developed spatiotemporal pattern and time series calculated for the constant frequency external electromagnetic radiation intensity $A = 0.04$, with $f = 0.2$ and $I_{ext} = 1.418$

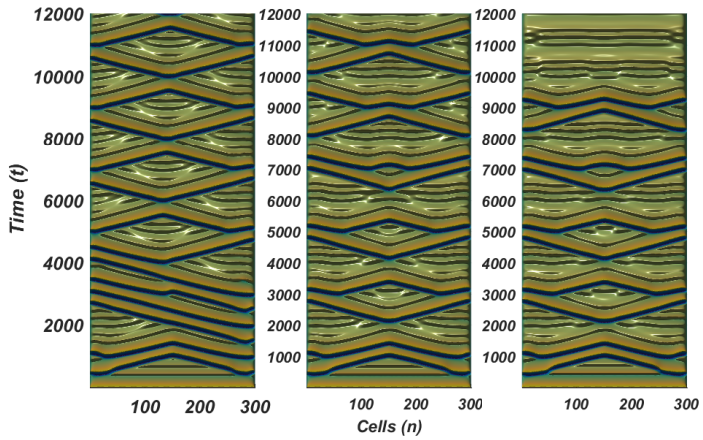

Figure 3.23: Spatiotemporal evolution of the membrane action potential and the effect of an external electromagnetic radiation intensity on wave patterns. It has been plotted for $A = 0.055$, $A = 0.065$ and $A = 0.075$, from Left to Right.

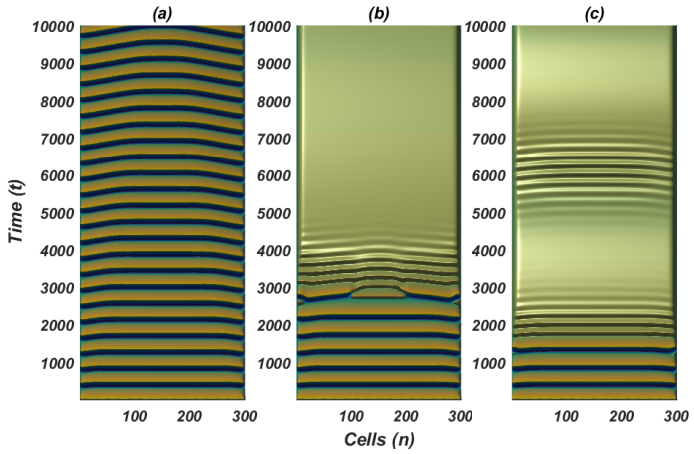

Figure 3.24: Spatiotemporal evolution for different frequencies of external electromagnetic radiation, (a) f=0.002, (b) f=0.02, and (c) f=0.04, with A=0.05

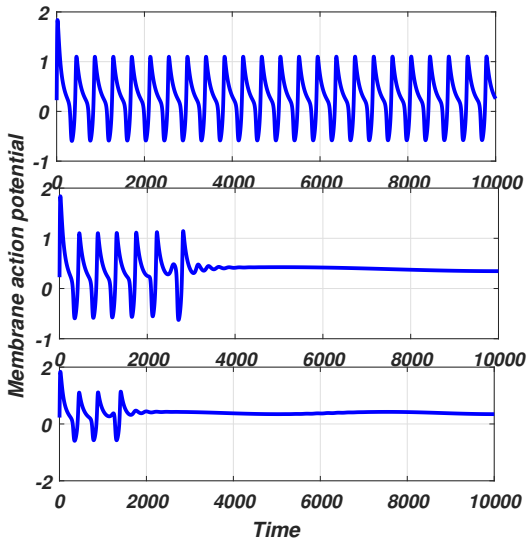

Figure 3.25: Corresponding time series evolution for different frequencies of external electromagnetic radiation for parameter values illustrated by Figs. (3.24). The intensity increases from Top to Bottom.

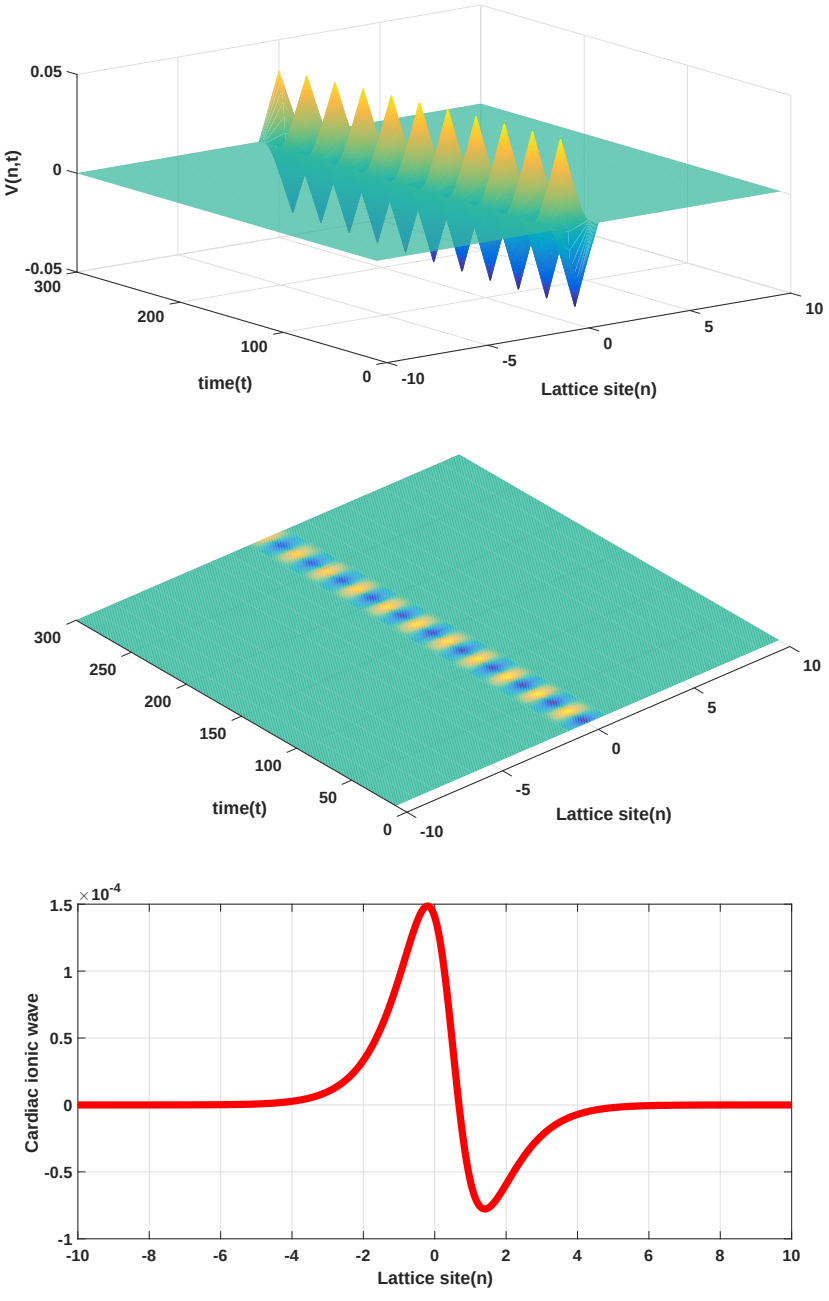

Figure 3.26: Spatiotemporal evolution of the cardiac ionic wave in all the computational domains: (a) 3D view of the traveling cardiac pulse, (b) upper view, and (c) spatial ionic wave profiles at t=10. Signal appears in the form of a nearly symmetric wave packet. $k_0 = 1.0, q = 0.02\pi, \epsilon = 0.01, A_0 = 0.01$ and t=3010

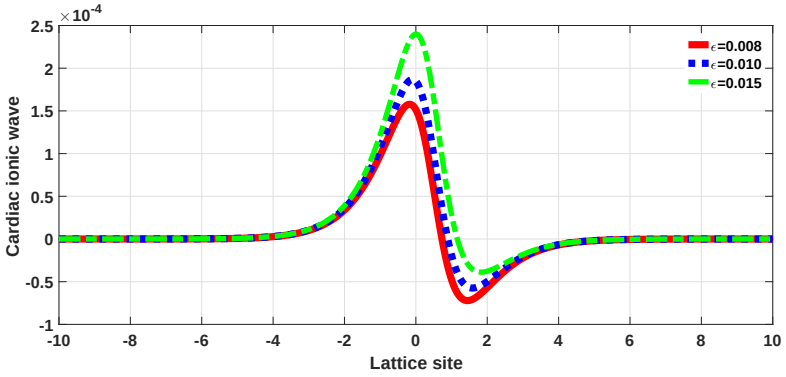

Figure 3.27: Impacts of small perturbations on the cardiac ionic wave. $k_0 = 1.0, q = 0.02\pi, A_0 = 0.001$ and t=3010

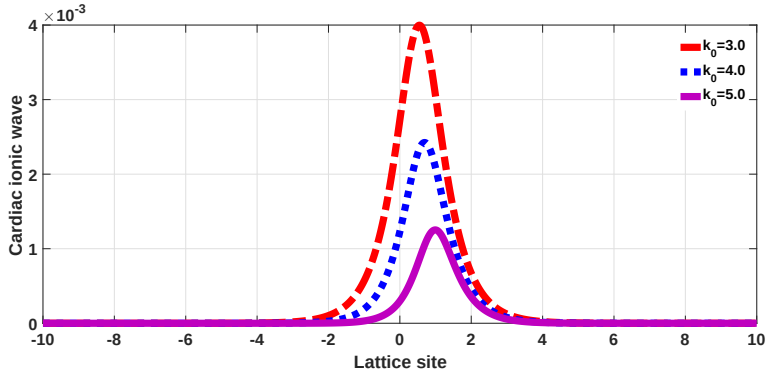

Figure 3.28: Impact of electromagnetic induction on the cardiac ionic wave. $q = 0.02\pi, A_0 = 0.001$ and t=3010

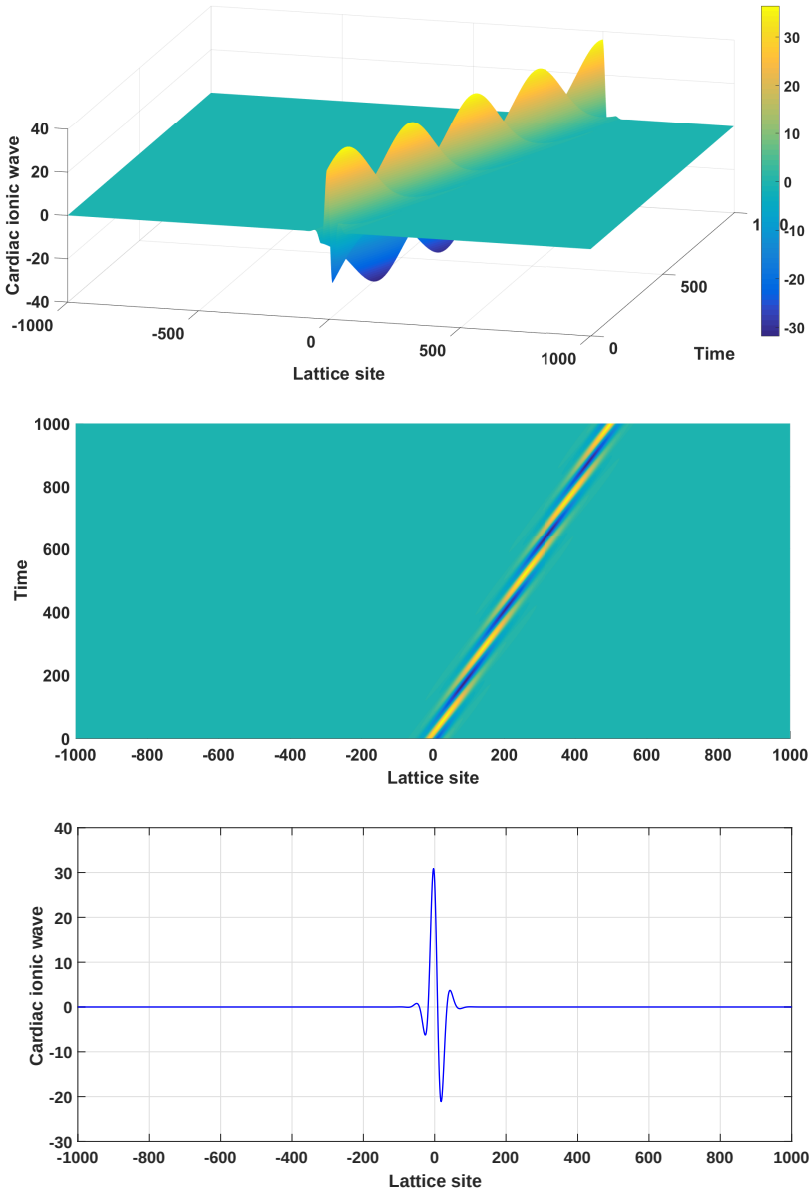

Figure 3.29: Spatiotemporal evolution of the cardiac ionic wave in all the computational domains: (a) 3D view of the traveling cardiac pulse, (b) upper view, and (c) spatial ionic wave profiles at $t = 10$. Signal appears in the form of an asymmetric wave packet. The parametric values are; $D_0 = 0.05, k_0 = 1.0, q = 0.02\pi, \epsilon = 0.70$ and $A_0 = 1.00$

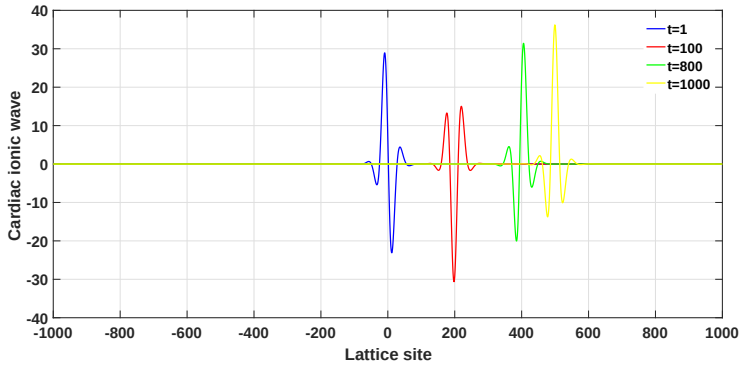

Figure 3.30: Ionic wave profiles at different times

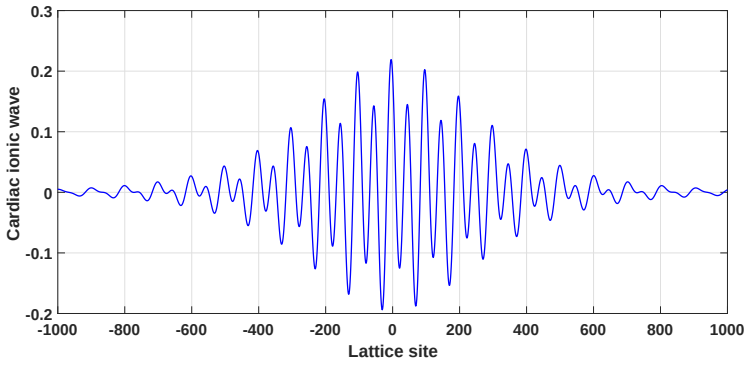

(a)

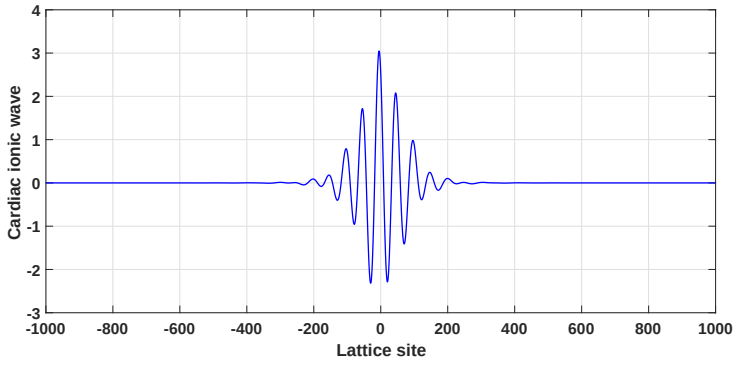

(b)

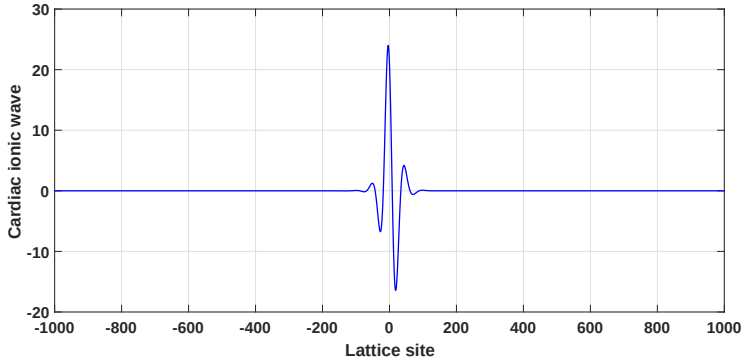

(c)

Figure 3.31: Impacts of small perturbations on the cardiac ionic wave (a) $\epsilon = 0.05$, (b) $\epsilon = 0.1$ and (c) $\epsilon = 0.6$

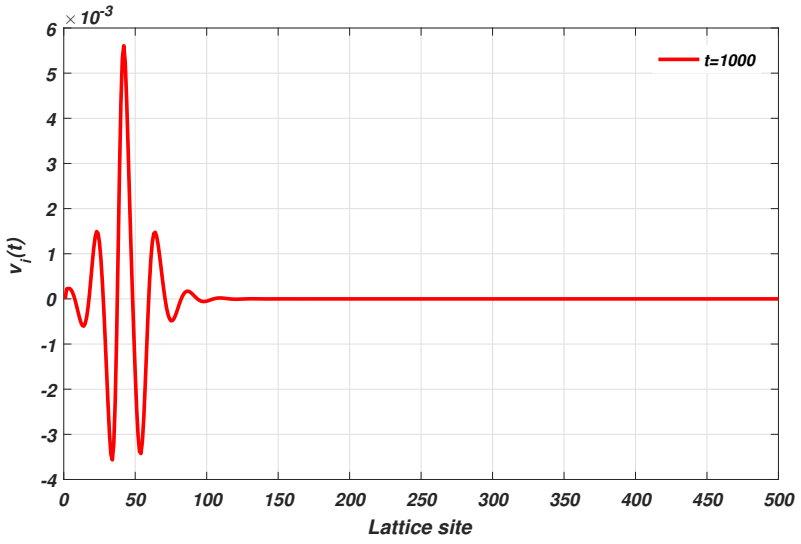

(a)

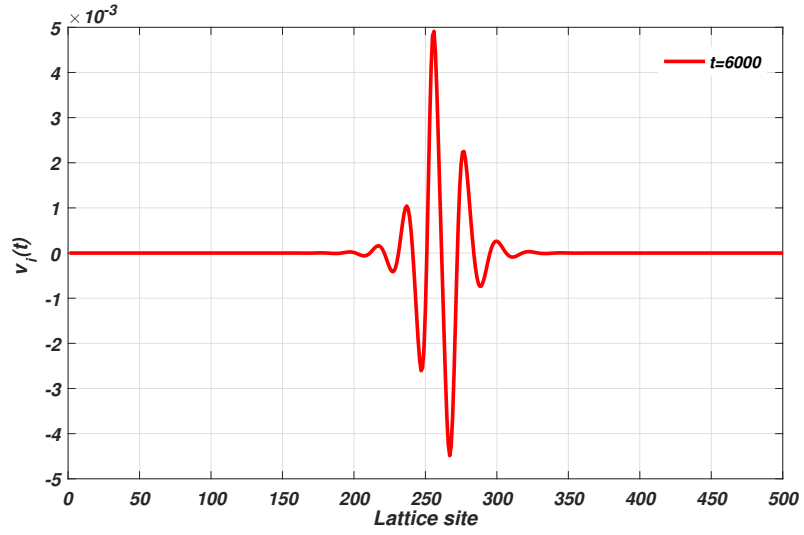

(b)

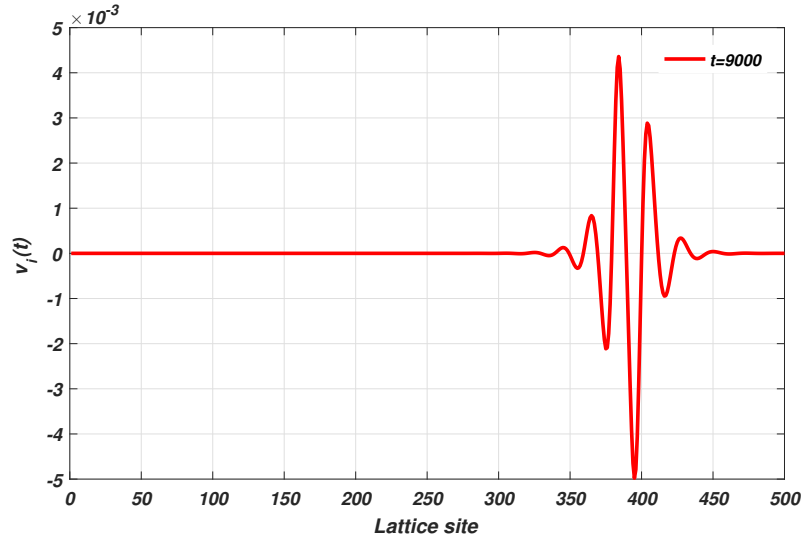

(c)

Figure 3.32: Time behavior of the cardiac ionic wave. The rest parameter values are: $D_0 = 0.05, k_0 = 1.0, q = 0.1\pi, \epsilon = 0.30$ and $A_0 = 0.02$

General Conclusion

Summary

In this thesis, we have investigated wave propagation, pattern formation and synchronization phenomena in biological excitable cells. In order to better describe the complex dynamical behaviors of these cells in a more realistic way, we have taken into account the effect of intracellular and extracellular magnetic flow effects. Using the continuous version of the FHN excitable model, we have developed the improved discrete models under magnetic flow effects, which provides an overview of the collective dynamic of neural and myocardial networks. Our investigations were conducted both analytically and numerically, not only for a better understanding of the studied phenomena, but also to highlight the main properties of the explored model.

To achieve our main goals, the work of this thesis has been subdivided into three chapters. The first one has dealt with an overview on myocardial cells, neurons and NNs. Here some generalities have been presented with emphasis on the functioning of synapses as the bridges that connected two neurons in NNs. We found that both electrical and chemical synapses are structurally and functionally different and the main difference is related to the synaptic delay which is larger in chemical synapses than in electrical ones. That is why electrical synapses are appropriately used in the achievement of NS phenomenon. We have also reviewed some phenomenological mathematical neural models. The biological HH model and many of developed versions have confirmed their effectiveness for recognizing and understanding the electrical activities in neurons. The HH was refined to obtain the FHN model. The FHN model itself is a generalization of the Van der Pol (VDP) oscillator, whose modified version has been recently proposed with the assumption that the neural environment implies some periodic excitations. The importance given to the VDP model equation in recent years come from the fact that it describes self-excited or self-sustained oscillations, suitable to describe some important processes like those related to brain and cardiac waves. That why the FHN was adopted in this thesis in order to better analyze waves propagation, pattern formation and NS phenomena.

In chapter 2, we have presented the improved FHN mathematical models which have been developed along with both analytical and numerical methods. The first model is the diffusive FHN neural network under magnetic flow effects allowing to investigate effects of memristive coupling strength, stimulus current and external electromagnetic radiation either on, modulated wave patterns or, eventual synchronous structures of membrane action potential. The second model depicts the electrical activity of myocardial cells under magnetic flow effect. The role of the memristive coupling and external electromagnetic radiation on instability and pattern formation examined. The third model depicts the complex wiring of neurons in the brain through the memristive synaptic coupling. The fourth one is the one-dimensional FHN NNs where effects of memristive coupling strengths on membrane potential have been explored considering each of frequency regimes which were detected analytically and confirmed numerically. The above models have been handled by means of some analytical and numerical methods. In this context, the DNLS equation describing the spatiotemporal dynamics of envelop soliton has been derived in the discrete approximation. The RK4 method with periodic boundary conditions has been used in the numerical simulations for integrating of original models. As initial conditions usually are known to be influenced by DNLS or CGL equation coefficients, the comparison between both analytical and numerical analysis has been done and suggests a perfect correlation between the found results.

Chapter 3 presents the main results. Through MI phenomenon, the transport and the transfer of the nerve impulses can be ensured by a soliton-like solitary wave. This phenomenon is influenced by strong memristive coupling, external stimuli current, electromagnetic radiation and high synaptic coupling strengths. Collective behaviors of NNs can be characterized by patterns formation and synchronous activity. We found that NS can be enhanced either by small value of stimulus current and MC parameter, or large values of diffuse and memristive coupling strengths. Obviously, our findings set a wide range of biological implications, including the prevention and efficient treatment of many cardiac and brain diseases through the control of NS phenomenon.

Future orientations

The work of this thesis has contributed to the improvement of mathematical FHN models to better understand the dynamics of nerve impulses in NNs. Most of the investigations carried out aimed at studying the phenomena of wave propagation and NS as a function of certain parameters, the number of which is not exhaustive. That is why we are prospecting other research directions that include:

- Thermal effects on modulated synchronous patterns using FHN model with or without

LRI since, temperature appears to play a crucial role in generation and conduction of the nerve impulse.

- Synchronizability between two or more NNs coupled by memristor with intra-and-inter LRI will also be investigated where memristor would behave as electrical synapse.
- The formation and removal of spiral waves in cardiac cells have also attracted much attention in recent decades. Unfortunately, the detection of such waves which result from the inhomogeneities of the target media has been done only either numerically or experimentally. Therefore analytical finding of these survival waves could open new horizons in neuroscience.

Bibliography

[1] O. Bernus, A. V. Holdena and A. V. Panfilov, Physica D. **v-viii** 238 (2009).

[2] Z. Qua, G. Hub et al., *Phys. Rep.* **543**, 61-162 (2014).

[3] D. Zipes and J. Jalife, *Cardiac Electrophysiology: from Cell to Bedside*, Amsterdam: Elsevier, (2013).

[4] S. Grillner and A. N. Graybiel, *"The Interface Between Neurons and Global Brain Function"*, MIT Press, Cambridge, MA, (2006).

[5] R. FitzHugh, Biophys. J. **1** 445 (1961).

[6] J. S. Nagumo, S. Arimoto and S. Yoshizawa, Proc. IRE **50** 2061 (1962).

[7] A. L. Hodgkin and A. F. Huxley, J. Physiol. **117** 500 (1952).

[8] B. Knight, J. Gener. Physiol. **59** 734 (1972).

[9] C. Morris and H. Lecar, Biophys. J. **35** (1981)

[10] J. L. Hindmarsh and R. M. Rose, Nature (London) **296** 162 (1982).

[11] J. L. Hindmarsh and R. M. Rose, Proc. R. Soc. London Ser-B **221** 87 (1984).

[12] J. L. Hindmarsh and R. M. Rose, Proc. R. Soc. Lond. B **237** 267 (1989).

[13] E. M. Izhikevich, IEEE Trans. Neural Networks **14** 1569 (2003).

[14] E. M. Izhikevich, IEEE Trans. Neural Networks **15** 1063 (2004).

[15] M. Lv and J. Ma, Neurocomputing **205** 375 (2016).

[16] M. Lv, C. Wang, G. Ren, J. Ma and X. Song, Nonlinear Dyn. **85** 1479 (2016).

[17] D. R. Chialvo, et al., *Nature(London)* **343**, 653 (1990).

[18] T. Krogh-Madsen and D. J. Christini, *Annu. Rev. Biomed. Eng.* **14**, 179 (2012).

[19] A. Karma, *Annu. Rev. Conden. Matter Phys.* **4**, 313 (2013).

[20] D. Difrancesco, *Annu. Rev. Physiol.* **55**, 455-472 (1993).

[21] G. Seemann et al., *Philos. Trans. A* **364**, 1465-1481 (2006).

[22] K. Fox, *J. Am. Coll. Cardiol.* **50**, 823-830 (2007).

[23] B. Echebarria et al., *Phys. Rev. Lett.* **88**, 208101 (2002).

[24] J. Landaw et al., *Phys. Rev. Lett.* **118**, 138101 (2017).

[25] A. V. Panfilov et al., *Phys. Rev. E.* **61**, 4644-4647 (2000).

[26] R. R. Aliev and A. V. Panfilov, *Chaos Solitons and Fractals* **7**, 293-301 (1996).

[27] M. Lv et al., *Nonlinear Dyn 385.***85**, 1479 (2016).

[28] J. Ma et al., *Chaos Solitons and Fractals* **99**, 219-225 (2017).

[29] A. Mvogo, C. N. Takembo et al., *Phys. Lett. A* **381**, 2264-2271 (2017).

[30] J. Ma et al., *Int. J. Mod. Phys. B* **30**, 1650251 (2016).

[31] Y. S. Kivshar and M. Peyrard, *Phys. Rev. A* **46**, 3198 (1992).

[32] T. B. Benjamin and J. E. Feir, *J. Fluid Mech.* **27**, 417 (1967).

[33] J. Meier et al., *Phys. Rev. Lett.* **92**, 163902 (2004).

[34] E. Sobel and Z. Davanipour, *Neurology* **47**, 1594 (1996).

[35] D. Clarke, and L. Sokoloff, *Basic Neurochemistry: Molecular, Cellular and Medical Aspects, edited by G. J. Siegel et al. (Lippincott-Raven, Philadelphia, 1999).*

[36] C. Johansen, *Epidemiol.* **11**, 539 (2000).

[37] M. Naghavi et al., *Lancet* **385**, 117-71 (2015).

[38] A. Lisi, M.T. Ciotti, M. Ledda, et al., *J. Cell. Phys.* **204(2)**, 532Ű538 (2005).

[39] S.C. Xu, Z. Zhou, L. Zhang, et al., *Brain Res.* **1311**, 189Ű196 (2010).

[40] R. Zhao, S.Z. Zhang, Z.P. Xu, et al., *Toxicology* **235(3)**, 167-175 (2007).

[41] H. Masuda, A. Ushiyama, M. Takahashi, et al., *Radiat. Res.* **172(1)**, 66-73 (2009).

[42] F.Q. Wu, C.N. Wang, Y. Xu, et al., *Sci. Rep.* **6**, 28 (2016).

[43] M. Ge, Y. Jia, Y. Xu, et al., *Nonlinear Dyn.* **91**, 515-23 (2018).

[44] Y. Xu, H. Ying, et al., *Sci. Rep.* **7**, 43452 (2016).

[45] G. Zhang, C. Wang, et al., *Chaos Solitons and Fractals* **108**, 15-24 (2018).

[46] https://opentextbc.ca/anatomyandphysiology/chapter/12-9-cardiac-muscle-and-electrical-actvity (Consulted on November 2018).

[47] Fullick, Ann. Edexcel IGCSE Biology Revision Guide1. p. 40. ISBN 9780435046767 (1984).

[48] http://physiologyplus.com/classification-of-neurons-by-structure-and-function (Consulated on November, 2018).

[49] https://opentextbc.ca/anatomyandphysiology/chapter/12-4-the-action-potential (Consulated on November, 2018).

[50] http://www.psych.ualberta.ca/ ITL/ap/ap.swf (Consulated on November, 2018).

[51] D. Purves, G.J. Augustine, D. Fitzpatrick, W.C. Hall, A.-S. Lamantia, J.O. McNamara and L.E. White, Neuroscience (4th Ed.) **26** (2008).

[52] T. Sasaki, N. Matsuki and Y. Ikegaya, science **331** 599 (2011).

[53] A.L. Hodgkin, J. Physiol. **90** 183 (1937).

[54] A.N. Kolmogorov, I.G. Petrowskij, N.C. Piskunov, Annual Eugenics **7** 255 (1937).

[55] K. Lonngren, A.C. Scott, Proceedings of a Workshop (1977).

[56] J.B. Hursh, Amer. J. Physiol. **127** 131 (1939).

[57] http://wiringcircuit.org.uk/diagram-of-motor-and-sensory-neurons.html, (Consulated on November, 2018).

[58] T.C. Süudhof, Handb. Exp. Pharmacol. **184** 1 (2008).

[59] D.A. Rusakov, Neuroscientist **12** 317 (2006).

[60] Y. Humeau, F. Doussau, N.J. Grant and B. Poulain, Biochimie **82** 427 (2000).

[61] http://www.zoology.ubc.ca/ gardner/synapses (Consulated on November, 2018)

[62] E. A. Pereda, Nat. Rev. Neurosc. **15** 251 (2014)

[63] G. Zoidl and R. Dermietzel , Cell Tissue Res. **310** 137 (2002).

[64] P.R. Brink, K. Cronin and S.V. Ramanan, J. Bioenerg. Biomembr. **28** 351 (1996).

[65] E. Godaux, *Cent Milliards de Neurones*, Collection la science apprivoisée (2006).

[66] L. D. Silva, F. H. Hocks, A. Smits and L. H. Zitterberg, Kybernettik **15** 27-37 (1974).

[67] M. E. Brandt, Int. J. Psychophys. **26** 285-298 (1997).

[68] H. Wang et al., *Commun. Nonlinear Sci. Numer. Simulat.* **19**, 3242-54 (2014).

[69] J. Ma et al., *Int. J. Mod. Phys. B* **29**, 1450239 (2015).

[70] M. Amiri et al., *J. Comput. Neurosci.* **34**, 489-504 (2013).

[71] G. Schmid, I. Goychuk et al., *Phys. Biol.* **1**, 61-66 (2004).

[72] A. carpio and L.L. Bonilla, SIAM J. Appl. Math. **63**(2), 619 (2002).

[73] B. Zinner and J. Diff. Eqs. **96**, 1 (1992).

[74] A. Tonnelier, Phys. Rev. E **67**, 036105 (2003).

[75] A. Panfilov and P. Hogeweg, Phys. Lett. A **176**, 295 (1993).

[76] S. Dimitry, A. Dimitrichev and V. Nekorkin, *Proceedings of Nonlinear Dynamics of Electronic Systems* (2012).

[77] A. Malevanets and R. Kapral, Phys. Rev. E **55**, R4841(R). (1997).

[78] Q. Zhenga and J. Shena, Comp. Math. Appl. **70** 1082 (2015).

[79] S. Abbasbandy, *Apll. Math. Modell.* **32**, 2706-2716 (2008).

[80] H. Triki et al., *Apll. Math. Modell.* **37**, 3221-3828 (2013).

[81] H. Daihai, G. Hu et al., *Phys. Rev. E.* **65**, 055204(R) (2002).

[82] D. Nozaki and D. Yamamoto, *Phys. Lett. A.* **1243**, 281-287 (1998).

[83] I. Maïna, C. B. Tabi, A. Mohamadou, H. P. F. Ekobena and T. C. Kofané, Chaos **25** 043118 (2015).

[84] C. B. Tabi, I. Maïna, A. Mohamadou, H. P. F. Ekobena and T. C. Kofané, EPL **106** 18005 (2014).

[85] C. B. Tabi, A. Mohamadou and T. C. Kofané, Eur. Phys. J. E **32** 327 (2010).

[86] J. Leon and M. Manna, J. Phys. A: Math Gen. **32** 2845 (1999).

[87] J. Leon and M. Manna, Phys. Rev. Lett. **83** 2324 (1999).

[88] A. Mohamadou, F. Fopa and T. C. Kofané, Optics Communications **266** 648 (2006).

[89] A. Mvogo, C. N. Takembo and H. P. F. Ekobena and T. C. Kofané, Phys. Lett. A **381** 2264 (2017).

[90] F. M. Moukam Kakmeni, E. M. Inack, and E. M. Yamakou, Phys. Rev. E **89** 052919 (2014)

[91] F. II Ndzana, A. Mohamadou and T. C. Kofané, Chaos **18** 043121 (2008)

[92] F. II Ndzana, A. Mohamadou, T. C. Kofané and L. Q. English, Phys. Rev. E. **78** 016606 (2008)

[93] F. II Ndzana, A. Mohamadou and T. C. Kofané, J. Phys. D: Appl. Phys. **40** 3254 (2007)

[94] E. Kengne, V. Bozic, M. Viana and R. Vaillancourt, Phys. Rev. E. **78** 026603 (2008)

[95] K. Nozaki and N. Bekki, J. Phys. Soc. Jpn. **53** 1581 (1984).

[96] J. Ketchakeu, T. C. Kofané and A. Zibi, Phys. Scr. **44** 505 (1991).

[97] T. C. Kofané, B. Michaux and M. Remoissenet, J. Phys. C: Solid State Phys. **21** 1395 (1988).

[98] A. Mohamadou, B. E. Ayissi and T. C. Kofané. Phys. Rev. E **74** 046604 (2006).

[99] T. B. Benjamin and J. E. Feir, J. Fluid Mech. **27** 417 (1967).

[100] A. D. Koko, C. B. Tabi, H. P. F. Ekobena, A. Mohamadou and T. C. Kofané, Chaos **22** 043110 (2012).

[101] L. O. Chua, IEEE Trans. Circ. Theory **18** 507 (1971).

[102] T. Kanamaru, Y. Okabe, Phys. Rev. E **62**, 2629 (2000).

[103] Y. Xu, Y. Jia, et al., Chaos Soliton Fract. **104**, 435-442 (2017).

[104] F. Xu, J. Zhang, T. Fang, et al., Nonlinear Dyn . **92**, 1395-1402 (2018).

[105] C.N. Takembo, A. Mvogo, H.P. Ekobena, et al., Int. J. Mod. Phys. B **32**, 1850165 (2018).

[106] K. Nozaki and N. Bekki, Phys. Rev. Lett. **51**, 2171(1983).

[107] A. Hasegawa, *Optical solitons in fiber, Springer tract in modern physics. Vol. 116, Berlin, Springer.* (1989).

[108] K. Nozaki, N. Bekki, J. Phys. Soc. Jpn. **53**, 1581-1582 (1984).

[109] N.R. Pereira and L., Stenflo, Phys. Fluids **20**, 1735-1743 (1977).

[110] L.P. DEVRIES and E.J. HASBUN, *A first course in computational physics*, Second edition. Jones and Bartlett Publishers 215 (2011).

[111] S. Raghavachari and J.A. Glazier, Phys. Rev. Lett. **82** 2991 (1999).

[112] J.Y. Wu, X. Huang, C. Zhang, *Neuroscientist* **(14)**, 487 (2008).

[113] S. Grillner and A.N. Graybiel, *The interface between neurons and global brain function* (MIT Press, Cambridge, MA) (2006).

[114] R. Yuste, J.N. Maclean, J. Smith, A. Lansner, *Nat. Rev. Neurosci.* **(6)**, 477 (2005).

[115] http://jonlieffmd.com/blog/breathing-alters-perception (2018).

[116] N. Barkai, B.Z. Shilo, *Curr. Biol.* **(12)**, R493 (2002).

[117] A.S. Pikovsky, M.G. Rosenblum, J. Kurths, *Synchronization: A Universal Concept in Nonlinear Sciences*, Cambridge University Press, (2001).

[118] W. Schultz, *J. Neurophysiol.* **(80)**, (80) (1998).

[119] A.A. Grace, B.S. Bunney, *Neuroscience* **(29)**, (80) (1984).

[120] A.S. Freeman, L.T. Meltzer, B.S. Bunney, *Life Sci.* **(36)**, (1985).

[121] M.J. Morel, *Neurology* **(77)**, (1295) (2011).

[122] G. Buzsaki, Rhythms of the Brain, Oxford University Press, New York, (2006).

[123] T.Lewis, in: *NIMBIOS Workshop on Synchrony,* April 11, (2011).

[124] E. Marder, D. Bucher, *Curr. Biol.* **11(23)**, R986-R996 (2001).

[125] J. Y. Wu, X. Huang and C. Zhang, *Neuroscientist* **14**, 487 (2008).

[126] T. Dauxois, M. Peyrard and A. R. Bishop, *Phys. Rev. E* **47**, R44 (1993).

[127] S. Zdravkovi, A. N. Bugay, G. F. Aru and A. Maluckov *Chaos* **24**, 023139 (2014).

[128] G. S. Yi, J. Wang, K. M. Tsang et al., *Biol. Cybern.* **109**, 287-306 (2015).

[129] H. G. Gu and B. B. Pan, *Nonlinear. Dyn.* **81**, 2107-2126 (2016).

[130] J. C. Neu, et al., *Physica D* **102**, 285 (1997).

[131] D. P. Zipes et al., *Cardiac Electrophysiology: From Cell to Bedside* (Saunders, Philadelphia, 2000).

[132] T. B. Benjamin and J. E. Feir, *J. Fluid Mech.* **27**, 417 (1967).

[133] D. Terman, A. Bose and N. Kopell, Proc. Natl Acad. Sci. USA **93**, 15417-15422 (1996).

[134] D. Battaglia, N. Brunel and D. Hansel, Phys. Rev. Lett. **99**, 238106 (2007).

[135] T.L. Ribeiro and Copelli *Phys. Rev. E* **77**, 051911 (2008).

[136] J.E. Rubin and D. Terman, J. Comput. Neurosci. **16**, 211 (2004).

[137] P.A. Robinson, C.J. Rennie, and D.L. Rowe, Phys. Rev. E **65**, 041924 (2002).

[138] C.N. Takembo, A. Mvogo, H.P., Ekobena, et al., Int. J. Mod. Phys. B **32**, 1850165 (2018).

[139] H.A. Swadlow and A.G. Gusev, Nat. Neurosci. **4**, 402 (2001).

[140] P.G. Ghomsi, T.J. Tameh Berinyoh and F.M. Moukam Kakmeni, Chaos **28**, 023106 (2018).

[141] T. Dauxois, M. Peyrard and A.R. Bishop, Phys. Rev. E. **47**, 684 (1993).

List of publications

✠ A. Mvogo, **C.N. Takembo**, H. P. Ekobena Fouda, T. C. Kofané, *Pattern formation in diffusive excitable systems under magnetic flow effects*, Phys. Lett. A **381** 2264-2271 (2017).

✠ **C.N. Takembo**, A. Mvogo, H. P. Ekobena Fouda, T. C. Kofané, *Modulated wave formation in myocardial cells under electromagnetic radiation*, Int. J. Mod. Phys. B **32** 1850165 (2018).

✠ **C.N. Takembo**, A. Mvogo, H. P. Ekobena Fouda, T. C. Kofané, *Localized modulated wave solution in diffusive FitzHugh-Nagumo cardiac network under magnetic flow effect*, Nonlinear Dyn. **381** 1079-1098 (2019).

✠ **C.N. Takembo**, A. Mvogo, H. P. Ekobena Fouda, T. C. Kofané, *Effect of electromagnetic radiation on the dynamics of spatiotemporal patterns in memristor-based neuronal network*, Nonlinear Dyn. **381** 1067-1078 (2019).